Université de Toulouse

THÈSE

En vue de l'obtention du

DOCTORAT DE L'UNIVERSITÉ DE TOULOUSE

Délivré par :

Université Toulouse 3 Paul Sabatier (UT3 Paul Sabatier)

Présentée et soutenue par :
Yu ZHU

le mercredi 22 mai 2013

Titre :

Modeling of a microwave plasma electron source for neutralization of ion thrusters

---

École doctorale et discipline ou spécialité :
ED GEET : Ingénierie des PLASMAS

Unité de recherche :
LAPLACE

Directeur(s) de Thèse :

Jean-Pierre BOEUF et Laurent LIARD

Jury :
Anna LACOSTE, Professeur, LPSC, Univ Joseph Fourrier, Grenoble (Rapporteur)
Laïfa BOUFENDI, Professeur, GREMI, Univ Orléans (Rapporteur)
Olivier PASCAL, Professeur, UPS/LAPLACE, Toulouse (Président du jury)
Laurent LIARD, Maître de conférences, UPS/LAPLACE, Toulouse (Invited)
Jean-Pierre BOEUF, Professeur, UPS/LAPLACE, Toulouse (Directeur)

Acknowledgments

First of all, I would like to extend my sincere gratitude to Jean-Pierre Boeuf, for your instructive advice and useful suggestions on my thesis. I am deeply grateful of your help in the completion of this thesis. Thanks to you for giving me the opportunity to work on the plasma physics in the group of GREPHE of LAPLACE.

High tribute shall be paid to Laurent Liard, for your helpful discussion and guiding on my thesis. You never refused me on talking about the work, and never stingily show me the skills in research. Because of your appearance, I didn't felt lonely in my PhD thesis adventure. I owe you a lot.

Thanks to Gerjan Hagelaar, who always explained to me patiently on the details of the modeling. I have to say sorry for bothering you so much, especially when you were busy. Your humor is like your achievement on the modeling: génial.

I would like to thank the members of my jury: Pro. Ana Lacoste, Pro. Boufendi Laifa and Pro. Olivier PASCAL who report my thesis and allowed me to defend.

Also thanks to the other members in GREPHE: Leane Pitchford, Laurent Garrigues, Thiery, Bhaskar, Jose and Guenael for your help in both research and life.

Great thanks to Philippe and Jonathan, four years we spent almost every day together on the work, discussion, sports, lunch. This was an experience only lucky people can have, and these four years will be the most precious period in my memory. I would never forget the days we spent on the sailing, marathon, swimming.

Thomas, thank you for taking me to the sky; Amine, thank you for leading us to the mountain; Namjun, thanks for your Korean food; thanks to our lunch team: Carrina, Nicolas, Romain, Sedire, Raja, Constantin, Arsma, Olivier. Great thanks also goes to my dear Chinese friends: Yuan, Xiaolin, Yanling, Zhongxun, Lumei.

Thanks my grandparents and my parents, brother and my newborn nephew, my warm families, you are the power that encourage me to conquer any difficulties.

I would keep my deepest thanks to my beloved girl friend Yunhui, if I really got some achievement during years of my thesis work, I would say it was you. Thanks for all your support during my roughest time, it was because of you, that I didn't give up. I couldn't be happier without you. My thesis is accomplished, but our new life is just beginning.

Thanks to LAPLACE/GREPHE, It is here I met and knew many excellent people who work on the plasma physics and modeling, it is here I got familiar with plasma and enjoyed every small progress in understanding physics. My final thanks goes to China Scholarship Council, for the financial support in the last years.

Table of contents

Symbols and abbreviations

A	a constant; surface area (m^2)
B	a constant
[illegible]	Bessel function's solution
C	a constant
C	collision term of momentum equation
D	a constant
D	diffusion coefficient (m^2 /s) ; D_a, ambipolar diffusion coefficient (m^2 /s)
[illegible]	electric field (V /m), [illegible] microwave electric field (V /m)
E	energy threshold (J)
[illegible]	distribution function (m^{-6} s^3)
F	macroscopic forces including electromagnetic force and gravity forces (N)
g	gravitational acceleration constant
[illegible]	macroscopic forces (N)
G	charged particle flux (m^{-2} s^{-1})
[illegible]	plasma center-to-edge density ratio
[illegible]	magnetic field (A/m)
[illegible]	Hankel function of the first kind
[illegible]	Hankel function of the second kind
[illegible]	specific impulse (s)
[illegible]	identity matrix
[illegible]	Bessel function of the first kind
J	electrical current density (A /m^2)
[illegible]	wave number
[illegible]	thermal conductivity;
[illegible]	rate coefficient (m^3s^{-1})
L	length (m)
[illegible]	azimuthal mode number
[illegible]	mass of particle (kg), [illegible] electron mass ($9.11 \times 10^{-31}\, mg$), [illegible] ion particle

mass.

propellant mass flow rate (mg /s)

propellant mass (kg)

satellite total mass (kg)

M heavy particle mass (kg)

particle density (m^{-3}); , electron density; , ion density; , gas density

Bessel function of the second kind

integer; gas pressure (N /m^2)

power dissipated in the thruster (W)

pressure tensor (N /m^2)

electric charge (C)

heat flux (W /(m^2s))

quality factor of resonant cavity; collision cross section; , gas flow rate

radial position (m)

r particle position phase space

r direction component of

R radius (m)

source term (m^{-3} s^{-1})

Poynting vector (W / (m^2 s))

time (s)

T temperature (K)

thrust (N)

permeability (H/m); a constant, $\eta = \sqrt{\frac{2.3m}{M}}$, m is electron mass, M is xenon ion mass

particle mean velocity (m s^{-1})

u electron direct velocity (m/s)

vector potential (**A**, **F**)

v velocity (m /s)

v particle velocity phase space

space vehicle total velocity increment (m /s)

V electron thermal velocity (m/s)

rectangular coordinate (m)

radian frequency (rad /s)

collision frequency (s^{-1})

efficiency factor

particle mean energy (**J**)

collision cross section

light speed (m s^{-1}), heat capacity at constant volume for neutral particle

dielectric constant (F/m); vacuum permittivity ($8.854 \times 10^{-12} F/m$); plasma dielectric constant

volume charge density (C/m^3)

the root of the Bessel function of the order; momentum transfer frequency (s^{-1})

electrical conductivity ($\Omega^{-1} m^{-1}$)

angle (rad)

, first zero of the Bessel function

wave length (m); , ion mean free path (m)

fraction

, correcting factor

potential (V)

net power density gain/lost in collisions (W)

N the number of particles created in one collision

electric scalar potential

x direction component of

angular direction component of

Λ diffusion length (m)

V volume (m^3)

charged particle flux (m^{-2} s^{-1})

General introduction

The work presented in this manuscript has been performed in the context of the research activities of the GREPHE/LAPLACE group on electric propulsion for space vehicles. It is focused on one particular aspect of electric propulsion, related to the electron source required to neutralize the ion beam generated in electrostatic thrusters.

Electric propulsion (EP) is the "acceleration of gases for propulsion by electrical heating and/or by electric and magnetic body forces" (G. Jahn, in *Physics of Electric Propulsion*", McGraw-Hill Book Company, 1968).

Electric propulsion systems for satellites or other space vehicles has a number of advantages over chemical propulsion, the most important being that they can allow much higher propellant velocities than chemical engines, leading to considerable propellant mass saving and launching cost reduction. The thrust of plasma thrusters is lower but a combination of low thrust and high specific impulse is sought in several types of missions such as orbit insertion, attitude control, and drag compensation.

There are three categories of electric thrusters: electrothermal, electrostatic, and electromagnetic thrusters. In electrothermal thrusters, the gas is electrically heated and expanded through a nozzle. In electrostatic thrusters ions are extracted and accelerated out of a plasma source, providing the thrust (these thrusters can be considered as ion sources). In electromagnetic thrusters, the thrust is created by the interaction of an applied electric field and an induced or applied magnetic field resulting in a JxB accelerating force on the plasma. A particular class of thrusters, the Hall thrusters can be considered both as electrostatic and electromagnetic thrusters.

In electrostatic thrusters, the flux of positive ions extracted from the plasma source must be balanced by an equal flux of electrons (otherwise the satellite would charge negatively). The electron flux must be provided by an electron source, also called "neutralizer". Very efficient neutralizers based on thermoionic hollow cathode discharges have been developed over the years. Some of these cathodes are able to provide tens of amperes of electron current. Hollow cathode neutralizers are used on most Hall thrusters and gridded ion sources. The critical issues of the thermionic hollow cathodes are possible failures of emitter and heater, lifetime limitation, high sensitivity of emission properties to various contaminations (the emissive material of these cathodes is often very sensitive to oxygen contamination). The sensitivity to oxygen contamination can become a serious issue for the use of electric propulsion on low orbit satellites. For these reasons, research on alternative electron sources not requiring high temperature electron emission is still an important topic and several experiments aimed at demonstrating the feasibility of efficiently extracting large electron currents from a plasma source have been developed. **The work presented in**

this thesis is devoted to the modeling of a resonant cavity microwave electron source that has been recently proposed by K.D. Diamant in the context of electric propulsion (references in the next chapters).

Although a number of models of microwave discharges have been developed in the context of different applications, there is no published model of a resonant cavity microwave discharge in the conditions of a neutralizer for space propulsion applications. The aim of this work is therefore 1) to better understand the plasma generation under conditions similar to those of Diamant, 2) to provide quantitative information on the plasma characteristics (plasma density, electron temperature, etc…) and source efficiency and to compare them with available experimental results, and 3), to understand and describe qualitatively and quantitatively the issues related to electron extraction from the source and to extraction efficiency.

The resonant cavity microwave source discussed in this thesis operates in xenon, at a gas pressure around 100 mtorr. In these conditions, the dimensions of the source are much larger than the particle mean free paths and the model used in this work is therefore based on a fluid description of the plasma particles.

The thesis is divided in 5 parts:

In **chapter 1**, we present a brief general overview of electric propulsion and electron neutralizers.

In **chapter 2,** the fluid model of the microwave discharge (two-dimensional and global, zero-dimensional model), its approximations, as well as the question of microwave energy coupling to the plasma are discussed and described.

In **chapter 3,** we describe and characterize the resonant cavity microwave source and discuss the ability of the cavity to store microwave energy. The role of the Q factor of the cavity is described and discussed on the basis of calculations performed both with commercial simulator (HFSS, High Frequency Structure Simulator) and using a FDTD, Finite Difference Time Domain model. Then we describe the parameters controlling the electromagnetic field distribution in the cavity prior to plasma formation and study the conditions of resonance that are sought for to optimize gas breakdown. We also describe the ignition phase of the discharge and the plasma formation, and discuss the best operating conditions (gas pressure) for breakdown.

C**hapter 4** is devoted to the description of the plasma properties based on the results from the global and 2D fluid models of the microwave discharge

Chapter 5 focuses on the issues related to electron extraction form the microwave plasma source.

Chapter 1: Electric thrusters and neutralizers for space propulsion

We present in this chapter a brief introduction to electric propulsion. Since the main topic of this thesis is the study of a plasma cathode as an alternative to thermoionic hollow cathode neutralizer for electric thrusters, we also present a brief overview of electron sources in the context of space propulsion.

1.1 Electric propulsion

Electric propulsion is a technology aimed at achieving thrust with high exhaust velocities, which results in a reduction in the amount of propellant required for a given space mission compared to other conventional propulsion methods. The basic idea is that in electric thrusters, the propellant (plasmas, ions) can be electrically accelerated and therefore reach much higher velocities than in conventional, chemical propulsion. A space mission is characterized by the total velocity increment ΔV provided by the propulsion system to the space vehicle during the time of the mission. From the mass conservation equation, one can deduce a simple law giving the mass of propellant M_p needed for a given total velocity increment, as a function of the exhaust velocity of the propellant v_e, and for an initial total of the satellite M_0. This law is the well-known Tsiokovsky's equation, which can be written as:

$$\frac{M_p}{M_0} = 1 - \exp\left(-\frac{\Delta V}{v_e}\right) \tag{1.1}$$

It is clear from this equation that, for a given total velocity increment, the needed mass of propellant decreases when the propellant velocity increases. For this reason, electric thrusters can allow a considerable reduction of the needed propellant mass, with respect to chemical thrusters (the propellant velocity in electrical thrusters can be as large as 20 or more km/s, while it is only a few km/s in chemical engines).

Reduced propellant mass can significantly decrease the launch mass of a spacecraft or satellite, leading to important saving costs.

In general, electric propulsion (EP) encompasses any propulsion technology in which electricity is used to increase the propellant exhaust velocity. There are many figures of merit for electric thrusters, but mission and application planners are primarily interested in thrust T, specific impulse I_{sp} and total efficiency in relating the performance of the thruster to the delivered mass and change in the spacecraft velocity during thrust periods. Thrust is directly related to the propellant mass flow

rate $\dot{m}$ and to the exhaust velocity and is given by:

(1.2) $$T = \dot{m} \mathrm{v}_e$$

Specific impulse, I_{sp} is defined as the propellant exhaust velocity divided by the gravitational acceleration constant g,

(1.3) $$I_{sp} = \frac{\mathrm{v}_e}{g}$$

The specific impulse is expressed in seconds and is completely characterized by the velocity of the propellant. The total efficiency η is the jet power produced by the thrust beam divided by the electrical power into the system.

(1.4) $$\eta = \frac{\dot{m}\mathrm{v}_e^2}{2P_a} = \frac{T^2}{2\dot{m}P_a} \equiv \frac{T\mathrm{v}_e}{2P_a}$$

Where P_a is the power dissipated in the thruster.

Naturally, spacecraft designers are then concerned with providing the electrical power that the thruster requires to produce a given thrust, as well as with dissipating the thermal power that the thruster generates as waste heat. An electric thruster can achieve specific impulses in the range 1500-3000 s (i.e. velocity of the propellant on the order of 15-30 km/s). This is much higher than the specific impulse of conventional chemical engines. On the other hand the thrust of electric thrusters is generally small, on the order of 100 mN on electric thrusters that are used for satellite station keeping and orbit control (power in the kW range). Plasma thrusters actually constitute a very large family, with powers ranging from 200 kW (VASIMR developed by Franklin Chang-Diaz [1]) to 10 W (Miniature ion propulsion, by Hiroyuki KOIZUMI, et al. [2]).

1.1.1 Brief history of EP (Electric propulsion)

As early as 1906, Robert Goddard (1882 - 1945) was the first to demonstrate the attractiveness of Electrical Propulsion [3]. He noted that charged particles could be accelerated to high speed, which is not possible with chemical propulsion due to wall heating issues. He concluded that electrically accelerated particle systems could provide high exhaust velocity propulsion systems. He also envisioned the utility of electrical propulsion for interplanetary transfers.

Later followed the work of Tsiokovsky (1911), Oberth [5]-[6] and Stuhlinger [7]. The U.S. ambition in space rapidly helped research in Electrical Propulsion thrive. Those

systems have existed now for more than 40 years. Electrical Propulsion was first tested in the early 1960s. In the 1980s, the US used electrical propulsion on communication satellites (e.g. the Iridium satellite constellation), but only as a station keeping and attitude control option. They have only been used as a primary propulsion system since the late 1990's, mainly because of a lack of confidence in those systems. The electric propulsion history is shortly summarized in *Table 1*.

However, those systems are far more efficient than conventional chemical propulsion systems. They allow bigger ΔV , allowing more complex missions.

1903	**K. E. Tsiolkovsky**	Derived the "Rocket" Equation commonly used to show the benefits of electric propulsion
1906	**R. Goddard**	Wrote about the possibility of electric rockets
1911	**K. E. Tsiolkovsky**	Independently wrote about electric rockets
1929	**V. P. Glushko**	World's first electric thruster demonstrated at the Gas Dynamics Laboratory in Lenningrad
1960	**Glenn Research Center**	First "broad-beam" ion thruster operated in the U.S. at the NASA Lewis (now Glenn) Research Center
1964	**U.S. and USSR**	First successful EP tests in space
1972	**USSR**	First operation of a xenon stationary plasma thruster (SPT-50) in space (Meteor)
1993	**U.S.**	First use of hydrazine arcjets on a commercial communications satellite (Telstar 401)

Table 1: A short summary of the EP history [8].

1.1.2 Classification of EP (Electric propulsion)

Electric thrusters are classically divided in three categories:

- Electrothermal: in this category, thrust is provided by the expansion of a heated gas through a nozzle (as in chemical thrusters), except that the heating of the gas is provided by a plasma source, e.g. an arc (arc jet) [9].
- Electromagnetic: in electromagnetic thrusters, a plasma is subject to the Lorentz force due to an external magnetic field or to the magnetic field generated by the plasma current itself. The extraction of the plasma particles by the Lorentz force provides the thrust [10].
- Electrostatic: in electrostatic thrusters, positive ions are extracted from the plasma source and provide the thrust. Ion extraction can be performed through a grid negatively biased with respect to the plasma. The extracted ion beam must be neutralized by an electron source [11][12].

Note that some very successful electric thrusters, the Hall thrusters, can be qualified as Electrostatic as well as Electromagnetic thrusters. In these thrusters, positive ions are not extracted from the plasma by a system of biased grids, but they are extracted by the electric field generated in the plasma by a local reduction of the electron conductivity induced by an external magnetic field placed in the direction perpendicular to the cathode-anode path (axial direction). The axial electric field must increase in the region of large (radial) magnetic field to maintain current continuity. In that sense Hall thrusters can be qualified as electrostatic thrusters (or ion sources). Another way to describe the thrust of an electric thruster is to say that the thrust is due to the reaction of the engine to the Lorentz force acting on the electron Hall current (the current in the azimuthal direction due to the ExB motion of the electrons). In that sense, the Hall thrusters belong to the Electromagnetic thruster category. It is easy to show that these two descriptions of the thrust in a Hall thruster (force on ions due to the generated electrostatic field, or reaction to the magnetic force on the electron Hall current) are fully equivalent.

Some electric thrusters are specifically designed for micro-propulsion (thrust in the micro to milli-Newton range). These include for example the Field Emission, colloid thrusters and are often considered as a fourth category.

The different types of thrusters in this classification are represented in Table 2.

Electro**static**	Electro**magnetic**
DC-discharge ion thruster[13]	Helicon plasma ion thruster
Microwave plasma ion thruster	Inductively coupled plasma (ICP) ion thruster
Radiofrequency(RF) plasma ion thruster [14]	Electron-cyclotron-resonance plasma (ECR) ion thruster[15]
Hall Effect (SPT,TAL) plasma thruster	Variable specific-impulse plasma thruster
Electro**thermal**	Electric **Micro-Propulsion**
Resistojet	Colloid ion[19]
Arcjet	
Radiofrequency(RF) electrothermal plasma thruster	Field Emission (FEEP)[16][17]
Microwave electrothermal plasma thruster	Pulsed plasma thruster (PPT)[18]
Pulsed electrothermal	Miniature-**plasma** thruster

Table 2: The different categories of electric thrusters.

The specific impulse and the thrust range covered by the different thrusters are shown in Figure 1.1.

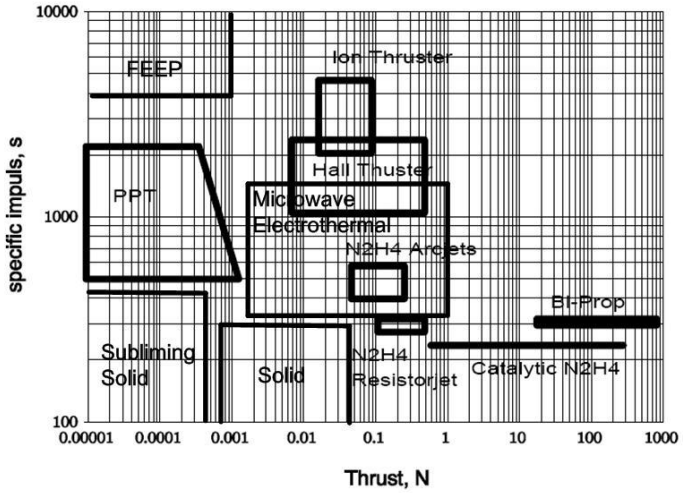

Figure 1.1: Operating Range of Specific Impulse VS. thrust for potential electric propulsion concepts; Some chemical propulsion concepts (solid, Mono-prop, Bi-prop) are also indicated on the figure [22].

Electric thrusters cover the low-thrust, high-Specific Impulse range of Figure 1.1.

This corresponds typically to input power between 0.5 mW and 10 kW, thrust in the 0.1μN-200mN range, specific impulse from 1000 s to 10000 s, and efficiency in a large range between 5% and 90%.

The specific demand of micro-propulsion

Nowadays, more and more demand comes from the "Small Satellites" to use the micro-propulsion as the primary on-orbit propulsion.

In order to spread the risk of deployment and to reduce the costs associated with satellite launch and operation, it is imperative to reduce satellite size by at least an order of magnitude. The satellites with the mass less than 500 kg are defined as "Small Satellites", the classification of the satellites is shown in Table 3.

The micro-propulsion is the propulsion system used on small spacecraft (< 500 kg), with small thrust level (μN~mN), low propellant mass (few 100 g). Such a low thrust level can be achieved by developing **Chemical** micro-propulsion (Cold Gas, Mono-propellant, Bi-propellant, etc.) or by **Electric** micro-propulsion (Colloid, PPT, FEEP, Miniature-plasma thrusters in table 2).

Up to now, the available electric power onboard of the satellites has been around 1 W/kg. To enable an order of magnitude reduction in spacecraft size while retaining mission capabilities, nothing less than revolutionary developments in propulsion technology are needed. Such developments have not been forthcoming, most likely because the emphasis on microspacecraft is just starting. The need for innovative technologies is graphically represented in Figure 1.2. Some existing spacecraft are shown, from the 12kg, 0.006 kW Microsat-I (no propulsion) to the 10.8 metric ton, 4.3 kW Hubble. At the low mass/power end of the graph, an area exists where, depending on mission requirements, spacecraft propulsive needs may be met with scaled down versions of conventional propulsion systems.

Group name	**Wet Mass**	
Large satellite	>1000kg	
Medium sized satellite	500-1000kg	
Mini satellite	100-500kg	Small Satellites
Micro satellite	10-100kg	
Nano satellite	1-10kg	
Pico satellite	0.1-1kg	
Femto satellite	<100g	

Table 3: The classification of satellites [20].

The boundaries of this "technology barrier" are not well defined. To overcome this

"technology barrier", may require revolutionary technologies such as "microelectromechanical systems (MEMS) technology". Both chemical and electric propulsion concepts could benefit from this technology, e.g. Aleksander Grm *et al.* they started the first MEMS thruster operation in 2005, and the first MEMS thruster was launched in 2010 [21].

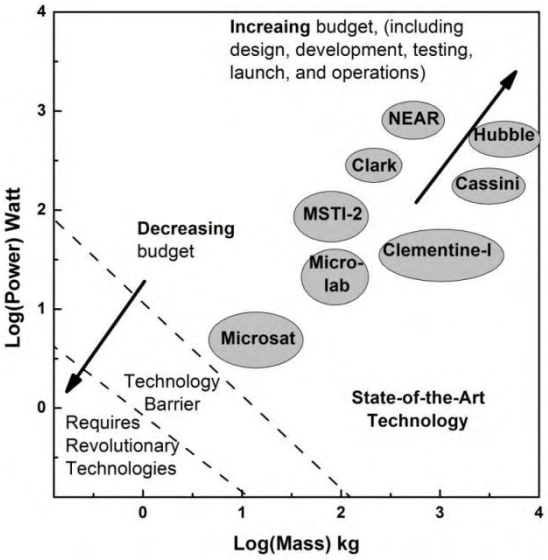

Figure 1.2: Technology Requirements for Small satellite [23].

1.2 Neutralizers for electron propulsion

In this section we focus on electron neutralizers for space propulsion applications. Ion thrusters such as Hall thrusters or gridded electrostatic thrusters require the presence of an electron source to neutralize the ion beam and keep the satellite charge constant. In some specific thrusters such as the Hall thrusters, the electron source is also used to provide the current to maintain the plasma of the ion source. In a Hall thruster, typically 25% percent of the current from the electron source is used to generate the plasma, and 75% to neutralize the ion beam current. For example, in a 1 kW Hall thruster operating in xenon under a mass flow rate of 5 mg/s and an applied voltage of 300 V, the ion current at exhaust is about 4 A. The neutralizer must provide 1 A to maintain the discharge, and 4 A to neutralize the ion beam [24].

The most commonly used electron sources for ion beam neutralization are thermoionic hollow cathodes. These sources use very low work function emitters such as LaB_6. Large electron currents can be emitted by small surfaces of these emitters when their temperature is sufficiently high. The cathode emitters are first heated by an external source. On the plasma is formed, their high temperature can be maintained by the large flux of ions returning to the cathode. These source are very efficient but are sensitive to contamination and their lifetime may be reduced under specific environments. This is the reason why research has been devoted to the development

of alternative plasma electron sources that do not use electron emission [25].

After a brief summary of the design and properties of thermoionic hollow cathodes (section 1.2.1), we describe different types of plasma sources that could be used as alternative to hollow cathodes. In the rest of this thesis, we study one particular type of electron source based on a microwave plasma. This source is described in section 1.2.2.

1.2.1 Thermoionic hollow cathode neutralizers

Thermoionic hollow cathode neutralizers are described in details in the book by Goebel and Katz [24]. In this section we only give a short introduction to this type of electron source.

Figure 1.3 shows a typical thermoionic hollow cathode geometry. The hollow cathode consists of a hollow refractory tube with an orifice plate on the downstream end. The tube has an insert in the shape of a cylinder that is placed inside the tube and pushed against the orifice plate. This insert is the active electron emitter, and can be made of several different materials that provide a low work function surface on the inside diameter in contact with the plasma. The cathode tube is wrapped with a heater that raises the insert temperature to emissive temperatures to start the discharge. Once the plasma is formed, the heater is turned off, and the hollow cathode operates in a "self-heating" mode and the insert is heated by charged particle bombardment.

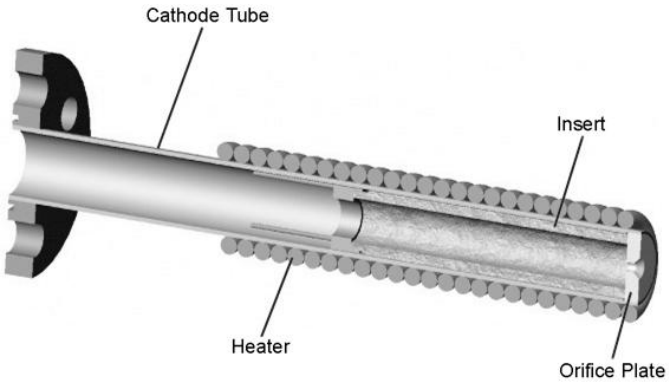

Figure 1.3 Typical hollow cathode geometry of a refractory metal tube with an emissive insert inside and a heater wrapped on the outside [24].

There are three self-heating mechanisms possible in hollow cathodes: (1) orifice heating(or aperture heating), (2) ion heating, (3) electron heating. The heating mechanisms are important for the hollow cathode design, because with different hollow cathode geometry, the heating mechanisms can be totally different.

The first heating mechanism(orifice heating) normally happens in the hollow cathodes designed with a small, restrictive orifice (high length-to-diameter ratio), which produces a high internal pressure in both the insert and orifice region. The

plasma discharge passing through the orifice is then very resistive, causing a significant amount of power to be deposited in the orifice plasma and transferred to the orifice walls by convection. This power deposition then heats the insert by conduction and radiation. Hence orifice heating is used primarily in neutralizer cathodes where the discharge currents are very low. **The second heating mechanism(ion heating)** is the classic mechanism for cathode heating, the ions flux in the cathode insert region plasma fall through the sheath potential at the insert surface and heat the surface by ion bombardment. **The third heating mechanism (electron heating)** occurs in a regime where both the cathode internal pressure and the discharge current are relatively high, resulting in the very high plasma densities ($>10^{21}$ m^{-3}) generated in the insert region. The low electron temperature and low sheath voltages produced in this situation result in the energetic tail of the Maxwellian electron distribution having sufficient energy to exceed the sheath potential and reach the insert surface, hence these electrons deposit their energy on the insert and heat it to emission temperatures. The dominating heating mechanism depends on the orifice geometry designed for different internal neutral gas pressure and discharge current.

As shown in Figure 1.4 (a),the orifice with a high length-to-diameter ratio, produces high internal gas pressure and **relatively low current**, the dominating heating mechanism is orifice heating.

Figure 1.4 (b)shows the orifice geometry for a cathode operating at lower internal pressure. This orifice has a diameter typically larger than the length. The heating mechanism in these cathodes can be ion heating or electron heating, or a combination of them, depending on the orifice size and operating conditions.

Figure 1.4 (c)shows the cathode has essentially no orifice at all, typically has a high neutral gas pressure gradient and produces **relatively high current**, the dominating heating mechanism is ion heating.

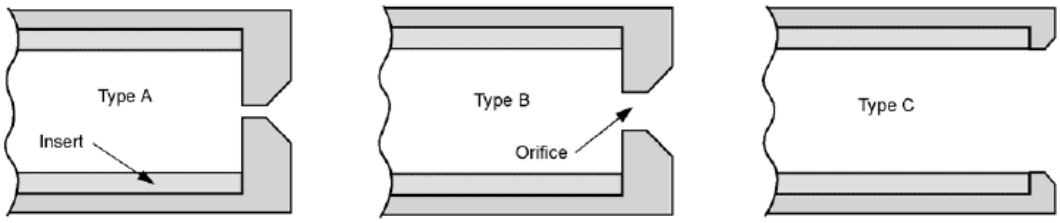

(a) (b) (c)

Figure 1.4 Schematic of the three characteristic types of hollow cathodes, depending on the orifice geometry [24].

Figure 1.5 shows axial plasma density profiles for a 0.38 cm inside-diameter cathode insert, operating at 13 A of discharge current and a xenon gas flow rate of 3.7 sccm (0.36 mg/s) for the different orifice geometries of Figure 1.4. As the orifice diameter

increases, the plasma density gradient decreases, due to the different heating mechanisms.

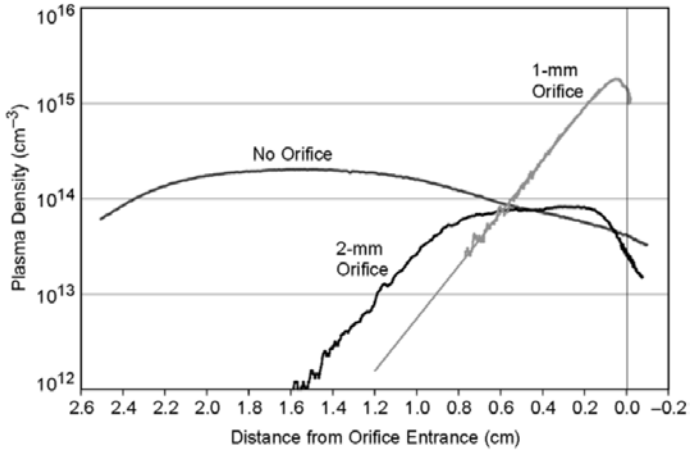

Figure 1.5: Cathode plasma density profile examples as the orifice diameter is increased for a constant discharge current and flow rate [24].

Indeed, the operating regime for a given cathode geometry can evolve from low resistive heating in the orifice at low currents and low gas flow rates to substantial resistive heating and plasma generation at high current and high gas flow rates.

The material of the insert (emitter) is crucial to determine the hollow cathode performance and lifetime. Common options of the materials are: Refraction metal (Tantalum, Tungsten), lanthanum hexaboride (LaB_6),barium oxide (BaO).

	A	*D*	ϕ
BaO-Scandate [11]	120	—	$8 \times 10^{-7} T^2 - 1.3 \times 10^3 T + 1.96$
BaO-W 411 [12]	120	—	$1.67 + 2.82 - 10^{-4}\, T$
BaO-W 411 [10]	—	1.5	1.56
LaB_6 [13]	—	29	2.66
LaB_6 [14]	—	110	2.87
LaB_6 [15]	120	—	2.91
LaB_6 [8]	120	—	$2.66 + 1.23 \times 10^{-4}\, T$
Molybdenum [8]	—	55	4.2
Tantalum [8]	—	37	4.1
Tungsten [8]	—	70	4.55

Table 4: Work function (ϕ) for several cathode materials[24].

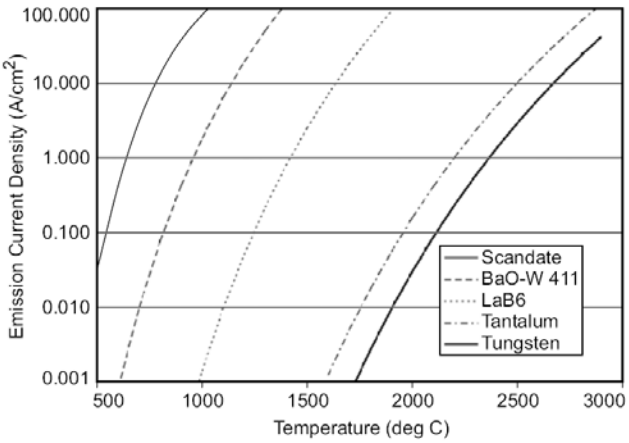

Figure 1.6: Emission current density versus temperature for various cathode materials [24].

Table 4 lists the work function (ϕ) of summarized cathode materials, and *Figure 1.6*shows the emission current for several different emitter materials:

Refractory metal cathodes have very high work function (over 4 eV), and requires high temperature (more than 2500 ^{o}C) to maintain high current density.

Barium oxide (BaO) cathodes can give very low work function (under 2 eV), are capable of producing high current densities under low temperature (under 1000 ^{o}C), but require extremely high feed gas purity (e.g. 99.9995% xenon purity on board) to avoid chemistry poisoning.

Lanthanum hexaboride (LaB_6) cathodes have moderate work function (~2.6 eV), can emit over 10 A/cm^2 current at a temperature of 1650 ^{o}C, are commonly used in electric propulsions with Hall thrusters. They are less sensitive to the feed gas purity and air exposure than BaO cathodes, but in specific environment (such as LEO orbit), the cathodes are sensitive to contamination due to the air exposure.

1.2.2 Other electron sources

Thermoionic hollow cathodes are commonly used as neutralizers in electric propulsion because they can achieve high electron emission current at low power and with low gas consumption. However their lifetime is limited by the degradation of the thermoionic emitter and by possible failures of the emitter and heater. Moreover, the emitters are very sensitive to various contaminations. For these reasons and in spite of the very high efficiency of thermoionic hollow cathodes, the research on alternative electron sources is still active and papers are presented on this topic at each propulsion conference.

Knowing that it is difficult to compete with thermionic hollow cathodes in terms of energy cost per extracted electron, it is however interesting to study the possibilities

and limitations of an electron source operating without emitter. The different questions that arise when designing a plasma source for electron extraction are:

- choice of plasma excitation among different possibilities: RF inductive, helicon, microwave, ECR, …
- operating conditions: gas pressure (xenon is generally used since most electric thrusters use xenon)
- extraction system: dimension of the aperture for electron extraction (this is also related to gas pumping, flow rate and operating gas pressure in the source)

Different electron sources for space propulsion have been developed and tested by different authors. These include helicon rf plasmas [26]-[28], microwave resonant cavity plasma sources [29]-[32], microwave plasmas at ECR (electron cyclotron resonance) discharges [33]-[37], and ICP (inductively coupled RF plasmas) sources [38][39]. Of course, for space applications, simplicity is an important key-word and sources using large magnetic fields such as helicons or ECR are not very appealing since the magnetic circuit adds complexity and weight. Two types of plasma cathodes, based on ICP and microwave have attracted more attention as possible candidates for electron neutralizers in space applications. In this thesis we have chosen to study a microwave source for specific reasons related to the research strategy in LAPLACE, but ICPs are also very good candidates for this application. The main points that can guide the choice between microwave sources and ICP for space propulsion are related to the simplicity and efficiency of the power coupling to the plasma, and the weight and cost of the power unit. The discussion of these questions is outside the scope of this thesis, and we concentrate here on the physics of the sources.

In this section we briefly describe the operation of an ICP and a microwave electron sources on the basis of recently published papers. The rest of the thesis will be focused on the theoretical and numerical study of the microwave source developed and tested by Diamant [29]-[31].

ICP electron source

Figure 1.7 shows an ICP source recently developed in Japan [38][39] to be used as an electron source for space propulsion applications. The plasma vessel is a cylinder of radius 2 cm and length 2.5 cm. The chamber walls are in alumina but an ion collector is inserted in the discharge volume (see Figure 1.8). The presence of an ion collector is necessary otherwise it would be impossible to extract electrons from the source.

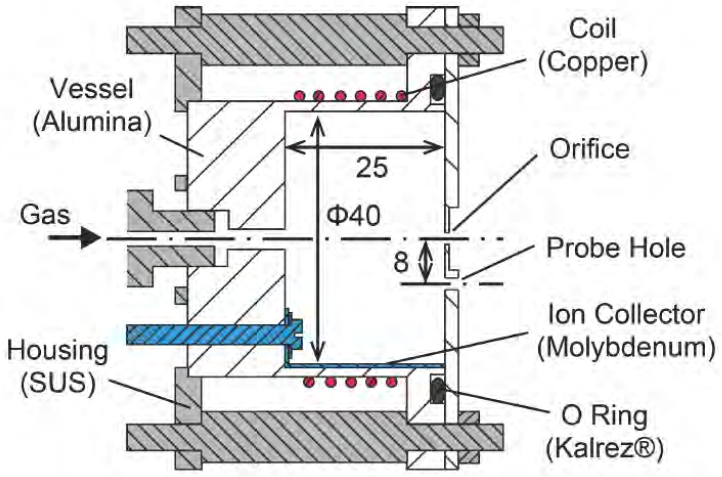

Figure 1.7: ICP electron source developed by Nakabayashi et al. [38][39]. The lengths are in mm.

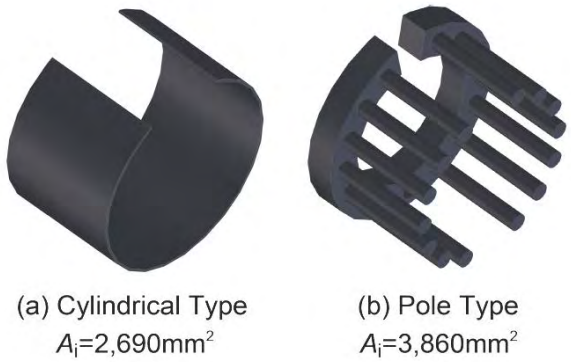

Figure 1.8: Two different forms of ion collector to be inserted in the ICP volume [38][39].

Two important (and sometimes independent) issues must be considered when designing an electron source. The first one is related to the ignition of the plasma and the second concerns the efficiency of the source in steady state operation, i.e. the energy cost per electron extracted and the efficiency of ionization of the injected gas flow. Figure 1.9 shows the measured minimum ignition power as a function of xenon mass flow rate for different configurations of the ion collector and for different dimensions of the electron extraction aperture. We see that there is a minimum gas flow rate below which it is not possible to initiate the plasma and that this minimum power depends on the ion collector geometry (the presence of the ion collector decreases the efficiency of the power coupling in the plasma). The minimum ignition efficiency is also strongly dependent, for a given xenon mass flow rate, on the size (radius and thickness) of the extraction orifice. This is because, for a given mass flow

rate, the size of the aperture controls the pressure inside the discharge chamber. We see on Figure 1.9 that the minimum ignition power for a given mass flow rate is lower for lower radii of the aperture, and this can be explained by an increase of the pressure in the chamber when the radius decreases.

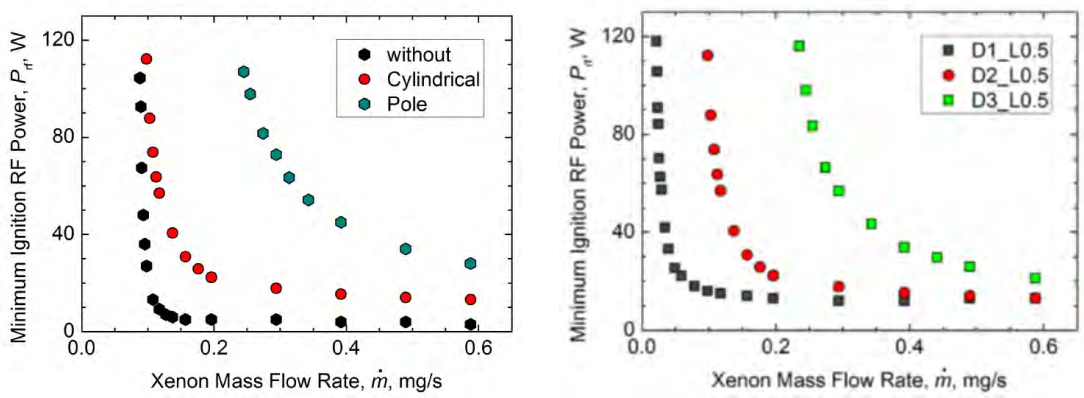

Figure 1.9: Minimum ignition power as a function of xenon mass flow rate for different forms of the ion collector (left) and for different dimensions of the extraction aperture (diameter D and length L in mm, e.g. D_2L0.5 corresponds to an aperture of diameter 2 mm and length 0.5 mm) (after Nakabayashi et al. [39]).

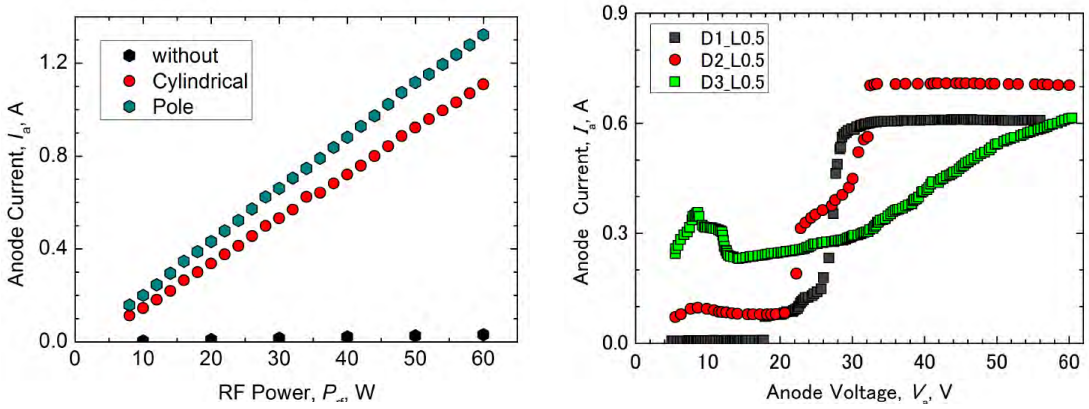

Figure 1.10: Extracted electron current as a function of RF power for a 40 V extraction voltage, a 0.15 mg/s xenon mass flow rate, and for different forms of the ion collector (left), and as a function of extraction voltage for different aperture dimensions at 40 W RF power and 0.15 xenon mass flow rate (right) (after Nakabayashi et al. [39]).

Figure 1.10 shows that the extracted electron current increases quasi-linearly with injected RF power (and that no electron current can be extracted if no ion collector is present in the chamber). We also see on this figure that the anode voltage necessary to extract the maximum possible electron current is larger for larger diameter of the extraction orifice. This result is quite intuitive but we will see in chapter 5 that this

can be explained with a simple analytical model. Finally, an important result of Figure 1.10 is that the cost of extracting 1 A of electron current is on the order of 50 eV in the conditions of the experiments (one can also infer from the figure that the extracted current is proportional to the power, with a slope around 20 mA/W).

The measured plasma density and electron temperature in the plasma source are on the order of 10^{19} m^{-3} and 1 eV respectively, as seen on Figure 1.11, and are not strongly dependent on the gas pressure in the considered range (between 10 Pa and 80 Pa).

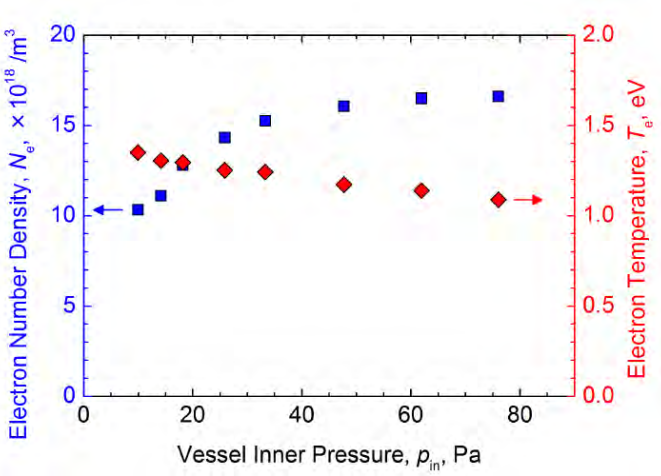

Figure 1.11: Measured plasma density and electron temperature as a function of pressure in the discharge chamber at 20 W of RF power and with a 2 mm orifice diameter (after Nakabayashi et al. [39]).

Microwave electron source

An alternative to an ICP source is a microwave source. A microwave plasma has been recently studied and proposed as an electron source in the context of space propulsion by Diamant[31]. In this thesis we will focus on this particular source and try to simulate and understand its properties.

A schematic of Diamant's microwave source is displayed in Figure 1.12, and a photo of the source on operation is shown in Figure 1.13. The plasma is generated in a microwave cavity using a 5.8 GHz magnetron. The microwave in introduced through a rigid coaxial cable and the cavity was tuned by varying the cavity of length and the depth of insertion of the coupling antenna. The experiments were performed first without a magnetic field [29][30][31], and, in a second paper, with a confining axial magnetic field [32]. The discharge chamber was a cylinder of approximately 10 cm length and 4 cm in diameter. The chamber was separated from the microwave injection system by an alumina (or sapphire or fused silica) separation plate. Figure 1.14 shows the design of the electron extraction system. Different extraction apertures were tested, the best results being obtained for extraction aperture diameters D of 4.1

and 5.8 mm (the thickness of the extraction aperture is about 1 cm).

The plasma was generated in xenon, with mass flow rates between 0.3 and 1.5 mg/s. Under these conditions of flow rates and aperture dimensions, the gas pressure inside the discharge chamber should be in the 100 mtorr range without plasma.

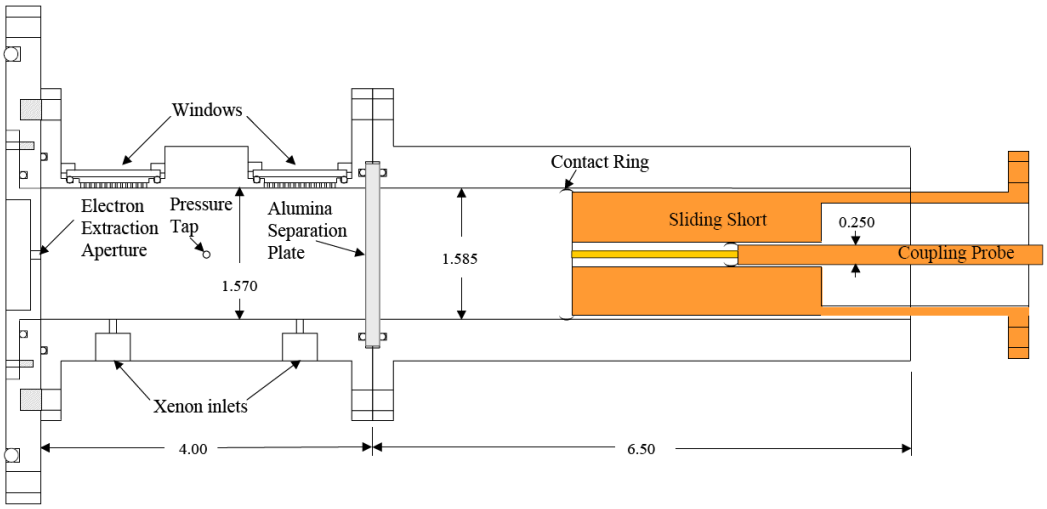

Figure 1.12: Scheme of the microwave electron source of Diamant. The dimensions are in inches [29]

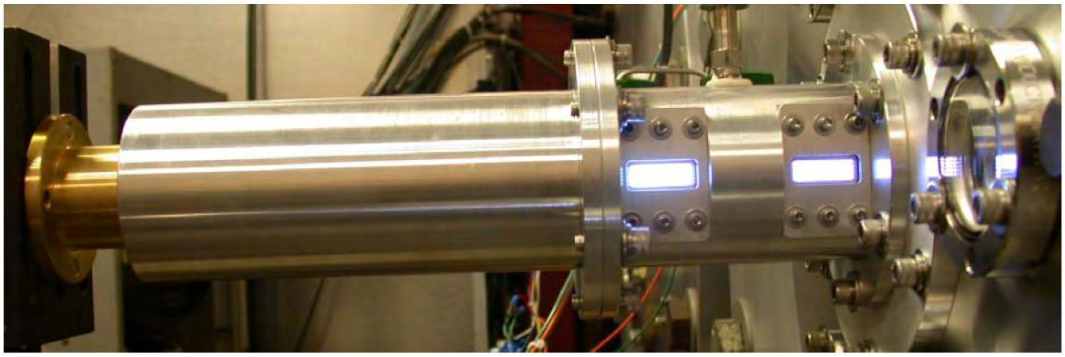

Figure 1.13: Microwave plasma source of Diamant [29] in operation.

After the extraction aperture, an intermediate electrode called the keeper can be used to maintain the current (see Figure 1.14). This electrode can help extract the current at low anode bias voltage but its influence on the discharge is not perfectly clear.

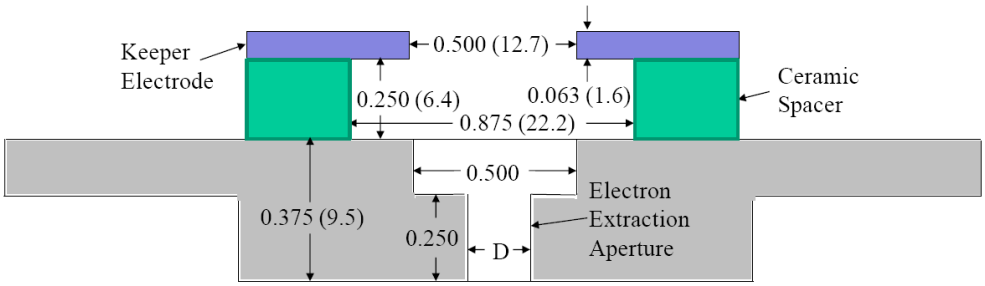

Figure 1.14: Enlarged section view of extraction aperture and keeper, dimensions in inches (mm) (after Diamant [29]).

In this configuration, Diamant reports extracted electron currents on the order of 30 mA/W, e.g. 2 A for 60 W absorbed power, as shown in Figure 1.15. This is significantly larger than the 20 mA/W reported by Nakabayashi et al. [39] in their ICP electron source (see Figure 1.10 and discussion above).

Note that most of the previous papers on electron sources in xenon give maximum extraction efficiencies of about or less than 20 mA/W (low frequency RF source of Godyak et al.[40], helicon source of Longmier and Hershkowitz [26][27], RF inductive of Nakabayashi et al.[39], ECR source of Edgar and Bilen, Hidaka et al., Weatherford and Foster [33]-[37]). The reason for the higher efficiency of Diamant's source is not clear. Moreover, when a large axial magnetic field is used to better confine the electrons, Diamant reports electron extraction efficiencies as large as 90 mA/W [32].The magnetic field was as large as 3 T in some regions of the discharge chamber, so ECR was in principle possible but it is not clear if it had a significant influence on the reported high electron extraction efficiency.

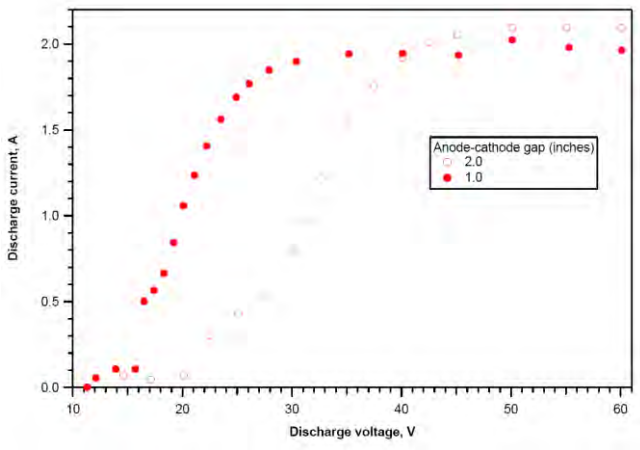

Figure 1.15: Extracted electron current as a function of anode voltage in the microwave source of Diamant for two different positions of the anode. The absorbed microwave power is 60 W and the xenon flow rate is 0.75 mg/s.

1.3 Conclusion

In this chapter we have presented a brief introduction to electric propulsion of the cathodes used as neutralizers in space applications.

The thermoionic hollow cathodes are very efficient electron sources that can deliver very large electron currents at a low energy cost and in a small volume. Although it is difficult to compete with these source in terms of efficiency and source volume, alternative electron sources may be necessary to increase the lifetime or under conditions where contamination of the emitter may be a problem.

Different plasma sources have been studied as electron sources for neutralization in electric space propulsion applications. These sources include RF inductively coupled, helicons, ECR, and microwave plasmas. The efficiency of these sources is limited by the cost to generate an electron-ion pair lost to the walls or electrodes. Typically, in xenon plasmas, electron extraction efficiencies on the order of 20 mA/W have been demonstrated in these different sources. In this thesis we will focus one particular source, a microwave source, developed by Diamant. Diamant has reported specially high efficiency, on the order of 30 mA for a microwave source and as much as 90 mA/W for a microwave source with magnetic confinement.

1.4References

[1] Squire, J. P, et al. VASIMR®VX-200 Operation at 200 kW and Plume Measurements: Future Plans and an ISS EP Test Platform. *32nd International Electric Propulsion Conference*. Wiesbaden, Germany. (2011)

[2] Hiroyuki, K., K. Kimya, et al., Development of the Miniature Ion Propulsion System for 50 kg Small Spacecraft. *48th AIAA/ASME/SAE/ASEE Joint Propulsion Conference & Exhibit*, 29 July - 1 August 2012, Atlanta, Georgia

[3] Jahn, G. R. and E. Y. Choueiri, Eds., *Encyclopedia of Physical Science and Technology*. (Chapter Electrical Propulsion, Academic Press, 2002).

[4] Tsiolkovsky, K. E. *Investigation of Outer Space Rocket Devices*. (1911)

[5] Oberth, H., Ed. *The electric spaceship*. (Wright-Patterson Air Force Base, Ohio, Aerospace Technical Intelligence Center, 1960).

[6] Oberth, H., Ed., *Ways to spaceflight.* (Washington, DC National Aeronautics and Space Administration, 1972).

[7] Stuhlinger, E., Possibilities of Electrical Space Ship Propulsion. *International Astronautical Congress*. 1955, Vienna

[8] Palaszewski, B., Electric Propulsion for Future Space Missions. (NASA Glenn Research Center at Lewis Field, unpublished, 2003)

[9] Butler, G. W., Converging constrictor for an electrothermal arcjet thruster. (1999)

[10] M. Andrenucci, F. P., A. Turco, et al., Plasma Diagnostics in MPD Thruster Plumes. *22nd International Electric Propulsion Conference*. Oct, 1991, Viareggio, Italy

[11] Kuninaka, H. and S. Satori., Development and Demonstration of a Cathodeless Electron Cyclotron Resonance Ion Thruster. *Journal of Propulsion and Power*. Vol. 14, 1022-1026 (1998)

[12] Tajmar, M. and J. Wang. Three-Dimensional Numerical Simulation of Field-Emission-Electric-Propulsion Backflow Contamination. *Journal of Spacecraft and Rockets*. Vol. 38, 69-78 (2001)

[13] Richard, W., M. Juergen, et al., Miniature Ion Thruster for Precision Formation Flying. *40th AIAA/ASME/SAE/ASEE Joint Propulsion Conference and Exhibit*. July 11-14, 2004, Fort Lauderdale, FL.

[14] White, P. S., Best, S., Hrbud, I., Hartsfield, R., and Rose, M. RF Plasma Thruster for SmallSat Applications, *35th AIAA Joint Propulsion Conference*. 20-24 June, 1999, Los Angeles, California.

[15] H. Kuninaka, I. Funaki, and K. Toki. Life Test of Microwave Discharge Ion Thrusters for MUSES-C in Engineering Model Phase. *35th Joint Propulsion Conference*. 20-24 June, 1999, Los Angeles, California.

[16] Marcuccio, S., Genovese, A., Andrenucci, M., Experimental Performance of FEEP Microthrusters, *Proceedings of the 3rd International Symposium on Space Propulsion*, Beijing, China, 1997.

[17] Marcuccio, S., Giannelli, S., Andrenucci, M., Attitude and Orbit Control of Small Satellites and Constellations with FEEP Thrusters, *25th International Electric Propulsion Conference*, Cleveland, OH, 1997.

[18] T.E. Markusic and Y.C.F. Thio. Design of a High-energy, Two-stage Pulsed Plasma Thruster. *38th Joint Propulsion Conference*. July 7-10, 2002, Indianapolis, IN.

[19] Huberman, M.N. and Rosen, S.G., Advanced highthrust colloid sources, *J. of Spacecraft*, Vol. 11, no. 7, July 1974, pp. 475-480.

[20] Micci, M. *Micropropulsion for Small Spacecraft*. (AIAA, 2000)

[21] Aleksander Grm, T.-A. G., Tomaž Rodic. Numerical analysis of a miniaturised cold gas thruster for micro- and nano-satellites. *Engineering Computations*. Vol. 28, 184 - 195 (2011)

[22] Zube, D. M. EP – Electric Spacecraft Propulsion. *Redmond, WA, Aerojet General: 31 (unpublished)*. (2006)

[23] De Groot, W. A. *Propulsion options for primary thrust and attitude control of microspacecrafe*. (Springfield, Va. NASA, LRC; NTIS, distributor, 1998)

[24] Goebel, D. M. and I. Katz. *Fundamentals of Electric Propulsion: Ion and Hall Thrusters*. (Wiley, 2008)

[25] Samukawa, S., M. Hori, et al. The 2012 Plasma Roadmap. *Journal of Physics D: Applied Physics* 45(25): 253001 (2012)

[26] Longmier, B., S. Baalrud, et al. Nonambipolar electron source. *Review of Scientific Instruments*. **77**(11): 113504 (2006)

[27] Longmier, B. and H. Noah. Helicon Mode and Xenon Operation with the Nonambipolar Electron Source. *43rd AIAA/ASME/SAE/ASEE Joint Propulsion Conference & Exhibit*. 11 July, 2007, Cincinnati, OH

[28] Longmier, B. and N. Hershkowitz. Improved operation of the nonambipolar electron source. *Review of Scientific Instruments*. 79(9): 093506 (2008)

[29] Diamant, K. D.. Resonant Cavity Hollow Cathode. *41st AIAA/ASME/SAE/ASEE Joint Propulsion Conference & Exhibit*. July, 2005, Tucson, AZ

[30] Diamant, K. D. Plasma Measurements in a Resonant Cavity Hollow Cathode. *42nd AIAA/ASME/SAE/ASEE Joint Propulsion Conference & Exhibit*. July 9-12 2006, Sacramento, California

[31] Diamant, K. D. Resonant Cavity Plasma Electron Source. *Plasma Science, IEEE Transactions on* 37(8): 1558-1562 (2009)

[32] Diamant, K. D. (2009). Microwave Cathode for Air Breathing Electric Propulsion. *31st International Electric Propulsion Conference*. Sept. 2009, Michigan, USA

[33] Hitoshi, K. and N. Kazutaka. Development of 20cm Diameter Microwave Discharge Ion Engine System "m20". *39th AIAA/ASME/SAE/ASEE Joint Propulsion Conference and Exhibit*. July 20-23, 2003, Huntsville, AL.

[34] Hani, K., F. John, et al. Operation of a Microwave Electron Cyclotron Resonance Cathode. *40th AIAA/ASME/SAE/ASEE Joint Propulsion Conference and Exhibit*.

July 11-14, 2004, Fort Lauderdale, FL.

[35] Nishiyama, K., S. Hosoda, et al. Operational Characteristics of a Microwave Discharge neutralizer for the ECR Ion Thruster μ20. *31st International Electric Propulsion Conference*. Sept. 2009, Michigan, USA

[36] Matthew, E. and B. Sven. Design and Testing of a High Power Electron Cyclotron Resonance Neutralizer. *43rd AIAA/ASME/SAE/ASEE Joint Propulsion Conference & Exhibit*. 11 July, 2007, Cincinnati, OH

[37] Weatherford, B. R., J. E. Foster, et al. Electron current extraction from a permanent magnet waveguide plasma cathode. *Review of Scientific Instruments*. Vol 82: 093507 (2011)

[38] Watanabe, H., T. Nakabayashi, et al. Study on Ignition and Electron Emission Characteristics of Inductively Coupled Plasma Cathode. *TRANSACTIONS OF THE JAPAN SOCIETY FOR AERONAUTICAL AND SPACE SCIENCES, AEROSPACE TECHNOLOGY JAPAN*. Vol 10: 37-42 (2012)

[39] Nakabayashi, T. Parametric Study on Shape Dependence of Inductively Coupled Plasma Cathode for Performance Improvement. *32nd International Electric Propulsion Conference*. September 11-15, 2011, Wiesbaden Germany

[40] Godyak, V., Y. Raitses, et al. RF Plasma Cathode-Neutralizer for Space Applications. *30th International Electric Propulsion Conference*. October 29, 2007 , Florence, Italy

Chapter 2: Modeling of a microwave plasma

When a plasma discharge forms in a microwave resonant cavity, the microwave can be reflected or absorbed by the plasma due to the collisions between electrons and heavy particles. The complex and non-linear interaction between the plasma and the wave cannot be described analytically. In the conditions of the electron source we are studying in this thesis, the background gas pressure of the source is around 100 mtorr, i.e. the plasma can be considered as collisional (the charged particle mean free paths are small with respect to the chamber dimensions) and a fluid description of the plasma is sufficient for our purpose. The self-consistent fluid model of the microwave generated plasma used here can be divided in three parts:

Fluid model of charged particle transport. In this part, both charged particles and neutral particles are described. Charged particle transport is described by continuity equations, momentum transport equations in the drift-diffusion form and energy equations. The system is closed by assuming a Maxwellian electron distribution function. The neutral particles are described by a simplified form of Navier-Stokes equation. Electron and ion transport equations are coupled through Poisson's equation (that provides the ambipolar electric field). In this thesis we have been using a two-dimensional (2D) fluid model of the source developed at LAPLACE/GREPHE, but we will also show that a much more simple "global" (0D) model of the discharge can also be extremely useful to provide good estimates of the main plasma properties.

Plasma chemistry model. In this part a simplified model of the plasma chemistry in xenon is considered. The important point is to have a reasonable description of the total ionization rate in the plasma. Under our conditions, the contribution of metastable states of xenon is important and must be taken into account. Collision frequency, rate coefficient, inelastic power loss rate coefficients are calculated assuming a Maxwellian electron distribution function (with a temperature obtained from the fluid model).

Microwave-plasma interaction. The microwave-plasma interaction is described by solving the Maxwell equations self-consistently with the fluid model of the particle transport and plasma chemistry. Maxwell's equation are solved with a Finite Difference Time Domain (FDTD) method. The calculated electromagnetic field, together with the electron current density provides the absorbed energy used as a source term in the electron energy equation. The electromagnetic power is absorbed in a thin layer at the plasma edge. We will see in the next chapter that the plasma properties are actually not very sensitive to the exact space distribution of the

absorbed power and that very similar results can be obtained, for a given total absorbed power, without coupling Maxwell'equations to the plasma equations, and by just assuming a given space profile of the absorbed power. Maxwell's equations are however necessary to optimize the conditions of breakdown in the cavity, as described in the previous chapter.

2.1 Fluid equations for particle transport

2.1.1 Fluid, particle, and hybridmodels

Charged particle transport in gas discharges can be described by fluid, particle, or hybrid methods. In particle methods the transport is described at the kinetic level (i.e. the particle velocity distribution functions are calculated) while in fluid methods particle transport is characterized by macroscopic quantities such as density, mean velocity and mean energy (i.e. successive moment of the particle distributions functions). In hybrid models different types of particles (or different groups of the same type of particles) may be described differently, i.e. at the kinetic or fluid level. Particle models obviously involve intensive computations and must be used only when specific properties of the particle distribution function are expected. Their main advantage is that they do not require any assumption on the particle transport since they are equivalent to solving charged particle Boltzmann equations. Fluid equations, on the other hand do not form a closed set of equations (i.e. contain only part of the information present in the Boltzmann equation) and therefore rely on assumptions on the particle velocity distribution functions. In gas discharge models at high pressure (e.g. atmospheric pressure), the local field approximation is often used, i.e. the local charged particle velocity distribution function is supposed to be the same as under a uniform field identical to the local field (in space and time) in the simulation. Under lower pressure conditions, as in our electron source problem (0.1 torr), a better approach is to assume that the electron distribution function is Maxwellian. This allows to simplify the transport terms in the moment equations, and to calculate and tabulate the collision frequencies as a function of electron temperature (from the supposedly known electron-neutral cross-sections).

2.1.2 Derivation of the fluid equations

Fluid equations are deduced from the Boltzmann equation which characterizes charged particle transport in a weakly ionized gas, one can find more detailed description in the literatures of Liebermann [1] and F. F. Chen [2]:

(2.1)
$$\frac{\partial f}{\partial t} + \mathbf{v} \cdot \nabla f + \frac{\mathbf{F}}{m} \cdot \nabla_{\mathbf{v}} f = \left.\frac{\partial f}{\partial t}\right|_{coll}$$

This equation is a non-local continuity equation in phase space . is the distribution function in the six-dimensional phase space of particle positions and velocities at time t. The Boltzmann equation describes the flow of the particles, due to the different forces. is the gradient operator in velocity space; corresponds to the macroscopic forces including electromagnetic force and gravity forces; is the mass of the particle. The right hand side is the collision term.

The Boltzmann equation is a complicated integrodifferential equation and solving it efficiently in this form is not currently possible. Particle methods offer a relatively simple way of solving the Boltzmann equation but the computation time becomes prohibitive for large volumes in two or three space dimensions. When the particle free path is significantly smaller than the characteristic dimension of the plasma the fluid approach is reasonable. In fluid models we are interested in macroscopic quantities such as particle density , mean velocity , and mean energy , which corresponds to velocity moments of the distribution function :

(2.2)
$$n(\mathbf{r}, t) = \int f(\mathbf{r}, \mathbf{v}, t) d^3 v$$

(2.3)
$$\mathbf{u} = \frac{1}{n} \int \mathbf{v} f(\mathbf{r}, \mathbf{v}, t) d^3 v$$

(2.4)
$$\varepsilon = \frac{m}{2n} \int v^2 f(\mathbf{r}, \mathbf{v}, t) d^3 v$$

By multiplying the Boltzmann equation by , and and and integrating over velocity space respectively, the Boltzmann equation (2.1) can be approximated by three fluid equations

(2.5)
$$\frac{\partial n}{\partial t} + \nabla \cdot (n\mathbf{u}) = S$$

(2.6)
$$\frac{\partial n\mathbf{u}}{\partial t} + \nabla \cdot (n\mathbf{u} \otimes \mathbf{u}) = \frac{\mathbf{G}}{m} = \frac{\mathbf{F}n}{m} - \frac{\nabla \cdot \mathbf{P}}{m} + \frac{\mathbf{C}}{m}$$

(2.7)
$$\frac{\partial en\varepsilon}{\partial t} + \nabla \cdot (en\mathbf{u}\varepsilon + \mathbf{P} \cdot \mathbf{u} + \mathbf{Q}) - qn\mathbf{F} \cdot \mathbf{u} = \Pi$$

These three equations are the well-known continuity equation, momentum equation and energy conservation equations. They describe the space and time evolution of the particle number density , mean particle velocity and mean particle energy The derivation of the fluid equations can be found for example in F. F. Chen's book [2].

The main terms present in these three equations are briefly defined or recalled below.

In the **continuity equation** (2.5), $S = \sum_j N_j n_{1j} n_{2j} K_j$ is the source term and describes the net number of particles created per unit time per unit volume, N_j is the number of particles created in one collision (negative in case of destruction) type j, n_{1j} and n_{2j} are the densities of the colliding particles, and $K_j = \sigma v_r$ is the rate coefficient of the reaction between particle 1 and 2 in units m^3/s, v_r is the relative velocity between particle 1 and 2.

In the **momentum equation** (2.6), $\mathbf{G} = \mathbf{F}n - \nabla \cdot \mathbf{P} + \mathbf{C}$ is the macroscopic force; $\mathbf{F} = q(\mathbf{E} + \mathbf{u} \times \mathbf{B})$ is the macroscopic electromagnetic force, q is elementary charge. $\mathbf{P} = m \int \mathbf{V} \otimes \mathbf{V} f d^3v$ is the pressure stress tensor, $\mathbf{V}$ is the random thermal velocity, which together with mean fluid velocity $\mathbf{u}$ composes the instantaneous particle velocity$\mathbf{v}$, i.e. $\mathbf{v} = \mathbf{u} + \mathbf{V}$. **C** is the collision term of the momentum equation and is generally approximated by $\mathbf{C} = -mn(\mathbf{u} - \mathbf{u}_i)\nu_m$. **C** is the momentum loss of the fluid caused by collisions with another target fluid species$i$, $\mathbf{u}_i$ is the fluid velocity of species i. $\nu_m = \sum_i n_i k_{(m,i)}$ is the mean momentum transfer frequency, where n_i is the target particle density, $k_m = \sigma_m v_r$ is an effective rate coefficient for momentum transfer to target particle i based on the momentum transfer cross section σ_m.

In the **energy equation** (2.7), $\mathbf{Q} = \frac{1}{2} m \int |\mathbf{V}|^2 \mathbf{V} f d^3v$ is the heat flux; Q is the net power density gained/lost in collisions and chemical reactions. P is the pressure tensor. Mean particle energy ε is the particle kinetic energy, including thermal energy and direct energy:

(2.8) $$\varepsilon = \frac{m}{2n} \int \mathbf{v}^2 f d^3v = \frac{1}{2n} m \overline{\mathbf{V}^2} + \frac{1}{2} m \mathbf{u}^2$$

The temperature is related to the thermal energy term, i.e., for electrons:

(2.9) $$T_e = \frac{1}{3k_B} m_e \overline{\mathbf{V}^2}$$

m_e is the electron mass, k_B is Boltzmann constant, T_e is in Kelvin.

2.1.3 Approximations to the fluid equations

Usual approximations for the fluid equations have been considered in this work and are described in this section.

The first approximation is to assume that the pressure tensor is diagonal and isotropic:

(2.10) $$\mathbf{P} = p\mathbf{I} = nk_B T \mathbf{I}$$

where

(2.11) $$p = nk_BT = \frac{1}{3}mn\overline{\mathbf{V}^2}$$

is the scalar pressure, [illegible] is the temperature in Kelvin determined by mean random kinetic energy, and [illegible] is the identity matrix.

The second approximation is related to the collision term of the momentum equation. We only consider collisions between charged and neutral particles and we neglect the mean velocity of the neutral particle [illegible] with respect to the charged particle velocity. The collision term of the momentum equation becomes [illegible]. Thus by substituting equation (2.5) and (2.11) into (2.6), the momentum equation becomes

(2.12) $$\frac{\partial \mathbf{u}}{\partial t} + (\mathbf{u}\cdot\nabla)\mathbf{u} = \frac{q(\mathbf{E}+\mathbf{u}\times\mathbf{B})}{m} - \frac{k_B}{mn}\nabla(nT) - \overline{\nu}_m\mathbf{u}$$

where

(2.13) $$\overline{\nu}_m = \nu_m + \frac{S}{n}$$

is the macroscopic momentum transfer frequency with the inclusion of the creation (ionization) frequency [illegible]. In equation (2.12), on the left-hand side, are the particle acceleration and inertial force terms; on the right-hand side, are electric and magnetic force, pressure gradient and collision terms respectively.

In plasma, in the absence of magnetic field and at low pressure, the momentum equation (2.12) is often further simplified in the case of electrons by neglecting the transport term on the left hand side and the collision term on the right hand side. This gives the well-known Boltzmann relation:

(2.14) $$q\mathbf{E} = \frac{k_B}{n}\nabla(nT)$$

which describes the equilibrium between electrostatic force and pressure gradient.

This is often a good approximation but this representation of the momentum equation does not give any information on the particle flux. Such information can be obtained if the collision term is kept in equation (2.12). This leads to the drift-diffusion form of the momentum equation, which is often a good approximation for electrons and is described below. The drift-diffusion form of the momentum equation provides a simple description of the electron flux and contains the Boltzmann relation in the limit of low collisionality. This approximation is not as good for ions (there is not balance between electrostatic force and pressure gradient for ions since, in contrast to electrons, ions are generally accelerated out of the plasma by the ambipolar field) so we treat separately below the approximations of the fluid equations for electrons and ions.

2.1.4 Electron transport

Here we are considering electron transport in a non-magnetized plasma, and we write the full set of fluid equations based on our assumptions, including: continuity equation, momentum equation and energy equation.

The continuity equation is solved from equation (2.5) directly for electrons:

(2.15) $$\frac{\partial n_e}{\partial t} + \nabla \cdot (n_e \mathbf{u}_e) = S_e$$

Where S_e is the source term, which will be described in section 4.1.

In the momentum equation (2.12) we neglect the inertia term on the left hand side with respect to the pressure gradient term, and the time derivation term with respect to the collision term (this assumes that the collision frequency is larger than the frequency of variations of the velocity) :

(2.16) $$n_e \mathbf{u}_e = \frac{-e}{m_e \overline{\nu}_m} n_e \mathbf{E} - \frac{k_B}{m_e \overline{\nu}_m} \nabla (n_e T_e)$$

Note that in this approach we do not describe the time variations of the mean electron velocity due to the microwave field (otherwise we could not neglect the time derivative term in equation (2.12)); the mean electron velocity we consider in the fluid equations is integrated over a cycle of a microwave field and is sensitive only to the ambipolar field present in equation (2.16).

For collisional electrons and a Maxwellian distribution, the heat flux vector is usually assumed proportional to the temperature gradient as

(2.17) $$\mathbf{Q}_e = -\frac{5 k_B T_e}{2 m_e \overline{\nu}_m} n_e \nabla T_e$$

By neglecting the directed energy with respect to the thermal energy the electron mean energy in (2.8) reduces to the thermal energy (2.9):

(2.18) $$\varepsilon_e = \frac{3}{2} k_B T_e$$

Then the electron energy equation can be simplified from (2.7) as:

(2.19) $$\frac{3 k_B}{2} \frac{\partial n_e T_e}{\partial t} + \nabla \cdot \left(\frac{5 k_B}{2} n_e \mathbf{u}_e T_e + \mathbf{Q}_e \right) = -k_B n_e \mathbf{u}_e \cdot \mathbf{E} + \Pi_e$$

The first term on the right-hand side of this energy equation represents the electron cooling by the ambipolar field E, while the second term is the power absorbed from the microwave field (and should be averaged on a cycle of the microwave field).

2.1.5 Ion transport

In this approach we do not solve an energy equation for ions and we assume that the ion temperature is equal to the temperature of the neutral particles.

The continuity equation for ions is the same as the electron continuity equation:

(2.20) $$\frac{\partial n_i}{\partial t} + \nabla \cdot (n_i \mathbf{u}_i) = S_i$$

As mentioned above, the drift-diffusion representation of the flux is not good for a discharge at relatively low pressure. This is because ions are accelerated out of the plasma by the ambipolar field so that the electric field does not approximately balance the pressure gradient as in the case of electrons, and moreover, inertia effects can be dominant if the ion mean free path becomes large. These effects are described by keeping the inertia terms (see literature [4]) in equation (2.12),which leads to:

(2.21) $$\frac{\partial \mathbf{u_i}}{\partial t} + (\mathbf{u_i} \cdot \nabla)\mathbf{u_i} = \frac{q\mathbf{E}}{m_i} - \frac{k_B}{m_i n_i}\nabla(n_i T_i) - \overline{\nu}_m \mathbf{u_i}$$

$\overline{\nu}_m = \nu_{mi} + \frac{S_i}{n_i}$ is the effective collision frequency, where corresponds to ion-neutral collisions and is deduced from the ion-mobility data [5].

2.1.6 Neutral transport

The transport of neutral particle species n is described by an approximate Navier-Stokes equation:

(2.22) $$m_n \frac{\partial \mathbf{u_n}}{\partial t} + m_n(\mathbf{u_n} \cdot \nabla)\mathbf{u_n} - m_n \eta_n\left(\nabla^2 \mathbf{u}_n + \frac{1}{3}\nabla(\nabla \cdot \mathbf{u}_n)\right) = \mathbf{F}_n - \frac{k_B}{n_n}\nabla(n_n T_n)$$

Where is the viscosity coefficient and is the net drag force due to the collisions with other species .

(2.23) $$\frac{\partial}{\partial t}(c_n n_n k_B T_n) + \nabla \cdot \left((c_n + 1) n_n \mathbf{u}_n k_B T_n - k_B \kappa_n \nabla T_n\right) = \Pi_n$$

Where is the heat capacity at constant volume, is the thermal conductivity, is the net power gained in reactions and collisions with other species. More detailed description of neutral transport approach is reported in literatures of [15].

2.2 Zero-dimensional model

A dimensional model such as the fluid model described above and used in this thesis

can be quite complex to solve because of the strong non-linearities and of the stiff coupling between the different equations. Often, in low pressure plasmas, the electron thermal conductivity is large and the electron temperature can be, to a large extent, considered as a constant (this is no longer true when magnetic fields are present). This can be the case for example in a discharge chamber of dimensions on the order of 10-20 cm, at pressures on the order of 10 mtorr.

When the assumption of constant electron temperature is reasonable, an alternative to the complex dimensional model above can be a zero-dimensional, or global model as is talked in Liebermann's book [1]. Basically, a global model is built on two types of equations for the plasma: a global particle balance equation for the charged particles, and a global power balance equation. When plasma chemistry must be taken into account (i.e. reactions between excited species, dissociation products etc…) particle balance equations for each species must be added.

The global particle balance states that the production of charged particles by ionization in the volume must be exactly balanced by losses to the walls. Since the electron temperature is supposed to be constant, the electron reaction rates (ionization, etc…) are constant so that the global ionization is known if the plasma density distribution is known. At low pressure, the plasma density can be supposed to be constant except near the walls where it must decay as the ion velocity increases to satisfy the Bohm criterion at the sheath entrance. At intermediate pressure (eg 100 mtorr) the assumption of constant density is no longer good and a diffusion profile is better than a constant density. The charged particle losses to the walls is estimated by the Bohm flux. To calculate this flux, it is necessary to calculate the value of the plasma density at the sheath entrance (where the ion velocity is equal to the Bohm velocity). For very low collisionality (low pressure), the ion density at the sheath entrance can be deduced from the plasma density by the factor exp(-1/2) corresponding to the fact that the ions must gain an energy equal to $k_BTe/2$ in the presheath. For high pressure (eg 100 mtorr) , as mentioned above, the particle flux to the walls can be estimated from the diffusion profile of the density. For intermediate pressure some analytical expressions of the plasma density at the sheath entrance have been derived by different authors [2]-[3]. These expressions depend on the chamber dimensions and on the ion mean free path. We will not describe here the derivation of these expressions but we will see in details in chapter 4, the case corresponding to a collisional plasma where the plasma density profile is controlled by ambipolar diffusion (this corresponds the conditions of the electron source we are studying in this thesis: 100 mtorr xenon plasma).

In the global particle balance equation, the charged particle generated by ionization per unit time in the source depends on electron temperature through the ionization rate and is proportional to the electron density, gas density and source volume. The loss of charged particle to the walls per unit time is equal to the Bohm flux integrated over the wall surface. It is therefore proportional to the plasma density (multiplied by a

factor accounting for the plasma decay to the sheath entrance), to the Bohm velocity (which depends on electron temperature), and to the wall surface. It is therefore easy to see that the particle balance equation relates the electron temperature to the gas density and to an effective dimension of the source (ratio of volume to wall surface multiplied by a coefficient that depends on geometry and collisionality). Therefore for a given gas density, the electron temperature is completely determined by the chamber dimensions (and ion mean free path) and does not depend on power.

The power balance equation states that the total power absorbed in the plasma is dissipated by collisions in the volume and lost by charged particle transport to the walls. The power dissipated by collisions in the volume and the power flowing to the walls are proportional to the plasma density. Therefore the plasma density is proportional to the absorbed power (unless for example the gas density is indirectly affected by the power, because of gas heating).

We will see in chapter 4 that a global model although very simple, can provide a very good insight into the physics of a plasma source and give results that are in very good agreement with a more complex 2D model when the electron temperature and gas density can be considered as uniform.

2.3 Plasma chemistry model

Plasma chemistry plays a very important role in applications of low temperature plasmas related to plasma processing because the active species generated by the plasma interact with the surfaces that are processed.

In the case of applications to electron or ion sources, plasma chemistry may also play a very important role (even in a rare gas) because the presence of excited species can completely modify the charged particle balance and power balance equations. When the concentration of metastable states becomes significant, stepwise ionization of the metastable can be a non-negligible and even a dominant source of ionization. We will describe in details in chapter 4 the plasma chemistry that we have used in our 0D and 2D model of a microwave discharge in xenon. In the conditions of the considered electron source (100 mtorr xenon, in a cylindrical R=2 cm, L=10 cm chamber), we will see that the models predicts that ionization due to metastable atoms is three times larger than direct electron impact ionization of xenon. This has clearly some effects on the energy cost to produce an electron-ion pair and therefore to the efficiency of the electron source.

2.4 Microwave-Plasma Interaction

In the presence of electromagnetic fields, the E-field of the wave will drive the electrons to oscillate at the wave frequency (this motion is not described in the fluid

equations which are integrated over a time scale of one or more cycles). This results in an electron current density $\mathbf{J} = n_e q \mathbf{u}$, that interacts with the wave. The velocity u in the electron current density is the instantaneous mean electron velocity (different from the cycle averaged mean velocity of the electron fluid equations). For this instantaneous velocity, the important terms in the momentum equations are not the spatial terms, but are the time derivative term, the force term and the collision term. The instantaneous electron mean velocity is therefore deduced from another approximation of the electron momentum equation (note that, for simplicity, we use the same notation as in the fluid equations above for the electron mean velocity and for the electric field, but **u** here is the instantaneous mean electron velocity, and **E** is the microwave field and not the ambipolar field) :

(2.24)
$$\frac{\partial \mathbf{u}}{\partial t} = \frac{q\mathbf{E}}{m} - \overline{\nu}_m \mathbf{u}$$

This form of the electron momentum equation leads to the well-known Drude model representation of the electron behavior in a microwave field.

The ion current density is much smaller than the electron current density and we therefore neglect its contribution to the conduction current in Maxwell's equations.

In the Maxwell equations, the plasma interacts with the wave only through the electron current density which is proportional to the product of the electron mean velocity from equation (2.24) by the electron density deduced from the fluid equations. In the plasma fluid equations, the microwave interacts with the electrons through the absorbed power term in the electron energy equation, which is equal to the time averaged Joule heating term **E**.**J**.

In our microwave plasma model we follow the time evolution of the plasma fluid equations coupled with Maxwell's equations until steady state is reached. Maxwell's equations are solved together with the velocity equation (2.24) and with the plasma density from the fluid model, using a FDTD method (Finite Difference Time Domain [11]). Since the time constants of the plasma and the EM field are different, the plasma equations and field equations can be solved on different time scales (in any case Maxwell's equations must be solved with a time step that is a fraction of the cycle period while the plasma equations are solved on a time scale equal or larger than a period, and using an absorbed power averaged over one cycle of the microwave field).

Another approach would have been to represent the plasma as a dielectric with complex permittivity and to solve the harmonic form of Maxwell's equations. In section 2.4.1 below we recall the plasma representation as a dielectric (Drude model) that is a consequence of equation (2.24) above. In section 2.4.3 we briefly summarize the form of Maxwell's equations and boundary conditions that are used in our simulations.

With these approach methods, people had been able to study microwave plasma discharge with different gas under different pressure ranges, e.g. microwave breakdown under atmosphere (observed both in nature and experimentally [6][7]) had been numerically studied by J P BOEUF, et al. [8][9], microwave plasma used for chemistry vapor deposition with Hydrogen and Methane under relatively high pressure (7.5-150 Torr) had been numerically studied by Hagelaar, Gicquel et al. [10].

2.4.1 Plasma as a Dielectric

We have chosen to solve numerically the space and time dependent form of Maxwell's using the FDTD algorithm. In this section we just recall the classical harmonic form of Maxwell's equations when the plasma is considered as a medium with complex permittivity.

We write the microwave electric field and electron instantaneous mean velocity as:

(2.25) $$\mathbf{E} = \tilde{\mathbf{E}} exp[i\omega t]$$

and

(2.26) $$\mathbf{u}_e = \tilde{\mathbf{u}}_e exp[i\omega t]$$

Where $\tilde{\mathbf{E}}$ and $\tilde{\mathbf{u}}_e$ are the complex oscillation amplitude oscillation amplitude of the field and electron velocity.

Applying (2.25) and (2.26) to momentum equation (2.24) we obtain:

(2.27) $$i\omega\tilde{\mathbf{u}}_e = -\frac{e}{m_e}\tilde{\mathbf{E}} - \overline{\nu}_m\tilde{\mathbf{u}}_e$$

Then we can deduce the complex amplitude of the electron velocity:

(2.28) $$\tilde{\mathbf{u}}_e = -\frac{e}{m_e(i\omega + \overline{\nu}_m)}\tilde{\mathbf{E}}$$

with the same notations, the electron current density can be written as:

(2.29) $$\tilde{\mathbf{J}}_e = -en_e\tilde{\mathbf{u}}_e = -\frac{e^2 n_e}{m_e(i\omega + \overline{\nu}_m)}\tilde{\mathbf{E}}$$

and Maxwell's equation become:

(2.30) $$\nabla\times\tilde{\mathbf{E}} = -i\omega\mu_0\tilde{\mathbf{H}}$$

(2.31) $$\nabla\times\tilde{\mathbf{H}} = \tilde{\mathbf{J}}_{tot} = i\omega\epsilon_0\tilde{\mathbf{E}} + \tilde{\mathbf{J}}_e$$

Where $\tilde{\mathbf{J}}_{tot}$ is the total current, including displacement current $i\omega\epsilon_0\tilde{\mathbf{E}}$ and electron current $\tilde{\mathbf{J}}_e = -en_e\tilde{\mathbf{u}}_e$. Substituting (2.29) into (2.31), we can obtain the total current in the sinusoidal steady state

(2.32)
$$\tilde{\mathbf{J}}_{tot} = i\omega\epsilon_0 \left[1 - \frac{\omega_{pe}^2}{\omega^2 + \overline{\nu}_m{}^2} - \frac{\omega_{pe}^2}{\omega^2 + \overline{\nu}_m{}^2}\frac{\overline{\nu}_m}{\omega}i\right]\tilde{\mathbf{E}}$$

Where $\omega_{pe} = (e^2 n_e/\epsilon_0 m_e)^{1/2}$ is the plasma frequency. Thus we can introduce an effective plasma dielectric constant

(2.33)
$$\epsilon_p = \epsilon_0\epsilon_r = \epsilon_0\left[1 - \frac{\omega_{pe}^2}{\omega^2 + \overline{\nu}_m{}^2} - \frac{\omega_{pe}^2}{\omega^2 + \overline{\nu}_m{}^2}\frac{\overline{\nu}_m}{\omega}i\right]$$

Where ϵ_r is the relative dielectric constant. When the plasma is collisionless ($\overline{\nu}_m = 0$) or the microwave frequency is much larger than collision frequency ($\omega \gg \overline{\nu}_m$), the plasma dielectric constant becomes

(2.34)
$$\epsilon_p = \epsilon_0\epsilon_r = \epsilon_0\left(1 - \frac{\omega_{pe}^2}{\omega^2}\right)$$

When $\omega_{pe}^2 = \omega^2$, the plasma dielectric constant $\epsilon_p = 0$, the plasma density is called critical (or cutoff) density. For 2.45 GHz and 5.8 GHz microwave, the critical densities are 7.5 10^{16} m^{-3} and 4.2 10^{17} m^{-3} respectively.

The representation above of the plasma by the complex permittivity (2.33) is called the Drude model. It would possible to solve our microwave-plasma problem by representing the plasma as a medium with complex permittivity as defined above and by solving Maxwell's equations in the harmonic regime. Since the plasma density (and therefore permittivity) depends on the absorbed power, it would be necessary to perform iterations between the plasma model and Maxwell's equations. Another way to solve our microwave-plasma coupling is to solve the time evolution of the plasma and coupled electromagnetic field. This approach has been chosen in this thesis. We give below a few information on this method.

2.4.2 Time dependent coupling of EM-field and Plasma

We now use the differential form of Maxwell's equations and assume that the microwave propagates into the plasma from vacuum space:

(2.35)
$$\nabla\times\mathbf{E} = -\mu_0\frac{\partial\mathbf{H}}{\partial t}$$

(2.36)
$$\nabla\times\mathbf{H} = \mathbf{J}_{tot} = \epsilon_0\frac{\partial\mathbf{E}}{\partial t} + \mathbf{J}$$

Where $\mathbf{E}$, $\mathbf{H}$ are the electric field and magnetic field of the microwave; μ_0, ϵ_0 are permeability and permittivity constant of the vacuum respectively; $\mathbf{J}_{tot}$ is the total current, including displacement current $\epsilon_0\frac{\partial\mathbf{E}}{\partial t}$ and electric current density $\mathbf{J}$.

The instantaneous electron current density $\mathbf{J}_e$ can be found by solving electron momentum equation (2.24):

(2.37) $$\mathbf{J}_e = -en_e\mathbf{u}_e$$

Where n_e is the electron density, $\mathbf{u}_e$ is the electron velocity from momentum equation (2.24).

When the microwave wave propagates into a plasma, the electric current density $\mathbf{J}$ in Maxwell Ampere curl equation (2.36), can be rewritten as

(2.38) $$\mathbf{J} = \mathbf{J}_d + \mathbf{J}_e$$

Where $\mathbf{J}_d$ is the driving current density to excite the microwave; $\mathbf{J}_e = -en_e\mathbf{u}_e$ is the electron current density from above. By substituting the electron current density into Maxwell equation, we can couple the microwave to the plasma, and in advance to look at the interaction of the microwave with the plasma; this coupling is the first step to make a full self-consistent model of a microwave discharge. Now the Maxwell equations can be written as

(2.39) $$\nabla\times\mathbf{E} = -\mu_0\frac{\partial\mathbf{H}}{\partial t}$$

(2.40) $$\nabla\times\mathbf{H} = \epsilon_0\frac{\partial\mathbf{E}}{\partial t} + \mathbf{J}_d - en_e\mathbf{u}_e$$

2.4.3 Maxwell equations and boundary conditions

Maxwell's equations in 3D

We now write out the vector components of the curl operator in (2.39) and (2.40) to yield the following six coupled scalar equations equivalent to Maxwell's curl equations in the three-dimensional cylindrical coordinate system (r, φ, x) as *Figure 3.3* shown.

(2.41) $$\frac{\partial H_x}{\partial t} = -\frac{1}{\mu_0}\left[\frac{1}{r}\left(\frac{\partial rE_\varphi}{\partial r} - \frac{\partial E_r}{\partial \varphi}\right)\right]$$

(2.42) $$\frac{\partial H_r}{\partial t} = -\frac{1}{\mu_0}\left[\frac{1}{r}\frac{\partial E_x}{\partial \varphi} - \frac{\partial E_\varphi}{\partial x}\right]$$

(2.43) $$\frac{\partial H_\varphi}{\partial t} = -\frac{1}{\mu_0}\left[\frac{\partial E_r}{\partial x} - \frac{\partial E_x}{\partial r}\right]$$

(2.44) $$\frac{\partial E_x}{\partial t} = \frac{1}{\epsilon_0}\left[\frac{1}{r}\left(\frac{\partial rH_\varphi}{\partial r} - \frac{\partial H_r}{\partial \varphi}\right) + J_{dx} - en_e u_{ex}\right]$$

(2.45) $$\frac{\partial E_r}{\partial t} = \frac{1}{\epsilon_0}\left[\frac{1}{r}\frac{\partial H_x}{\partial \varphi} - \frac{\partial H_\varphi}{\partial x} + J_{dr} - en_e u_{er}\right]$$

(2.46)
$$\frac{\partial E_\varphi}{\partial t} = \frac{1}{\epsilon_0}\left[\frac{\partial H_r}{\partial x} - \frac{\partial H_x}{\partial r} + J_{d\varphi} - en_e u_{e\varphi}\right]$$

The system of six coupled partial differential equations of (2.41) - (2.46) forms the basis of the FDTD numerical algorithm for EM wave interactions with general three-dimensional objects, and it is very informative to consider simplifications to two-dimensional and one-dimensional cases. By themselves, these demonstrate interesting and useful electromagnetic wave phenomena and can yield insight to the analytical and algorithmic features of the general three-dimensional case.

Maxwell's equation in 2D

In the three-dimensional cylindrical coordinate system (, ,) as is shown in *Figure 3.3*, let us assume that neither the electromagnetic field excitation nor the modeled geometry has any variation in the direction. That is, we assume that all partial derivatives of the fields with respect to equal zero (/ = 0), and that the structure being modeled extends to infinity in the -direction with no change in the shape or position of its transverse cross section. Then the full set of Maxwell's curl equations in cylindrical coordinates given by (2.41) - (2.46) reduces to

(2.47)
$$\frac{\partial H_x}{\partial t} = -\frac{1}{\mu_0}\frac{1}{r}\frac{\partial r E_\varphi}{\partial r}$$

(2.48)
$$\frac{\partial H_r}{\partial t} = \frac{1}{\mu_0}\frac{\partial E_\varphi}{\partial x}$$

(2.49)
$$\frac{\partial H_\varphi}{\partial t} = \frac{1}{\mu_0}\left(\frac{\partial E_x}{\partial r} - \frac{\partial E_r}{\partial x}\right)$$

(2.50)
$$\frac{\partial E_x}{\partial t} = \frac{1}{\epsilon_0}\frac{1}{r}\frac{\partial r H_\varphi}{\partial r} + \frac{1}{\epsilon_0}\left(J_{dx} - en_e u_{ex}\right)$$

(2.51)
$$\frac{\partial E_r}{\partial t} = -\frac{1}{\epsilon_0}\frac{\partial H_\varphi}{\partial x} + \frac{1}{\epsilon_0}\left(J_{dr} - en_e u_{er}\right)$$

(2.52)
$$\frac{\partial E_\varphi}{\partial t} = \frac{1}{\epsilon_0}\left(\frac{\partial H_r}{\partial x} - \frac{\partial H_x}{\partial r}\right) + \frac{1}{\epsilon_0}\left(J_{d\varphi} - en_e u_{e\varphi}\right)$$

H polarized

In 2D axisymmetric problems, when the EM wave is linear H-polarized [12] (only , , exist), it is possible to simplify the equations (2.41) - (2.46) into:

(2.53)
$$\frac{\partial H_\varphi}{\partial t} = \frac{1}{\mu_0}\left(\frac{\partial E_x}{\partial r} - \frac{\partial E_r}{\partial x}\right)$$

(2.54)
$$\frac{\partial E_x}{\partial t} = \frac{1}{\epsilon_0}\frac{1}{r}\frac{\partial r H_\varphi}{\partial r} + \frac{1}{\epsilon_0}\left(J_{dx} - en_e u_{ex}\right)$$

(2.55)
$$\frac{\partial E_r}{\partial t} = -\frac{1}{\epsilon_0}\frac{\partial H_\varphi}{\partial x} + \frac{1}{\epsilon_0}\left(J_{dr} - en_e u_{er}\right)$$

E polarized

In a similar way, in 2D axisymmetric problems, the equations for a linear E-polarized (only [illegible], [illegible], [illegible] exist) EM wave can be sorted out from (2.41) - (2.46)

(2.56)
$$\frac{\partial H_x}{\partial t} = -\frac{1}{\mu_0}\frac{1}{r}\frac{\partial r E_\varphi}{\partial r}$$

(2.57)
$$\frac{\partial H_r}{\partial t} = \frac{1}{\mu_0}\frac{\partial E_\varphi}{\partial x}$$

(2.58)
$$\frac{\partial E_\varphi}{\partial t} = \frac{1}{\epsilon_0}\left(\frac{\partial H_r}{\partial x} - \frac{\partial H_x}{\partial r}\right) + \frac{1}{\epsilon_0}\left(J_{d\varphi} - e n_e u_{e\varphi}\right)$$

We observe that the H-polarized and E-polarized modes are decoupled; they contain no common field vector components. In fact, these modes are completely independent for structures composed of isotropic materials or anisotropic materials having no off-diagonal components in the constitutive tensors. That is, the modes constitute the two possible ways that two-dimensional electromagnetic field interaction problems can be set up.

Boundary conditions

1. Absorbing boundary condition

For the boundaries where the EM wave goes out of the calculation domain, an Absorbing Boundary Condition (ABC's) should be set to truncate the boundless computation domain, such as Mur's traditional ABC's [12] of one-way approximation, perfectly matched layer (PML) [13], etc. One has to pay special attention to Mur's ABC's that an accurate solution is available only when the boundary is put sufficient far away from the excitation source and the scatter.

2. Metallic boundary

For the EM wave on the metal surfaces, here we give the general definition of the boundary conditions, this boundary condition will be discussed again in chapter 3:

(2.59)
$$E_{//} = 0 \qquad H_\perp = 0$$

2.4.4 FDTD method

The Finite Difference Time Domain (FDTD) method of Kane Yee [11], is one of the available electrodynamics modeling techniques and has been used in this thesis. With FDTD one can solve the time dependent form of Maxwell equations for EM wave propagation in a wide frequency range, arbitrary domain, and treat complex material properties in a natural way.

2.5 Limitations of the model

1. As in any fluid model, the assumption of a given shape of the charged particle distribution function restricts the validity domain of the model. In our model described above, the electron energy distribution function is supposed to be Maxwellian. This is a good approximation especially in our conditions of high plasma density where Coulomb collisions tend to "Maxwellianize" the distribution function but it is difficult to estimate the limits of this assumption.
2. Numerically the solutions of Maxwell's equations in a cavity can be tricky because the resonance are very sharp and small. The calculation of the Q factor for example implies a very small mesh size and the resonant frequency may shift if the mesh size is not small enough. Moreover, the FDTD method is probably not the best method to study a microwave cavity because of the numerical errors induced by the multiple reflections on the walls.
3. In the coupling of Maxwell's equations with the plasma equations, especially in case where the plasma density is over-critical, the skin depth can be very small with respect to the plasma dimensions and this makes difficult to solve describe accurately this coupling.

2.6References

[1] Lieberman, M. A. and A. J. Lichtenberg. *Principles of Plasma Discharges and Materials Processing*. (Wiley, 2005).

[2] Chen, F. F. *Introduction to Plasma Physics and Controlled Fusion*. (Springer, 1984).

[3] Chabert, P. *Physics of Radio-Frequency Plasmas*. (Cambridge University Press, 2011).

[4] Hagelaar, G. J. M. Effective-Viscosity Approach for Nonlocal Electron Kinetics in Inductively Coupled Plasmas. *Physical Review Letters*. 100(2): 025001 (2008)

[5] L.A. Viehland and E.A. Mason. Transport Properties of Gaseous ions over a wide energy range, IV*. *Atomic Data and Nuclear Data Tables*. 60, 37 (1995)

[6] MacDonald, A. D. *Microwave Breakdown in Gases*. (John Wiley & Sons, New York, 1966).

[7] Gould, L. and L. W. Roberts. Breakdown of Air at Microwave Frequencies. *Journal of Applied Physics*. **27**(10): 1162-1170 (1956)

[8] Chaudhury, B., J.-P. Boeuf, et al. Physics and modelling of microwave streamers at atmospheric pressure. *Journal of Applied Physics*. 110(11): 113306 (2011)

[9] Chaudhury, B., J.-P. Boeuf, et al. Pattern formation and propagation during microwave breakdown. *Physics of Plasmas*. 17(12): 123505 (2010)

[10] Hagelaar, G. J. M., K. Hassouni, et al. Interaction between the electromagnetic fields and the plasma in a microwave plasma reactor. *Journal of Applied Physics*. 96(4): 1819-1828 (2004)

[11] Yee, C. L. Numerical solution of initial boundary value problems involving maxwell's equations in isotropic media. *Antennas and Propagation. IEEE Transactions on*. 14(3): 302-307 (1966)

[12] Mur, G. Absorbing Boundary Conditions for the Finite-Difference Approximation of the Time-Domain Electromagnetic-Field Equations. *Electromagnetic Compatibility, IEEE Transactions on EMC*. 23(4): 377-382 (1981)

[13] Berenger, J. P. A perfectly matched layer for the absorption of electromagnetic waves. *J. Comput. Phys*. 114(2): 185-200 (1994)

[14] Hagelaar, G. J. M. *Modeling methods for low temperature plasmas*. (Habilitation à Diriger des Recherches, Université de Toulouse, France, 2008).

[15] Hagelaar, G. J. M., G. Fubiani, et al. Model of an inductively coupled negative ion source: I. General model description. *Plasma Sources Science and Technology*. 20(1): 015001 (2011)

[16] Boeuf, J. P., B. Chaudhury, et al. Theory and Modeling of Self-Organization and Propagation of Filamentary Plasma Arrays in Microwave Breakdown at Atmospheric Pressure. *Physical Review Letters*. 104(1): 015002 (2010)

Chapter 3: Electromagnetic field in a microwave resonant cavity

The aim of this thesis is to study the possibility to design efficient plasma electron sources as an alternative to the usual thermoionic hollow cathodes. Thermoionic hollow cathodes are very efficient because the required power per extracted electron is quite low. The reasons for the efficiency of these cathodes are the high electron emissivity of the cathode materials and the fact that they can be sustained by a very low voltage (i.e. the ion energy losses in the cathode sheath are low). One important constraint when designing an efficient electron source is therefore to try to minimize the voltage drop between the plasma and the cathode. This can be achieved for example in ICP (inductively coupled plasmas) or microwave plasmas, if the electron temperature is small enough. In this work we have chosen to study a microwave source in a design proposed by Diamant [1][2][3]. In this design, the plasma is formed in a metallic cavity and the microwave power is introduced in the cavity through a quartz window. Besides the electron extraction efficiency, another important issue is the question of gas breakdown in the cavity and of the optimization of the cavity geometry to initiate breakdown at reasonable values of the incident electric field.

In this chapter, we describe the parameters controlling the electromagnetic field distribution in the cavity prior to plasma formation and study the conditions of resonance that are sought for to optimize gas breakdown. We then describe the ignition phase of the discharge and the plasma formation, and discuss the best operating conditions (gas pressure) for breakdown.

3.1Introduction

Microwaves are electromagnetic waves with wavelengths typically in the range from 1 millimeter to 1 meter (eg frequency between 300 GHz and 0.3 GHz). In a so-called TEM wave, the electric field and magnetic field are perpendicular to each other and oscillate in a plane perpendicular to the direction of propagation defined by the wave vector.

Microwave propagation can be perfectly described by Maxwell equations, and microwave's energy density, energy flux density (known as Poynting vector), energy conservation will be described in section 3.2.

In experiments and industry, microwave can be generated by a magnetron or the new up-to-date solid state source, guided by waveguides (coaxial waveguide, rectangular waveguide, cylindrical waveguide, etc.), and coupled with a metallic cavity. When the

microwave is coupled into a metallic cavity, if a microwave resonance occurs, the cavity would be called a microwave resonant cavity.

When the microwave propagates into the resonant cavity, there are two resonance mode types, TE_{mnp} (Transverse Electric)and TM_{mnp} (Transverse Magnetic), depending on whether the electric or magnetic field is orthogonal to the cavity axis. The m,n,p indices represent the number of electric field maxima (or lobes) in the angular, radial and axial directions respectively. For TE mode, since the electric field is orthogonal to the cavity axis, and parallel to the cavity side wall, due to the electric boundary condition, the tangential component of the electric field should be zero on the side wall surface. Examples of TM and TE modes are displayed in Fig. 1 (TE_{112} , and TM_{012}). The TM modes have maxima on the basis of the cylinder forming the cavity. In this these thesis we have chosen (following Diamant, [1]) to use the TM_{011} mode which has two electric field maxima, one on the quartz surface, and one on the metallic surface More details about describing the perfect (or ideal) cavity for a TM_{011} mode are given in section 3.2.2 and 3.2.3.

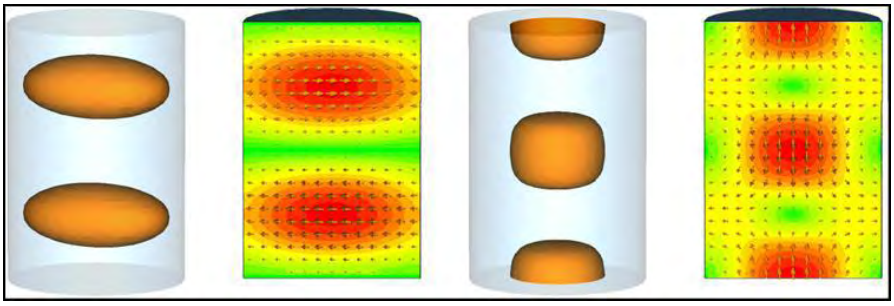

Figure 3.1: Example showing the electric field distribution of TE_{112} (left two) and TM_{012} (right two) modes in a cylindrical cavity. Silva et al. 2009 [4].

Real microwave cavities need excitation sources to excite microwave in the cavity. The presence of the excitation source and the microwave injection makes the description of the electromagnetic field in the cavity a little more complicated, hence we will use numerical tools to calculate the field distribution. The numerical tool (HFSS) used for these calculations and the excitation technique will be introduced in section 3.3.1 and 3.3.2.

When a microwave cavity is empty, we call it a homogeneous cavity; otherwise, the cavity is called a non-homogeneous cavity. This is the case in our geometry since the cavity is partially filled with a dielectric. The study of the cylindrical cavity with a quartz plate that separates the plasma volume from the microwave injection are presented in section 3.3.3.

The microwave energy may be many times enlarged by a microwave resonant cavity, due to the standing wave effect. The factor to investigate the energy enhancement level is called a Q factor (Quality factor). The basic definition of the Q factor and the

calculation and measurement methods of this parameter are described in section 3.3.4.

Briefly, throughout this chapter, our aim is to design some non-homogeneous (mentioned above) microwave resonant cavities, which works in TM_{mnl} mode at certain microwave frequencies in absence of plasma. In the case of a perfect resonant cavity, analytical solutions of this problem can be obtained and are based on the calculations of the eigenvalues of the field equations. In a real case, one has to take into account the presence of an antenna which couples the microwave energy to the cavity, and, in our case, of a dielectric plate that separates the plasma volume form the microwave injection. The analytical solutions are therefore no longer valid and numerical tools can be used to estimate the effects of the perturbations induced by the antenna and the quartz plate. The analytical theory for the ideal case is presented in section 3.2 while the real situation is discussed in section 3.3, on the basis of simulations performed with the commercial software HFFS, compared with results from a FDTD (Finite Difference Time Domain) model developed during the course of this thesis.

3.2 EM wave in a perfect cavity

A perfect cavity here means that the cavity is assumed to be a standard rectangular or cylindrical one without any other excitation antenna or wave guide connection. The walls of the cavity are supposed to be perfect conductor rather than a lossy conductor, and the material inside the cavity is vacuum. With the above assumptions we can apply the classical theory to this resonant cavity problem.

Maxwell's equations in free space

The theoretical description of the microwave field in this part can be found in many textbooks [5][6][10]. In the following we consider time-harmonic fields and we write the electric and magnetic fields as:

(3.1) $$\mathbf{E}(\mathbf{r},t)e^{i\omega t} \; and \; \mathbf{H}(\mathbf{r},t)e^{i\omega t}$$

where $\omega=2\pi f$ is the angular frequency and E and H are the complex amplitude of the fields (which include the phases shift with respect to the incident wave).

Maxwell's equation can be written as:

(3.2) $$\nabla\times\mathbf{E} = -i\omega\mu\mathbf{H}$$

(3.3) $$\nabla\times\mathbf{H} = \mathbf{J}_{tot} = i\omega\epsilon\mathbf{E} + \mathbf{J}$$

(3.4) $$\nabla\cdot\mathbf{E} = \frac{\rho}{\epsilon}$$

(3.5) $$\nabla\cdot\mathbf{H} = 0$$

(3.2) is the Maxwell-faraday equation and (3.3) is the Maxwell-Amp ère equation.

, are respectively the permeability and permittivity constant of the medium, is the space charge; is the total current, including displacement current and electric current density .

Energy conservation

Starting from Maxwell-Ampere equation (3.3), and taking the scalar product of the equation with E on both sides of the Ampere equation, we get:

(3.6) $$\mathbf{E}\cdot\mathbf{J} = \mathbf{E}\cdot(\nabla\times\mathbf{H}) - i\epsilon\omega\mathbf{E}^2$$

Then combined with $\mathbf{E}\cdot(\nabla\times\mathbf{H}) = \mathbf{H}\cdot(\nabla\times\mathbf{E}) - \nabla\cdot(\mathbf{E}\times\mathbf{H})$, and equation (3.4), equation (3.6) can be written as:

(3.7) $$\mathbf{E}\cdot\mathbf{J} = -\nabla\cdot(\mathbf{E}\times\mathbf{H}) - i\omega(\mu\mathbf{H}^2 + \epsilon\mathbf{E}^2)$$

Defining the quantities S and by:

(3.8) $$\vec{\mathbf{S}} = \mathbf{E}\times\mathbf{H}\ (\mathrm{J}\cdot\mathrm{m}^{-2}\cdot\mathrm{s}^{-1})$$

(3.9) $$\varepsilon = \frac{1}{2}(\epsilon\mathbf{E}^2 + \mu\mathbf{H}^2)$$

and using equations (3.2) and (3.3), equation (3.7) can be rewritten as:

(3.10) $$\mathbf{E}\cdot\mathbf{J} = -\nabla\cdot(\vec{\mathbf{S}}) - \frac{\partial\varepsilon}{\partial t}$$

This is the energy conservation equation (or energy continuity equation). The left hand side is the energy source term to supply or consume energy, the first term of the right hand side is the divergence of the energy flux density (S is called the Poynting vector), and the second term is the time differential of energy density

We will use this equation in section 3.3.4 to describe the energy stored inside of the cavity.

Energy density

For a source-free electromagnetic wave, the time averaged energy density ε_{av} can be written as :

(3.11)
$$\varepsilon_{av} = \frac{1}{2}(\frac{1}{2}\epsilon \mathbf{E}_{amp}^2 + \frac{1}{2}\mu \mathbf{H}_{amp}^2) = \frac{1}{2}\epsilon \mathbf{E}_{amp}^2 = \frac{1}{2}\mu \mathbf{H}_{amp}^2$$

where $\mathbf{E}_{amp}$, $\mathbf{H}_{amp}$ are the amplitude of the electric field and magnetic field respectively. In any space, the microwave energy can be calculated by the volume integration of the time averaged energy density.

3.2.1 Vector potential and Helmholtz equation

So far, we have the field equations for describing the propagation of the microwave in free space. To solve the field equations, a general method to obtain the solutions of the equations, is by introducing a *magnetic vector potential* and an *electric vector potential* [5].

Vector potential, wave equation and wave potential

In a homogeneous source-free region, the field equations (3.2)-(3.5) become:

(3.12)
$$\nabla \times \mathbf{E} = -i\omega\mu \mathbf{H}$$

(3.13)
$$\nabla \times \mathbf{H} = i\omega\epsilon \mathbf{E}$$

(3.14)
$$\nabla \cdot \mathbf{E} = 0$$

(3.15)
$$\nabla \cdot \mathbf{H} = 0$$

Considering equation (3.14) and (3.15), the divergence less vector $\mathbf{E}$ and $\mathbf{H}$ can be the curl of some other vectors; so:

(3.16)
$$\mathbf{E} = -\nabla \times \mathbf{F}$$

(3.17)
$$\mathbf{H} = \nabla \times \mathbf{A}$$

Where $\mathbf{F}$ is called an *electric vector potential*, $\mathbf{A}$ is called a *magnetic vector potential*. Substituting equations (3.17) into equations (3.12), and (3.16) into (3.13) respectively, we have

(3.18)
$$\nabla \times (\mathbf{E} + i\omega\mu \mathbf{A}) = 0$$

(3.19)
$$\nabla \times (\mathbf{H} + i\omega\epsilon \mathbf{F}) = 0$$

Any curl-free vector is the gradient of some scalar. Hence,

(3.20)
$$\mathbf{E} + i\omega\mu \mathbf{A} = -\nabla \Phi^a$$

(3.21) $$\mathbf{H} + i\omega\epsilon\mathbf{F} = -\nabla\Phi^f$$

where [illegible] and [illegible] are electric scalar potentials related to [illegible] and [illegible] respectively. To obtain the equation for [illegible] and [illegible], substitute equations (3.20) and (3.17) into equation (3.13), equations (3.21) and (3.16) into equation (3.12), will give

(3.22) $$\nabla\times\nabla\times\mathbf{A} - k^2\mathbf{A} = -i\omega\epsilon\nabla\Phi^a$$

(3.23) $$\nabla\times\nabla\times\mathbf{F} - k^2\mathbf{F} = -i\omega\mu\nabla\Phi^f$$

Where [illegible]. Equations (3.22) and (3.23) can be transformed into:

(3.24) $$\nabla(\nabla\cdot\mathbf{A}) - \nabla^2\mathbf{A} - k^2\mathbf{A} = -i\omega\epsilon\nabla\Phi^a$$

(3.25) $$\nabla(\nabla\cdot\mathbf{F}) - \nabla^2\mathbf{F} - k^2\mathbf{F} = -i\omega\mu\nabla\Phi^f$$

we are still free to choose [illegible] and [illegible]. If we let

(3.26) $$\nabla\cdot\mathbf{A} = -i\omega\epsilon\Phi^a$$

(3.27) $$\nabla\cdot\mathbf{F} = -i\omega\mu\Phi^f$$

the equations (3.24) and (3.25) simplifies to

(3.28) $$\nabla^2\mathbf{A} + k^2\mathbf{A} = 0$$

(3.29) $$\nabla^2\mathbf{F} + k^2\mathbf{F} = 0$$

These are the Helmholtz equations, or complex wave equations. Solutions to equations (3.28) and (3.29) are called wave potentials. Note that the components of the wave potentials from equations (3.28) and (3.29) satisfy the scalar wave equation, or Helmholtz equation,

(3.30) $$\nabla^2\mathbf{U} + k^2\mathbf{U} = 0$$

- **TM field**

In terms of the magnetic wave potential, with (3.13), (3.17) and (3.28) the electromagnetic field components given by

(3.31) $$\mathbf{E} = -i\omega\mu\mathbf{A} + \frac{1}{i\omega\epsilon}\nabla(\nabla\cdot\mathbf{A})$$

(3.32) $$\mathbf{H} = \nabla\times\mathbf{A}$$

- **TE field**

In terms of the electric wave potential, with (3.12), (3.16) and (3.29) the electromagnetic field components given by

(3.33) $$\mathbf{E} = -\nabla\times\mathbf{F}$$

(3.34)
$$\mathbf{H} = -i\omega\epsilon\mathbf{F} + \frac{1}{i\omega\mu}\nabla(\nabla\cdot\mathbf{F})$$

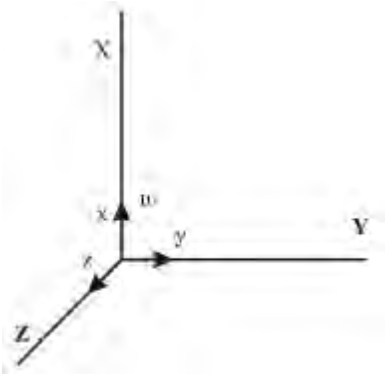

Figure 3.2: Rectangular coordinates system.

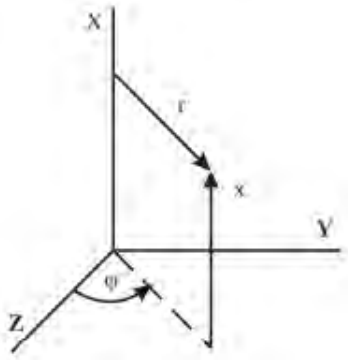

Figure 3.3: Cylindrical coordinates system.

Helmholtz equation in cylindrical coordinates

The electromagnetic field propagates in free space in cylindrical coordinates are already given above with equations (3.31)(3.32) or equations (3.33)(3.34). Problems of solution in standing waves or with boundaries which coincide with cylindrical coordinate surfaces are considered here and the following sections, the cylindrical coordinates system and geometry are shown in *Figure 3.3*. We first consider solutions to the scalar Helmholtz equation (3.30). Once we have these scalar wave functions, we can construct electromagnetic fields according to equations (3.31)(3.32) or equations (3.33)(3.34).

The scalar Helmholtz equation in cylindrical coordinates is

(3.35)
$$\frac{1}{r}\frac{\partial}{\partial r}(r\frac{\partial \mathbf{U}}{\partial r}) + \frac{1}{r^2}\frac{\partial^2 \mathbf{U}}{\partial \varphi^2} + \frac{\partial^2 \mathbf{U}}{\partial x^2} + k^2\mathbf{U} = 0$$

The only solution can be found by following the method of separation of variables. With this method we seek to find solutions in the form of

(3.36)
$$\mathbf{U}(x, r, \varphi) = \mathbf{X}(x)\mathbf{R}(r)\mathbf{\Phi}(\varphi)$$

where [illegible] are positions in axial, radial and angular direction respectively, the equation (3.35) can be separated as follow:

(3.37)
$$\frac{d^2\mathbf{X}(x)}{dx^2} + k_x^2\mathbf{X}(x) = 0$$

(3.38)
$$\frac{d^2\mathbf{\Phi}(\varphi)}{d\varphi^2} + m^2\mathbf{\Phi}(\varphi) = 0$$

(3.39)
$$r\frac{d}{r}(r\frac{d\mathbf{R}(r)}{dr}) + (k_T^2 r^2 - m^2)\mathbf{R}(r) = 0$$

(3.40) $$k_x^2 + k_T^2 = k^2$$

Where T represents the transverse components (r and φ), k_x and m represent the wave number in axial and angular direction respectively, k_T means the transverse wave numbers.

According to equation (3.40), one can obtain:

(3.41) $$f = \frac{1}{2\pi\sqrt{\epsilon\mu}}k = \frac{1}{2\pi\sqrt{\varepsilon\mu}}\sqrt{k_x^2 + k_T^2}$$

Where f is the frequency that one can obtain from wave number.

Standing wave solution for Helmholtz equation in cylindrical coordinates

Equations (3.37)(3.38) are standing wave equations, giving rise to harmonic functions. These we denote, in general, by $S(k_x x), S(m\varphi)$. Equation (3.39) is *Bessel's equation* of order m, solutions noted $B_m(k_T r)$. Commonly used solutions to Bessel's equation are

(3.42) $$B_m(k_T r) \sim J_m(k_T r), N_m(k_T r), H_m^{(1)}(k_T r), H_m^{(2)}(k_T r)$$

Where $J_m(k_T r)$ is the Bessel function of the first kind, $N_m(k_T r)$ is the Bessel function of the second kind, $H_m^{(1)}(k_T r)$ is the Hankel function of the first kind, and $H_m^{(2)}(k_T r)$ is the Hankel function of the second kind. Any two of the functions of equation (3.42) are linearly independent solutions; so $B_m(k_T r)$ is, in general, a linear combination of any two of them. According to equation (3.36), we can obtain solutions to the Helmholtz equation as

(3.43) $$\mathbf{U}(x, r, \varphi) = S(k_x x)S(m\varphi)B_m(k_T r)$$

Now, consider the various solutions to Bessel's equation. We **note** that only the $J_m(k_T r)$ functions are nonsingular at $r = 0$. **Hence, if a field is to be finite at** $r = 0$, **the** $B_m(k_T r)$ **must be** $J_m(k_T r)$, and solutions (3.43) could be of the form

(3.44) $$\mathbf{U}(x, r, \varphi) = S(k_x x)S(m\varphi)J_m(k_T r), \ r = 0 \ included$$

With $J_m(k_T r)$, the solution can be used for the position r=0. The solution of the harmonic functions $S(k_x x)$ and $S(m\varphi)$ are

(3.45) $$S(k_x x) = A\cos(k_x x) + B\sin(k_x x)$$

(3.46) $$S(m\varphi) = C\cos(m\varphi) + D\sin(m\varphi)$$

Then in the longitudinal direction, angular direction, apply solutions (3.45)(3.46) to

(3.44), the standing wave solution of is:

(3.47) $$\mathbf{U}(x,\varphi,r) = [\cos(k_x x) + \sin(k_x x)][\cos(m\varphi) + \sin(m\varphi)] \cdot [J_m(k_T r)]$$

is Bessel functions with integer order. In a cylindrical resonant cavity, the field in angular direction is in standing wave, and the field must be continuous around the whole circle. Therefore m=0, 1, 2, ... : an integer is necessary. There is no boundary around the whole circle, so in equation (3.47), either or can be chosen; so we have a mode degeneracy except for the cases , hence:

(3.48) $$\mathbf{U}(x,\varphi,r) = [\cos(k_x x) + \sin(k_x x)] \left\{ \begin{array}{c} \cos(m\varphi) \\ \sin(m\varphi) \end{array} \right\} J_m(k_T r)$$

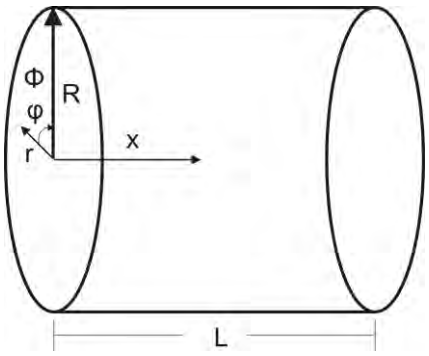

Figure 3.4: Resonant cavity and Cylindrical coordinates.

Now we have the general standing wave solution for wave potential . To determine the electromagnetic field, m=0, 1, 2, ...is known, we still have to specify the wave numbers , with boundary conditions, which will be discussed in following section 3.2.3.

The general solution of EM fields in standing waves

In the section above, we obtained the general solution for wave potential in standing waves, here we are going to derive the fields from the wave potential firstly.

Let's go back to equations (3.31)(3.32) and (3.33)(3.34), and obtain electromagnetic field components from them.

If we take

(3.49) $$\mathbf{A} = \mathbf{u}_x U$$

Where is the unit vector in x direction, has already been solved in cylindrical coordinates in above two sections, which is given out in equation (3.48), equations (3.31) and (3.32) can be expanded in cylindrical coordinates as

$$\mathbf{E}_r = \frac{1}{i\omega\epsilon}\frac{\partial^2\mathbf{U}}{\partial r\partial x}, \quad \mathbf{H}_r = \frac{1}{r}\frac{\partial\mathbf{U}}{\partial\varphi}$$

$$\mathbf{E}_\varphi = \frac{1}{i\omega\epsilon r}\frac{\partial^2\mathbf{U}}{\partial\varphi\partial x}, \quad \mathbf{H}_\varphi = -\frac{\partial\mathbf{U}}{\partial r} \tag{3.50}$$

$$\mathbf{E}_x = \frac{1}{i\omega\epsilon}(\frac{\partial^2}{\partial x^2} + k^2)\mathbf{U}, \quad \mathbf{H}_x = 0$$

the cylindrical coordinates system is shown in *Figure 3.3*. A field with no [illegible] is called [illegible] (TM).

If we take

$$[illegible] \tag{3.51}$$

Where [illegible] is the unit vector in x direction, [illegible] has already been solved in cylindrical coordinates in above two sections, which is given out in equation (3.48), equations (3.33) and (3.34) can be expanded in cylindrical coordinates as

$$\mathbf{E}_r = -\frac{1}{r}\frac{\partial\mathbf{U}}{\partial\varphi}, \quad \mathbf{H}_r = \frac{1}{i\omega\mu}\frac{\partial^2\mathbf{U}}{\partial r\partial x}$$

$$\mathbf{E}_\varphi = \frac{\partial\mathbf{U}}{\partial r}, \quad \mathbf{H}_\varphi = \frac{1}{i\omega\mu r}\frac{\partial^2\mathbf{U}}{\partial\varphi\partial x} \tag{3.52}$$

$$\mathbf{E}_x = 0, \quad \mathbf{H}_x = \frac{1}{i\omega\mu}(\frac{\partial^2}{\partial x^2} + k^2)\mathbf{U}$$

the cylindrical coordinates system is shown in *Figure 3.3*. A field with no [illegible] is called [illegible] (TE).

Now we have the general solution for EM fields in standing waves. The specific values of these fields need the specific solution of wave potential [illegible], which is decided by the boundary conditions as described in the following section.

3.2.2 Metallic boundaries and solutions for TM/TE modes

When the microwave propagates in a cylindrical cavity with metal boundary as shown in *Figure 3.4*, R and L are the radius and length of the cylinder respectively, we can take the boundary conditions to solve [illegible], and [illegible] in equation (3.48) and in advance determine the electromagnetic field for TM and TE modes by applying equation (3.48) to above equations (3.50) and (3.52), here we just show how to obtain field in TM modes, the field for TE modes can be obtained in a similar way.

The boundary conditions on the cavity metal walls impose zero tangential

components for the electric field and zero normal components for magnetic field, according to Figure 3.4, which gives

$$\mathbf{E}_r|_{x=0,L} = 0, \quad \mathbf{H}_r|_{r=R} = 0$$

(3.53)

$$\mathbf{E}_x|_{r=R} = 0, \quad \mathbf{H}_x|_{x=0,L} = 0$$

$$\mathbf{E}_\varphi|_{x=0,L} = 0$$

After applying equation (3.48) and boundary conditions (3.53) into TM field equations (3.50), one can find that in equation (3.48), the item $\sin(k_x x)$ has to be dropped, becomes

(3.54)

$$\mathbf{U}(x,\varphi,r) = \cos(k_x x)\left\{\begin{array}{c}\cos(m\varphi)\\ \sin(m\varphi)\end{array}\right\} J_m(k_T r)$$

and the conditions

(3.55)

$$k_x = \frac{p\pi}{L} \quad k_T = \frac{\nu_{mn}}{R}$$

must be satisfied, where p is integer, L is the length of the cavity; ν_{mn} denotes the n^{th} root of the Bessel function of the m^{th} order (J_m), R is the radius of the cavity.

Then substituting k_x, k_T in to (3.54), can have the TM_{mnp} mode potential function:

(3.56)

$$\mathbf{U}^{TM}_{mnp} = \cos(\frac{p\pi}{L}x)\left\{\begin{array}{c}\cos(m\varphi)\\ \sin(m\varphi)\end{array}\right\} J_m(\frac{\nu_{mn}}{R}r)$$

where m=0, 1, 2, ...; n=1, 2, 3, ...; and p=1, 2, 3, ...

Substituting (3.56) into equations (3.50), the electromagnetic field for TM mode are:

(3.57)

$$\mathbf{E}_x(x,\varphi,r) = A_1\cos(\frac{p\pi}{L}x)\left\{\begin{array}{c}\cos(m\varphi)\\ \sin(m\varphi)\end{array}\right\} J_m(\frac{\nu_{mn}}{R}r)$$

(3.58)

$$\mathbf{E}_r(x,\varphi,r) = A_2\sin(\frac{p\pi}{L}x)\left\{\begin{array}{c}\cos(m\varphi)\\ \sin(m\varphi)\end{array}\right\} J'_m(\frac{\nu_{mn}}{R}r)$$

(3.59)

$$\mathbf{E}_\varphi(x,\varphi,r) = A_3\sin(\frac{p\pi}{L}x)\left\{\begin{array}{c}\sin(m\varphi)\\ \cos(m\varphi)\end{array}\right\} J_m(\frac{\nu_{mn}}{R}r)$$

where in equation (3.58), J'_m is the derivative of the Bessel function of the m^{th} order, when $r = R$,

$$J'_m(\frac{\nu_{mn}}{R}r) = constant$$

$A_1 = \frac{1}{i\omega\varepsilon}(\frac{\nu_{mn}}{R})^2$, $A_2 = \frac{1}{i\omega\varepsilon}\frac{\nu_{mn}}{R}\frac{p\pi}{L}$, $A_3 = \frac{m}{i\omega\varepsilon}\frac{p\pi}{L}$ are the constants that depend on the cavity geometry R and L substituting (3.55) to equation (3.41), the resonant frequency of TM_{mnp} mode for a resonant cavity is:

(3.60) $$f_r|_{TM_{mnp}} = \frac{1}{2\pi\sqrt{\epsilon\mu}}\sqrt{(\frac{\nu_{mn}}{R})^2 + (\frac{p\pi}{L})^2}$$

the resonant frequency of a cavity at TM_{mnp} mode is $f_r|_{TM_{mnp}}$, which is decided by the right side of the equation (3.40). μ, ϵ are permeability and permittivity constant of the medium in the cavity respectively; m, n, p are integers; ν_{mn} denotes the n^{th} root of the Bessel function of the m^{th} order (J_m), R is the radius of the cavity; L is the length of the cavity. The indexes m, n, p indicate the electric field structure, which represent the number of electric field maxima (or lobes) in the angular, radial and axial directions respectively.

So far, we finally get the equation to describe and solve a perfect resonant cavity: if the incident frequency is fixed, we can get the dimension (R, L) of the cavity for resonance; if the dimension of a cavity is given, we can get the corresponding incident microwave frequency for resonance.

For a fixed incident frequency, if the cavity radius decreases, the cavity length should increase to keep the microwave resonating in the cavity. For convenient in experiment, what we fix is the cavity radius, and tune the cavity length with a sliding short to make the cavity a resonant cavity at a certain microwave frequency.

However not all the radiuses are permitting the microwave propagating into the cavity, there exists a radius called cutoff radius, below which the EM wave cannot propagate into the cavity, the cutoff radius will be discussed in the next section.

3.2.3 Remarks

There are some important remarks on the microwave resonant: the resonant mode structures, cutoff radius, how to apply the theory to select a resonant mode and cavity, electric field distributions.

- The resonant mode structures: In perfect microwave resonant cavities, if the microwave frequency is fixed, the resonant modes will depend on the cavity geometry, the structure of TM_{mnp} modes are shown in Figure 3.5, the n index ranging from 1 to 3, and the p index varying from 0 to 3, where the red colors are maxima electric field values, blue colors are the minima electric values; in the figure when we fix the cavity radius and increase cavity length, p index will increase, it is the same to the n index, when we fix the cavity length and increase the cavity radius; notice that, the lowest resonant TM mode is TM_{010} in the upper left corner, this mode has only one resonant in radial direction, no resonant in angular and axial direction, the fields in these two directions are uniform; the TM_{011} mode, only has one resonant in radial and axial direction respectively.

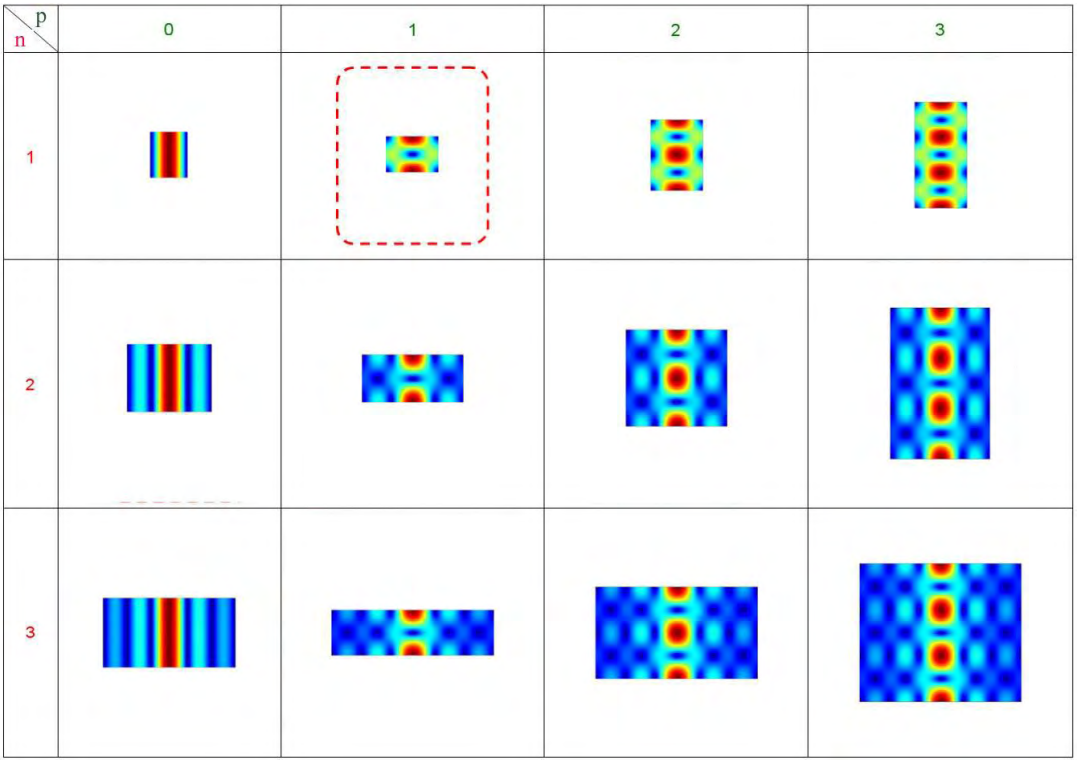

Figure 3.5: Details of the electric field distribution in TM_{mnp} cylindrical cavity modes, for n and p indices ranging respectively from 1 to 3 and from 0 to 3. The cavities were dimensioned so that their resonant frequencies remain identical and are to scale. Mode surrounded by a red dashed line is TM_{111} mode. Silva et al. 2009 [4].

- Cutoff radius: however, in case the frequency is fixed, not all the geometries have the capability for the microwave resonance, due to the cutoff radius for a certain microwave frequency. To understand the cutoff radius we could look into equation (3.60), if the cavity length L [illegible], then the axial wave number $k_x = p\pi/L = 0$, which means no wave can propagate along the axial, the wave is cut off, and the related cavity radius is so called a cut off radius.

For instance, an incident microwave frequency is f_{ri}, for an arbitrary p in TM_{mnp}, applying L [illegible] into equation (3.60), we can obtain the cutoff radius:

(3.61)
$$R_c(m,n) = \frac{\nu_{mn}}{2\pi\sqrt{\epsilon\mu}f_{ri}}$$

one cannot get the resonant mode TM_{mnp} with the cavity radius smaller than $R_c(m,n)$.

- Mode selection and radius selection: for several purposes, the resonance mode of our application is chosen to be TM_{111}, and the radius of the cavity (R) is chosen to be 5.0 cm:

1, As talked above, with TM_{111} mode, we can have the least resonant in axial direction, which is the simplest mode in axial resonance, the electric field in this mode

also focuses on the axes due to the TM mode boundary condition: $E_x(x, R, \varphi)=0$, which makes the plasma ignition easily start on the side wall, and the resonant easily be excited by a simple coaxial cable antenna.

2, According to equation (3.60), when the incident microwave is 2.45 GHz, the cavity radius (R) and length (L) have the relation of below:

$$(\frac{\nu_{01}}{R})^2 + (\frac{\pi}{L})^2 = 2.6 \times 10^3$$

from which, we can plot the function between [illegible] and L/R as shown in Figure 3.6, all the points on the curl are the geometries can have TM_{011}, there are numberless geometries can have TM_{011} mode for a certain incident microwave. With the radius (R) of 5 cm, the length (L) of the cavity is only 17.05 cm, this cavity size is not too long for the experiment vacuum chamber, and can ensure the excited resonant is TM_{011} mode rather than other modes. The cutoff radius ([illegible]) for TM_{011} mode at 2.45 GHz according to equation (3.61) is also shown in the figure (vertical straight line), is 4.67 cm.

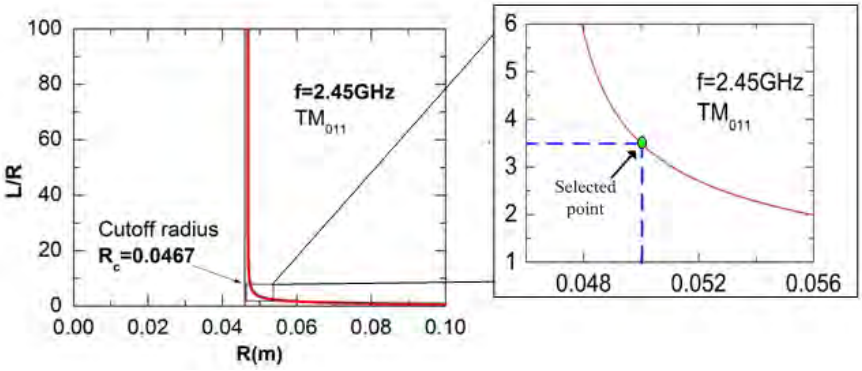

Figure 3.6: Aspect ratio vs radius for TM_{011} mode at 2.45GHz.

Here we choose R=5 cm, not only because we could get a cavity not too long for the experiment, but also because it is one of the standard dimensions for vacuum elements.

- Electric field distribution: from above, we have got a length (L=17.05 cm) for the fixed cavity radius (R=5 cm), for TM_{011} mode, which gives m=0, n=1, p=1, according to equations (3.57)-(3.59), electric field distribution can be calculated and the normalized result is shown in Figure 3.7.

Due to the TM mode boundary condition: $E_x(x, R, \varphi)=0$, electric field is focusing on the axial line of the cavity. This is the analytical result from assuming that the field in the cavity is already in resonant state, due to the resonant, the electric field in the cavity is in standing waves, and the amplitude of the field can be greatly enlarged, hence the energy will be stored.

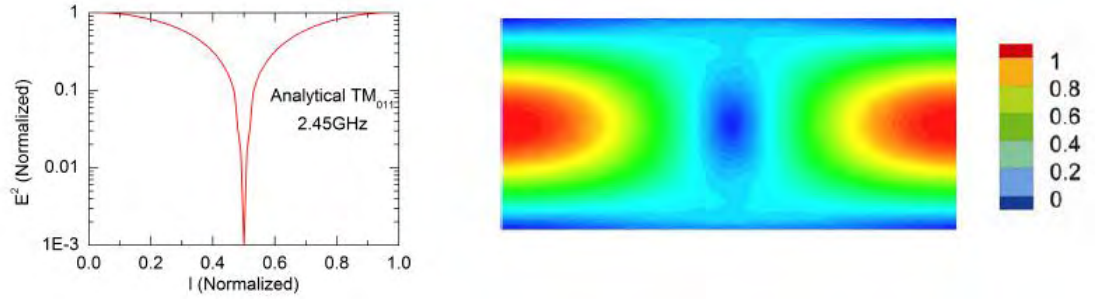

Figure 3.7: Analytical result for TM011 from equations (3.57)-(3.59)*, where m=0, n=1, p=1. The normalized total electric field vs normalized length l along the centerline of the resonant cavity; and the amplitude of normalized total electric field contour plot in 2D.*

Conclusion: If we stick to the analytical formula, we have got a length L for a selected cavity radius above, in this case, we can plot and show the electric field from the analytical formula. However, we are studying real cavities, which cannot be described analytically, because the presence of the excitation source of the microwave will bring a perturbation in the cavity, the cavity will not be perfect cavity anymore, in this case the numerical simulation is required, this will be the content presented in the next section.

3.3 Real Cavity

As talked above, a real microwave resonant cavity needs a properly given excitation source to excite the microwave, the expected resonant mode greatly depends on the ways of the excitation are given; this excitation source will also bring a perturbation to the cavity, in such a situation, the numerical simulation is required. Among the EM wave simulation tools, the code called HFSS is used.

This section we will introduce the HFSS code, apply excitation into a real cavity and simulate it, then we will move on to a real cavity partially filled with dielectric called non-homogeneous cavity and simulate it with HFSS also, in the end we will discuss the Q factor and the way to measure it.

3.3.1 HFSS (High Frequency Structure Simulator)

HFSS (High Frequency Structure Simulator) is a electromagnetic structures solver based on commercial finite element method, with proper boundary conditions and excitation, one can not only calculate the electromagnetic field but also can calculate the Q factor with S parameter (except eigenmode) for a given structured electromagnetic components.

There are three solution types: Driven Model Solution, Driven Terminal Solution,

Eigenmode Solution.

With Driven model solution type, we can use HFSS to calculate the modal-based S-parameters of passive, high-frequency structures such as microstrips, waveguides, and transmission lines. The S-matrix solutions will be expressed in terms of the incident and reflected powers of waveguide modes.

We choose the Driven Terminal solution type when we want HFSS to calculate the terminal-based S-parameters of multi-conductor transmission line ports. The S-matrix solutions will be expressed in terms of terminal voltages and currents.

With the eigenmode solution type, one doesn't need to add an excitation for injecting EM wave, and can calculate the eigenmodes, or resonances, of a structure. The eigenmode solver finds the resonant frequencies of the structure and the fields at those resonant frequencies.

More details about the HFSS code are available in the help file of it. [11]

3.3.2 Excitation

In a real cavity, we need an antenna (or a waveguide) to transmit the microwave energy to the cavity, the excitation coupling techniques must be studied. After choosing a proper excitation method, we can carry out the microwave simulation with the tool of HFSS.

- Excitation techniques: to excite the desired resonant mode efficiently, the exciting field, either external electric or magnetic field should possess at least one component that is similar to the field of the cavity mode that we intend to excite. An antenna coupling into the cavity along the axial line can efficiently excite a TM resonant mode. The coupling antenna is shown in Figure 3.8 on the left.
- HFSS simulation result: Now that the antenna is coupled (size of the antenna: r=0.8 mm, l=10.0 mm) into the cavity (with the selected radius R=5 cm), the microwave frequency is fixed at 2.45 GHz, the simulation result shows that the cavity length in these conditions has to be reduced from L=17.05 cm to L=16.5 cm to ensure the microwave resonant is in TM_{011} mode. The electric field distribution got from HFSS simulation is shown in Figure 3.8.
- The electric field values around the antenna tip are higher than any other positions in the cavity, this leads to an asymmetric electric distribution compared to the electric field distribution in the perfect cavity (Figure 3.8).

When the external microwave load (antenna or waveguide system) is coupled to the cavity to supply the energy, the external load and the cavity together compose a system, the ability of how much this system can store the energy is called Loaded Q factor, which is described in the next section.

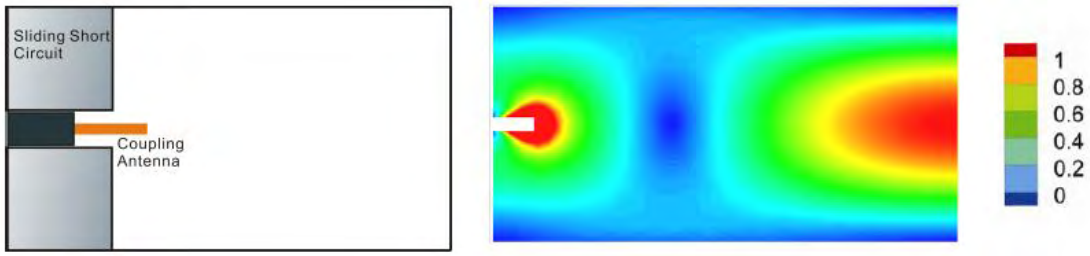

Figure 3.8: A real resonant cavity, microwave is excited by an antenna in TM resonant mode.

3.3.3 Application to a non homogeneous cavity

In the above sections, we have applied the theories to a perfect homogeneous cavity without excitation (section 3.2) and used HFSS calculated a real homogeneous cavity with excitation (section 3.3.2) at 2.45 GHz, this section we will talk about the application to a non homogeneous cavity which is partially filled with dielectric in the cavity, and the cavity is working at 5.8 GHz, which is the one used in Diamant's experiment for microwave resonant plasma cavity [1].

Non-homogeneous characteristics

A cavity partially filled with dielectric is called a non homogeneous cavity, inside of which the permittivity ε and the permeability μ are not uniform.

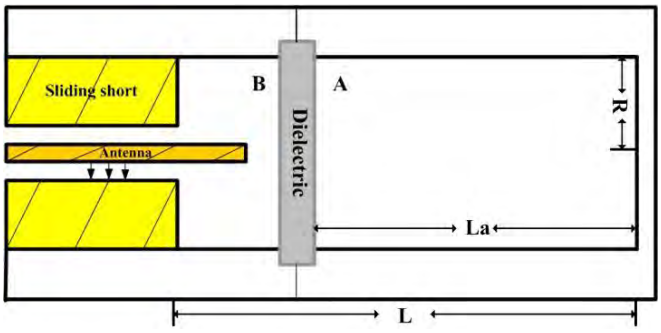

Figure 3.9: Simplified sketch of the resonant cavity

Figure 3.9 shows the cavity used in Diamant's experiment, the cavity radius selected for 5.8 GHz microwave resonant is R=2 cm, the way to select this radius is the same as selecting the radius for 2.45 GHz (presented in section 1.2.4). As we can see in the figure the cavity is partially filled with a dielectric, hence the cavity becomes a non homogeneous cavity, distance from dielectric to the right side wall is La, the total length of the cavity from the sliding short to the right side wall L.

The presence of the dielectric (Quartz) with a bigger permittivity ε than vacuum, can play a role in shortening the resonant cavity, in advance to reduce the cavity size and separate the plasma from the antenna (This can have two advantages: 1, improve the

plasma properties. 2, make the experiment easily valid, because the part A of the cavity is vacuum while the part B is in atmosphere.).

Since now the analytical solution in equation (3.57)-(3.59) cannot describe the fields correctly due to the presence of the antenna and dielectric, so again we use HFSS code to simulate the fields inside of the cavity.

Results from HFSS

With HFSS, the non homogeneous cavity (shown in Figure 3.9) was calculated with microwave at 5.8 GHz, the radius of the cavity is R=2 cm, distance from dielectric to the right side wall is L_a=9.8 cm, dielectric material is Quartz, thickness is 0.4 cm. To achieve a resonant mode of TM_{011}, the length of cavity has to be adjusted by moving the sliding short, the adjusted cavity length L=11.8 cm.

Figure 3.10 shows the normalized electric field 1D distribution along the centerline and 2D in cross section, which is calculated with HFSS, of our non homogeneous cavity.

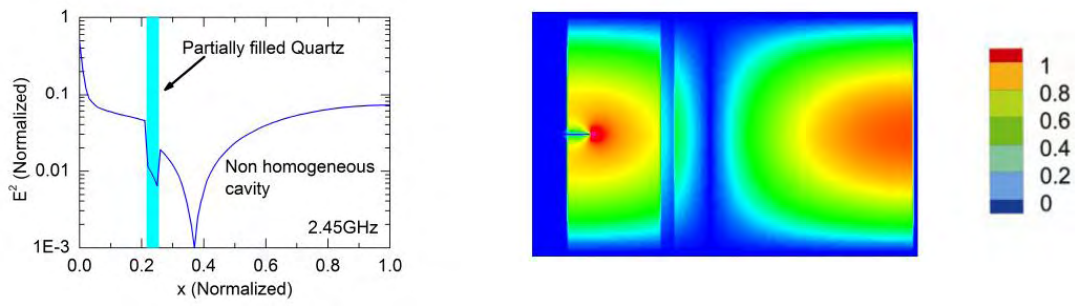

Figure 3.10: Normalized result from HFSS for non homogeneous cavity in TM_{011} mode. The normalized total electric field from HFSS vs normalized length l along the centerline of the resonant cavity; and the amplitude of normalized total electric field contour plot in 2D.

From the electric field distribution we could see that the resonant mode now is a quasi TM_{011} mode. According to the electric boundary condition (3.62) and (3.63), where E_{1t} and E_{2t} are the tangential components of the electric field at the dielectric boundary, $E_{1n}$and E_{2n} are normal components of the electric field at the dielectric surface, indexes 1 and 2 represent outside and inside of the dielectric, ϵ_0 ϵ are vacuum permittivity and dielectric permittivity respectively, the electric field inside of the dielectric is lower than outside of it as in Figure 3.10.

(3.62) $$E_{1t} = E_{2t}$$

(3.63) $$\epsilon_0 \mathbf{E}_{1n} = \epsilon \mathbf{E}_{2n}$$

Due to the resonant, the electric field are greatly enlarged, the maxima value of the electric field is near to the antenna tip on the left of the 1D electric field distribution along the cavity centerline in Figure 3.10, but there would not be a discharge at such a

strong electric field, because in the experiment the volume (volume B in *Figure 3.9*) containing the tuning elements was at atmosphere to prevent breakdown at the tip of the antenna. The plasma breakdown will happen at the electric maxima point near to the right side cavity wall in vacuum volume (volume A in *Figure 3.9*) as shown in the 1D electric field distribution along the cavity centerline. The ability of the cavity can enlarge and store the electric energy could be explained by measuring a Quality factor, which will be presented in the next section.

3.3.4 Quality factor

Quality factor, which is also known as Q factor, is the factor to represent a cavity's ability to store the energy. The higher Q factor a cavity has, the more energy it could store in it.

Definition

Basically, a Q factor of a system (e.g. a cavity and an external load in our case) is known as loaded Q factor can be a composition of an unloaded Q factor, which is due to the volume loss and surface loss of the cavity, and an external Q factor due to the loss in the external load.

Unloaded Q factor

Supposing no external load coupled, but there is the resonant electric field fills the cavity; in general, the permittivity of the dispersive media can have real and imaginary components such that [6]:

(3.64) $\epsilon = \epsilon' - j\epsilon''$

The real part ϵ' represents the familiar lossless media permittivity, ϵ'' is the imaginary part of permittivity attributed to bounded charge and dipole relaxation phenomena, which gives rise to energy loss that is indistinguishable from the loss due to the free charge conduction that is quantified conductivity σ, for convenient we don't use this permittivity (ϵ'') in our case.

Then the Maxwell equation for the magnetic field can be written as:

(3.65) $$\nabla \times \mathbf{H} = j\omega\epsilon'\mathbf{E} + \sigma\mathbf{E} = j\omega(\epsilon' - j(\sigma/\omega))\mathbf{E}$$

Here ω is the radian frequency of EM wave. According to equation (3.11), the time-average energy density stored in the cavity is:

(3.66) $$\varepsilon(x, r, \varphi) = \frac{1}{2}\epsilon' E_0(x, r, \varphi)^2$$

$E_0(x, r, \varphi)$ is the amplitude of the electric field of the EM wave inside of the resonant cavity. So the total energy stored in the cavity can be found by integrating the time averaged energy density (ε):

(3.67) $$W = \int_V \varepsilon(x, r, \varphi)\, \mathrm{d}V$$

The energy-loss densities inside the cavity due to give:

(3.68) $$p_v(x, r, \varphi) = \frac{1}{2}\sigma E_0(x, r, \varphi)^2$$

Hence the total energy loss inside of the cavity is

(3.69) $$P_V = \int_V p_v(x, r, \varphi)\, \mathrm{d}V$$

The of a cavity due to the volume loss is then given by

(3.70) $$Q_V = \omega \frac{W}{P_V} = \omega \frac{\int_V \varepsilon(x, r, \varphi)\, \mathrm{d}V}{\int_V p_v(x, r, \varphi)\, \mathrm{d}V} = \omega \frac{\frac{1}{2}\epsilon' \int_V E_0(x, r, \varphi)^2\, \mathrm{d}V}{\frac{1}{2}\sigma \int_V E_0(x, r, \varphi)^2\, \mathrm{d}V} = \frac{\omega\epsilon'}{\sigma}$$

If the media is non-dispersive and low-conductivity with high-frequency EM wave injected, then there is , we have .

Normally, the wall of a practical resonant cavity is made of good conductor metal instead of a perfect conductor. There are losses on the surface of the wall. The surface losses can be obtained by solving Helmholtz's equation (see in section 3.2) with non-perfect conductor boundary conditions, which gives the accurate field solution of the problem, but it is an onerous task. In practice, for low-loss waveguides made with good conductor walls, the perturbation technique given as follows is suitable.

In practical lossy waveguides, the tangential component of the electric field at the boundary becomes nonzero. The tangential electric field accompanied by the tangential magnetic field forms the Poynting vector pointing **normally** into the wall and gives rise to the attenuation. But in ideal waveguides, the tangential component of the electric field at the boundary is always zero. We recognize that this is the only difference that must be considered, because it is the difference of a finite value from zero.

Compared equation (3.65) with equation (3.3), we can use take place of , then energy density equation (3.11) becomes:

(3.71) $$\varepsilon_{av} = \frac{1}{2}(\frac{1}{2}(\epsilon' - j(\sigma/\omega))\mathbf{E}_{amp}^2 + \frac{1}{2}\mu\mathbf{H}_{amp}^2) = \frac{1}{2}(\epsilon' - j(\sigma/\omega))\mathbf{E}_{amp}^2 = \frac{1}{2}\mu\mathbf{H}_{amp}^2$$

Thus the Poynting vector in equation (3.9) in the good conductor wall surface can be written in a complex way (time-averaged):

(3.72) $$\overline{\vec{\mathbf{S}}} = \frac{1}{2}\mathbf{E}_t \times \mathbf{H}_t = \frac{1}{2}\sqrt{\frac{\mu}{\epsilon' - j(\sigma/\omega)}}\mathbf{H}_t^2\mathbf{n}$$

Where is the unit vector of the wave vector normal to the conductor wall; and denotes the tangential component of the electric field and magnetic field at the cavity wall respectively as above talked. Because we are using a good conductor

which gives$\sigma/\omega \gg \varepsilon'$, so the equation (3.72) becomes:

(3.73)
$$\overline{\vec{\mathbf{S}}} = \frac{1}{2}\sqrt{j\frac{\mu\omega}{\sigma}}\mathbf{H}_t^2\mathbf{n} = \frac{1}{2}(1+j)\sqrt{\frac{\mu\omega}{2\sigma}}\mathbf{H}_t^2\mathbf{n}$$

The real part represents the average power flow density normal to the conducting wall, which is the average surface energy-loss density in the cavity conducting wall [6]:

(3.74)
$$p_s = \overline{S} = \frac{1}{2}\sqrt{\frac{\mu\omega}{2\sigma}}\mathbf{H}_t^2 = \frac{1}{2}\frac{1}{\sigma\delta}\mathbf{H}_t^2$$

Here $\delta = \sqrt{\frac{2}{\mu\omega\sigma}}$ is the Skindepth of a good conductor. The Q of a cavity due to the surface loss is given by:

(3.75)
$$Q_S = \omega\frac{W}{P_S} = \frac{2}{\delta}\frac{\int_V \mathbf{H}^2\,\mathrm{d}V}{\oint_S \mathbf{H}_t^2\,\mathrm{d}S}$$

Then the unloaded quality factor of an unloaded cavity is:

(3.76)
$$\frac{1}{Q_0} = \frac{P_V + P_S}{\omega W} = \frac{1}{Q_V} + \frac{1}{Q_S}$$

That means the Q factor will decrease as the losses are coupled to the system continuously.

Loaded Q factor

When an external load is coupled to the cavity, we define the external quality factor Q_e as follows:

(3.77)
$$Q_e = \frac{\text{Time averaged energy stored}}{\text{Energy loss per radian of oscillation in the external load}} = \omega\frac{W}{P_L}$$

where P_L is the power loss in the external load.

As the begin of this part said, a Q factor of the system is known as the loaded quality factor, denoted by Q_L, and is given by:

(3.78)
$$Q_L = \frac{\text{Time averaged energy stored}}{\text{Energy loss per radian of oscillation in the system}} = \omega\frac{W}{P_{sys}}$$

(3.79)
$$\frac{1}{Q_L} = \frac{P_0 + P_L}{\omega W} = \frac{1}{Q_0} + \frac{1}{Q_e} = \frac{1}{Q_V} + \frac{1}{Q_S} + \frac{1}{Q_e}$$

This is the Q factor we obtain from experiments or simulations. In our case, the cavity is empty, so $Q_V \to \infty$; the main losses are from surface and external load. A typical Q factor normally is around 1000.

Practical definition and measurements of Q factor

Practically, for high values of Q_L, the following definition is also mathematically accurate [13]:

(3.80)
$$Q_L = \frac{f_r}{\Delta f} = \frac{f_r}{f_2 - f_1}$$

Where f_r is the resonant frequency, Δf is the bandwidth which can be measured both in experiment and HFSS code with S parameter. After tuning operation in measurement, the resonant frequency, the bandwidth of an arbitrary EM wave resonant cavity, and S parameter vs tuning frequency are shown in *Figure 3.11*.

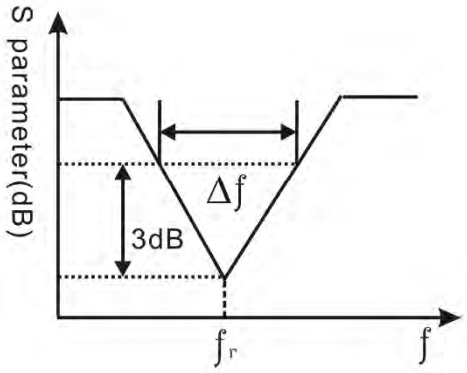

Figure 3.11: S parameter vs tuning frequency. The resonant frequency stays at the bottom of the curl line; and 3dB bandwidth Δf can be found just around the resonant frequency; with both of them, Q factor of this cavity can be calculated by equation (3.80).

Figure 3.12 shows a typical case of Q factor measurement for TM_{010} and TM_{011} with HFSS code, the Q factor of TM_{011} mode is around 845, which is calculated by equation *(3.80)* with the 3dB bandwidth $\Delta f = f_2 - f_1$ and the resonant frequency $f_r = 2.45GHz$.

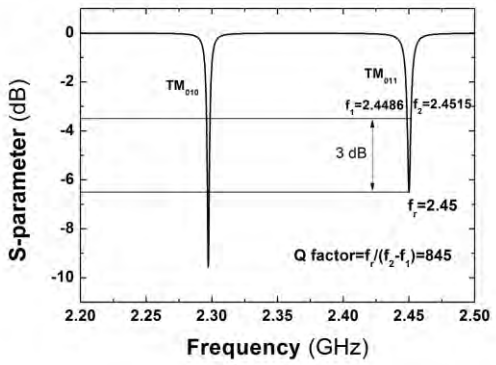

Figure 3.12: A typical Q factor calculation by HFSS using S Parameter; the cavity being calculated is the and 3dB bandwidth $\Delta f = f_2 - f_1$ around the resonant frequency of the cavity f_r; with both of them, Q factor of this cavity can be calculated by equation (3.80).

3.4 Plasma breakdown

After discussing the EM field excited in the microwave cavity without plasma, this section characterizes the plasma breakdown, stressing the pressure influence and showing the early evolution of the plasma discharge with CAVIMO code.

About the threshold

From the work of Raizer [14] on the gas breakdown in microwave fields, the calculated breakdown thresholds are compared with experimental data of argon and xenon. It is found that the smaller the discharge volume and the higher the microwave frequency, the higher the threshold field is. Figure 3.13 presents the microwave field threshold as a function of gas pressure for different excitation frequencies, gas and different diffusion lengths. The field threshold shows a minimum which is equivalent of Paschen minimum for high frequency excited plasma.

Figure 3.13a shows the microwave field threshold as a function of argon pressure for different excitation frequencies and different diffusion lengths. When the excitation frequency increases from 0.99 GHz to 2.8 GHz, the argon breakdown threshold increases by a factor of 10.

Figure 3.13b shows the microwave field threshold as a function of **xenon** pressure at 2.8 GHz with a diffusion length Λ of 0.10 cm (diffusion length Λ is introduced in section 4.2.1, equation 4.11).

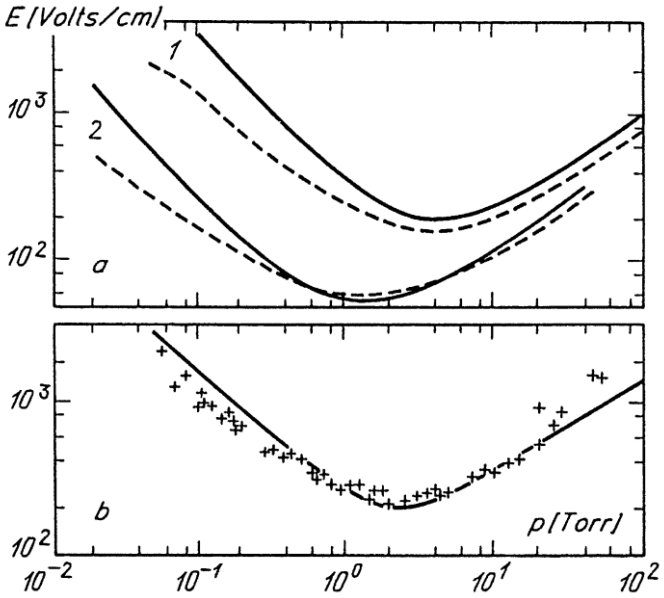

Figure 3.13:Thresholds of microwave breakdown: (a) Ar, (1) f = 2.8 GHz, Λ = 0.15 cm; (2) f = 0.99 GHz, Λ = 0.63 cm; (b) Xe, f = 2.8 GHz, Λ = 0.10 cm. Solid curves, results of calculations; dashed curves and crosses give experimental data. Λ is the diffusion length depends on the resonator size.[14].

With the model described in chapter 2 and used in this thesis, we are able to define the microwave breakdown power (and the corresponding threshold electric field) for a given pressure.

To find the minimum breakdown power, we set a relatively low initial electron density (10^{12} m^{-3}), and fix the gas pressure at different levels (from 20 mTorr to 200 mTorr). To obtain breakdown in the simulation, we progressively increase the microwave power, from a low level, until the electron density continuously grows. The breakdown threshold field is found as a RMS (root mean square) amplitude at the maximum resonant point at the end of the cavity on the centerline as is illustrated in Figure 3.10.

In Figure 3.14, the red curve presents, for our plasma source, the minimum electric field and also the minimum input microwave power required for the plasma breakdown as a function of xenon pressure. The code gives a breakdown value for xenon pressure higher than 10 mTorr. We focus the simulations on the pressure range of interest for our application, which is not higher than 200 mTorr. The minimum power (or electric field) required for breakdown decreases as the xenon pressure increases. 35 W microwave input power is necessary for a 100 mTorr xenon breakdown. The plasma source studied here and after in this thesis is the same cavity as in Diamant's experiment [1], the microwave frequency is 5.8 GHz, and the diffusion length Λ is 0.8 cm (see Figure 3.9). The same curve of Raizer's case as is shown in Figure 3.13 for xenon breakdown threshold at 2.8 GHz and with the diffusion length Λ of 0.10 cm is inserted for a comparison. Since the microwave frequency is higher in our plasma source, the breakdown threshold should be higher, but the diffusion length of our source is also 0.8 cm, which is much bigger than 0.10 cm. This drags the breakdown threshold lower than Raizer's case, as mentioned above. Finally the important feature is that the same trends are found in these two different studies.

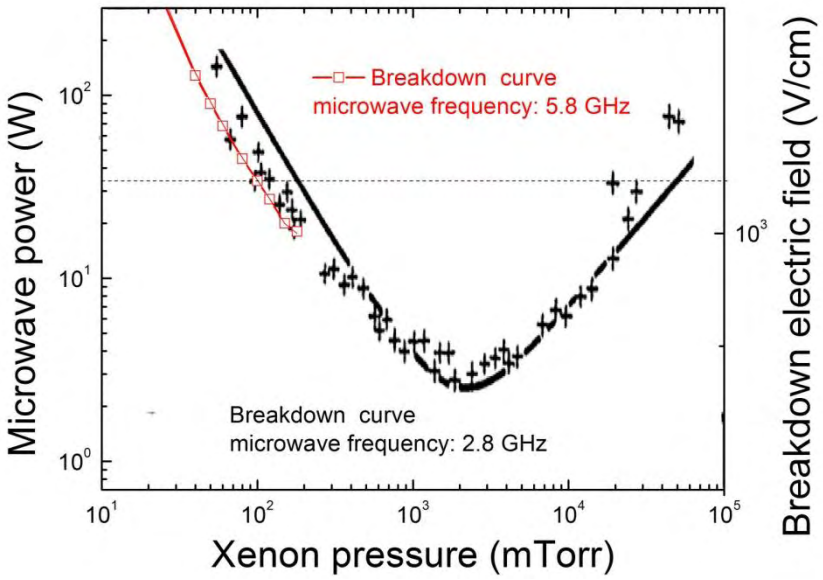

Figure 3.14: (Red curve) The simulation xenon breakdown threshold at 5.8 GHz, with Λ = 0.80 cm; (Black curves) The calculated (solid line) and experimental data (stars) of xenon at 2.8 GHz, with Λ = 0.10 cm, done by Raizer.[14]

Same kind of breakdown curve for a hydrogen microwave plasma produced by elementary ECR source was studied by A Lacoste et al. [15], L. Boufendi et al.[16], Figure 3.15 shows the microwave power required to obtain plasma breakdown, to sustain the plasma, and to obtain visually uniform plasmas as a function of hydrogen pressure. Even if the plasma source and gas are different, discharge is difficult to trigger under 70 mTorr, the minimum power required for breakdown appears around 1 Torr.

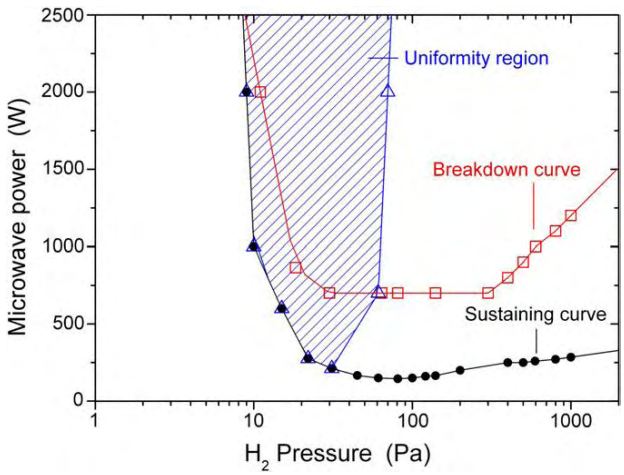

Figure 3.15: Microwave power required to achieve plasma breakdown, to sustain the plasma, and to obtain visually uniform plasmas as a function of hydrogen pressure [15].

About the plasma phases from the breakdown to steady state

To study the plasma phases from the breakdown to steady state, we carried out a simple simulation to show the plasma density and electric field distribution at different time steps.

In this simulation, the gas density is uniformly fixed at 100 mTorr, initial electron density is set to be 1 10^{12} m^{-3}. Cavity radius R is 2 cm, the length L_a of the space for the plasma volume is 10 cm, the geometry is shown in Figure 3.9, this geometry gives a diffusion length Λ of 0.8 cm.

To excite the electric field of TM_{011} mode at 5.8 GHz, a preliminary study has been done with HFSS by carefully adjusting the antenna length inside of the cavity.

Figure 3.16 shows electron density and axial RMS electric field $\mathbf{E}_x$ spatial distribution at several time steps during the early breakdown of the plasma.

Between 5 μs to 97 μs, the volume discharge is ignited: the plasma density increases but remains lower than the critical density (4.2 10^{17} m^{-3} for 5.8 GHz, as was talked in section 2.4.1). So the plasma relative dielectric constant [illegible] (see equation 2.33) is positive but smaller than 1, this gives a plasma dielectric constant smaller than the vacuum permittivity: [illegible], hence according to equation (3.61), the cutoff radius R_c increases and becomes bigger than the one calculated with [illegible], the microwave is cut off by the cavity in the plasma volume, but still is absorbed near to the dielectric. Because the electric field is higher in the vicinity of the dielectric than deeper in the plasma, as shown in time step 97 μs, the plasma forms faster near to the dielectric.

As the discharge carrying on, as shown in time step 110 μs, the plasma density reaches the critical density. The microwave electric field is reflected by the part of the plasma whose density is higher than the critical density, due to the superposition of the forward coming and the backward coming wave, there forms a high electric field front.

After 130 μs time step, the plasma is continuously heated by the electric field within a skindepth, the volume discharge gradually becomes weak, and the plasma grows in the vicinity of the dielectric.

Then after 210 μs, due to the ambipolar diffusion, the plasma with high density (25 times of overcritical density is found in the vicinity of dielectric) finally fills most of the plasma volume.

At time step of 600 μs, the plasma almost reaches steady state, we can see that electron heating in the volume disappears, the plasma is only heated in the skin.

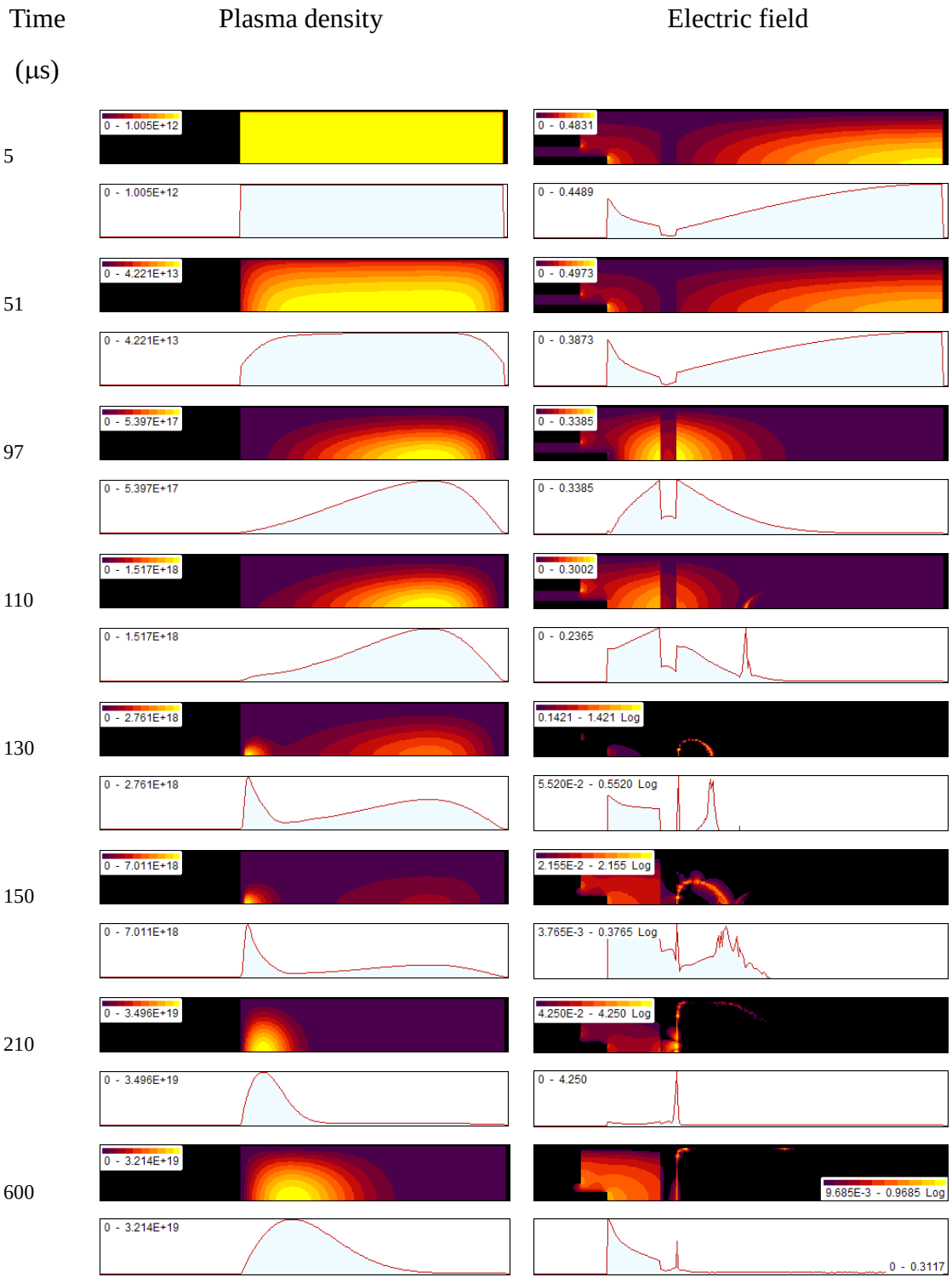

Figure 3.16: Plasma densities and electric field distribution at different times during the plasma formation. Microwave frequency f = 5.8 GHz, input power 60 W, under fixed gas pressure of 100 mTorr. Electric field is normalized. Plasma density values are in m^{-3}.

3.5 Conclusion

- Theoretical analysis of the TM mode microwave resonant cavity can be found in this chapter, a resonant cavity formula (equation (3.60)) to describe the resonant cavity was derived:

$$f_r|_{TM_{mnp}} = \frac{1}{2\pi\sqrt{\epsilon\mu}}\sqrt{(\frac{\nu_{mn}}{R})^2 + (\frac{p\pi}{L})^2}$$

this equation can give the dimension of an arbitrary TM resonant mode cavity for a frequency fixed incident microwave.

- For radius selection, we focus on the TM_{011} mode, the cutoff radius (R_c) for TM_{011} resonant modes at different frequencies could be found in the equation above by fixing the frequency and let [illegible] (e.g. R_c=4.67 cm at 2.45 GHz), however, the cavity radius (R) was chosen to be 5.0 cm due to the vacuum facilities in our experiment at 2.45 GHz, the perfect cavity length was estimated by the above equation to be about L=17.05 cm.

- In a real cavity, excitation techniques for a real cavity are introduced, and a microwave coupling antenna was positioned to be coincident with the central axis of a cavity, to supply the same electric field as the TM_{011} mode as for excitation.

- HFSS (High Frequency Structure Simulator) was employed to investigate the excitation in the real cavities. The simulation results from HFSS for the resonant cavity (R=5.0 cm) tuning with an exciting antenna (l=1.0 cm, r=0.081 cm) are shown in Figure 3.8.

- With the same method of radius selection and excitation techniques, non homogeneous cavities partially filled with a dielectric (Quartz, [illegible]) operated at 2.45 GHz and 5.8 GHz were studied, the cavities are simulated with HFSS. For the non homogeneous cavity operated at 2.45 GHz, the cavity radius was kept the same as before R=5.0 cm, the HFSS simulation results for the cavity tuning at [illegible] mode are shown in Figure 3.17 (in open squares). The electric field simulated with HFSS for 5.8 GHz non homogeneous cavity at TM_{011} mode is shown is Figure 3.10.

- The Q factor for a non homogeneous resonant cavity is measured by both HFSS simulation and experiment in our team.

- The microwave power required for xenon breakdown in the TM_{011} mode resonator at 5.8 GHz under 100 mTorr is 35 W. The required power goes up when the pressure decreases.

- Plasma breakdown starts near to the microwave electric field peak at the end of the cavity, firstly grows with the volume discharge and then grows in the vicinity of

the dielectric to a high plasma density (25 times of critical density for 5.8 GHz) by being heated by the microwave within a skindepth.

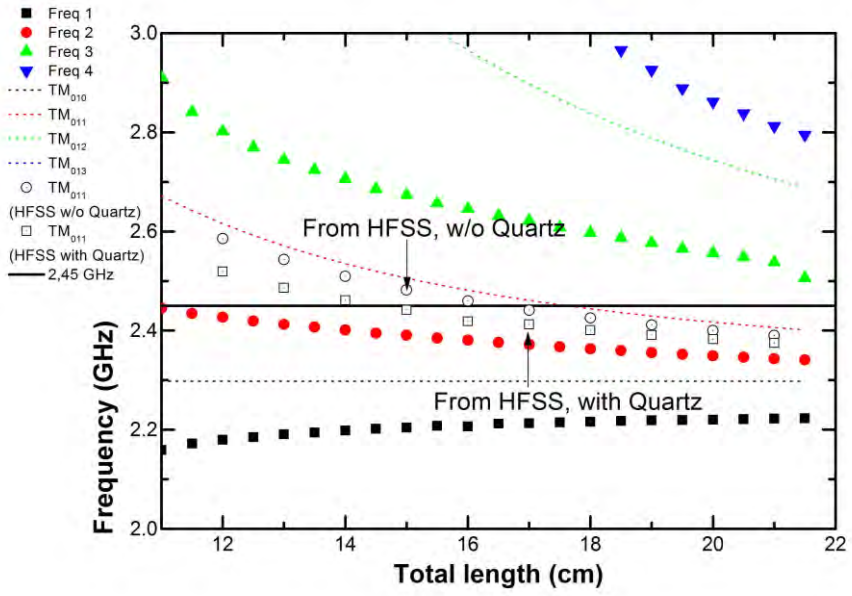

Figure 3.17: Tuned cavity length (L) versus frequency with fixed cavity radius (R=5 cm), dashed lines are theoretical results of different resonant modes corresponding to different colors (black TM_{010}, red TM_{011}, green TM_{012}, blue TM_{013}), open symbols are simulation results from HFSS (open circles are results only with antenna excitation, open squares are results with Quartz partially filled), solid symbols are results from experiment measurements (solid square TM_{010}, solid circle TM_{011}, solid square TM_{012}, up-triangle is TM_{013}).

3.6References

[1] Diamant, K. D. Resonant Cavity Plasma Electron Source. *Plasma Science, IEEE Transactions on*. **37**(8): 1558-1562 (2009)

[2] Diamant, K. D. Resonant Cavity Hollow Cathode. *41st AIAA/ASME/SAE/ASEE Joint Propulsion Conference & Exhibit*. 10-13 July *2005*, Tucson, Arizona

[3] Diamant, K. D. Plasma Measurements in a Resonant Cavity Hollow Cathode. *42nd AIAA/ASME/SAE/ASEE Joint Propulsion Conference & Exhibit*. 11 July 2006, Sacramento, CA.

[4] Silva, F., K. Hassouni, et al. Microwave engineering of plasma-assisted CVD reactors for diamond deposition. *Journal of Physics: Condensed Matter*. 21(36): 364202 (2009)

[5] Harrington, R. F. *Time-Harmonic Electromagnetic Fields*. (Wiley-IEEE Press; 2nd edition, 2001)

[6] Zhang, K. and D. Li. *Electromagnetic Theory for Microwaves and Optoelectronics*. (Springer,2007)

[7] Maxwell, J. C. *A Dynamical Theory of the Electromagnetic Field*. (Wipf & Stock Publishers , 1996)

[8] Jackson, J. D. *Classical Electrodynamics*. (Wiley; 3rd ed, 1999)

[9] Panofsky, Wolfgang K. H.; Phillips, Melba. *Classical Electricity and Magnetism*. (Dover; 2nd ed., 2005)

[10] Maxwell, J C. *A Treatise on Electricity and Magnetism*. (Dover, 1873)

[11] HFSS. *Online help*. http://www.scribd.com/doc/82687895/Ansoft-HFSS-Online-Help.

[12] Taflove, A. *Computational Electrodynamics: The Finite-Difference Time-Domain Method, Third Edition*. (Artech House, 2005)

[13] Petersan, P. J. and S. M. Anlage. Measurement of resonant frequency and quality factor of microwave resonators: Comparison of methods. *Journal of Applied Physics*. 84(6): 3392-3402 (1998)

[14] Raizer, Y. P. *Gas Discharge Physics*. (Springer, 1991)

[15] Rayar, M., H. L. Quoc, et al. Characterization of hydrogen microwave plasmas produced by elementary sources in matrix configuration. *Plasma Sources Science and Technology*. 18(2): 025013 (2009)

[16] A. A. Fridman, L. Boufendi, T. Hbid, B. v. Potapkin, and A. Bouchoule. Dusty Plasma formation: Physics and critical phenomena. Theoretical approach. *Journal of Applied Physics*. Vol 79: 1303-1315 (1996)

Chapter 4: Physics and modeling of the microwave plasma source

In this chapter we present and discuss the physics of the microwave plasma source using the models described in the previous chapter. We first use a zero-dimensional (0D) global model to estimate the order of magnitudes of the main plasma parameters and to understand how they vary with pressure and injected power. We will see, by comparing the results with those of the 2D model that the 0D global model gives estimates of the plasma density, electron temperature, and other plasma properties, that are surprisingly close to those of the 2D model when gas heating and gas flow are not taken into account. We then describe in details the results from the 2D model for a typical case (with and without gas flow and gas heating included). Finally we present a parametric study of the plasma properties as a function of pressure and microwave power, and some comparisons with the experimental results of Diamant.

The model is applied to a cylindrical cavity (dimensions 10 cm length, 2 cm radius) in xenon, at pressure in the 20-200 mtorr range and for absorbed microwave power between 10 and 100 W. The plasma properties are presented with and without taking into account gas flow and gas heating. The question of electron extraction from the microwave source is not treated in this chapter and will be discussed in the next chapter.

The conditions of the simulations and the plasma chemistry model are described in section 4. In section 4.2 we present the principles of the 0D, global model of the discharge, and discuss the results obtained with this model. The results from the 2D model for a typical operating point (pressure and power) are presented in section 4.3 first with a fixed gas density (4.3.1), and then taking into account gas flow and gas heating (4.3.2).A parametric study of the 2D model in a large pressure and power range is presented in section 4.4 where the model results are also compared with experiments.

4.1Conditions of the simulations and xenon plasma chemistry

Geometry of the cavity

The cavity is a cylinder as shown in Figure 4.1. The cavity is partially filled with a quartz window (with a relative permittivity of 5.6 for 5.8 GHz), which separates the cavity into a plasma volume (A) and a volume where the microwave power is injected

(B). The cavity radius and plasma volume length are R = 20 mm and L = 100 mm, respectively. The plasma volume is $V = \pi R^2 L$ and the total inside wall area is $A = S_1 + S_2 + 2\pi RL$, which are dielectric surface and cavity side wall surface respectively. This cavity is designed for TM_{011} resonant mode at 5.8 GHz.

The Q factor of this non homogenous cavity is around 1000 calculated from simulations with the HFSS code (see chapter 2) and this value is in good agreement with the Q factor measurement performed in our group on an experimental microwave cavity. With this quality factor, when the resonant is set in the cavity, the electric field can be 30 times enlarged, and supplies enough electric field strength for plasma breakdown which happens on the axial of the cavity side wall. After breakdown the plasma develops toward the dielectric wall and grows until steady state is reached.

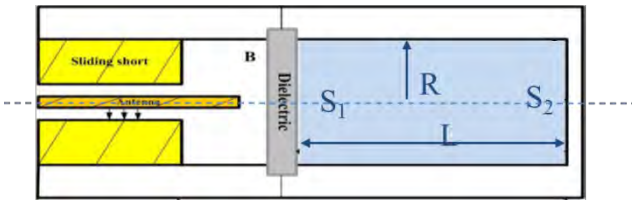

Figure 4.1: Geometry of the microwave source. The plasma simulation domain is the cylinder in blue (R=2 cm, L=10 cm).

Xenon plasma chemistry and reaction rates used in the models

The 0D and 2D models assume a Maxwellian electron distribution function of the electrons. As mentioned in chapter 3, we use a simple xenon chemistry model based on the reactions represented in Table 5. Other models can be found in the literature [1]-[3]. The aim of this model is not to describe the complete xenon chemistry, but to provide a reasonable estimation of the total ionization of xenon, including direct ionization from the ground state of xenon, and stepwise ionization from the metastable state $1s^5$.

Reaction	Type	Rate (m^3s^{-1})
$e^- + Xe \rightarrow e^- + Xe$	elastic	K_{el}
$e^- + Xe \rightarrow e^- + Xe*$	Metastable excitation	K_{ex}
$e^- + Xe* \rightarrow 2e^- + Xe^+$	Stepwise ionization	K_{sw}
$e^- + Xe* \rightarrow e^- + Xe$	Metastable de-excitation	K_{de}
$e^- + Xe \rightarrow 2e^- + Xe^+$	Ionization	K_{iz}

Table 5: Xenon chemistry used in the 0D and 2D models.

The rates of the reactions of Table 5 are calculated by integrating the electron impact cross-sections of the corresponding reactions over a Maxwellian electron distribution function. The electron-xenon cross-sections used in the calculations come from the SIGLO database [4] and are displayed in Figure 4.2. The rate of de-excitation from the metastable state is deduced by classical detailed balancing, using a statistical weight of 5.

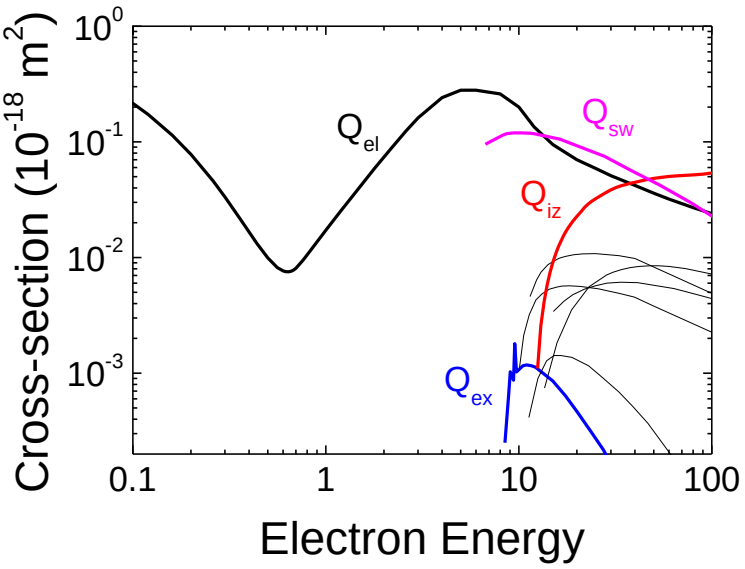

Figure 4.2: Electron impact cross-sections for xenon (from siglo data base, at [4]). Q_{el}, Q_{ex}, Q_{iz}, and Q_{sw} are the cross sections for elastic collisions, metastable ($1s^5$) excitation, direct ionization and stepwise ionization, respectively.

These cross-sections are used to calculate the rates K_{el}, K_{ex}, K_{iz}, K_{sw} and K_{de} (de-excitation of the metastable state), assuming a Maxwellian electron distribution function, using Bolsig+ [5]. The other cross sections represented on the figure are electron impact excitation cross-sections (other than excitation to the $1s^5$ metastable state) and are used in the calculation of the electron energy loss rate for total electron impact excitation. The energy threshold of metastable excitation, direct ionization, and stepwise ionization are 8.31, 12.12, and 3.44 eV respectively.

The 0D and 2D models use the rates coefficients of Table 5 in the source term of the particle balance equations (0D model, see below), or continuity equations (see description of the 2D model in chapter 2) for the charged particles and metastable state. The collision terms of the electron energy balance or energy equation use energy loss (or gain, for the case of de-excitation) rate coefficients that can also be simply deduced from the rate coefficients. The energy loss corresponding to a given electronic excitation noted "j" is simply equal to the corresponding energy threshold E_j, multiplied by the associated rate K_j calculated by integration over a Maxwellian, as in Figure 4.3. The total excitation energy loss $\Sigma E_j K_j$ is obtained by summing the contributions of all the electron impact excitation collisions represented in Figure 4.2.

The energy loss corresponding to ionization is simply $E_{iz}K_{iz}$ where E_{iz} is the energy threshold for xenon ionization (12.12 eV). The electron energy loss rates due to elastic collisions, metastable excitation, and direct ionization are displayed in Figure 4.4 as a function of electron temperature.

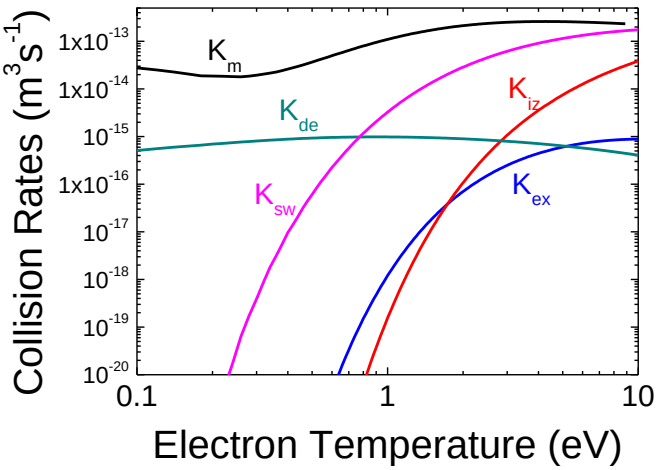

Figure 4.3: Rate coefficients as a function of electron temperature for the reactions of Table 5, calculated from the cross-section data of Figure 4.2, assuming a Maxwellian electron distribution function.

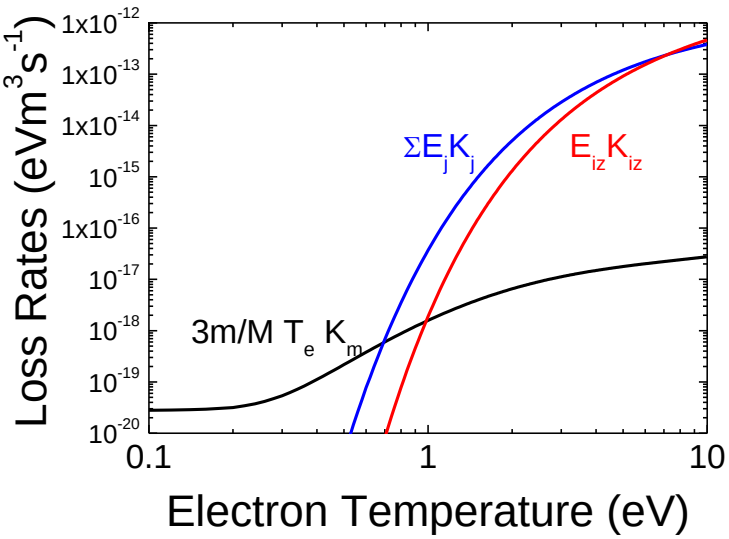

Figure 4.4: Electron energy loss rate coefficients corresponding to elastic collisions (black line), total electronic excitation (blue), and ionization (red) as a function of electron temperature, calculated from the cross-section data of Figure 4.2 assuming a Maxwellian electron distribution function.

The energy loss coefficient for stepwise ionization and de-excitation (energy gain) can

be simply deduced from the corresponding rates of Figure 4.3.

4.2 Results from a 0D, global model

A 0D, global model can be very useful to get a first order description of the plasma under the conditions described above and can form the basis to understand and discuss the results from the more complex 2D model. A 0D model is based on global equations describing the production and losses of charged particles and neutral particles (e.g. excited states) and the balance between power injected, power absorbed by the particles and power lost to the walls. It does not describe the details of the transport of particles and energy in the discharge volume but takes into account the particles and energy transported to the walls.

The global model and the space 2D dependent models used below are based on the same simplified plasma chemistry model of xenon described in the previous section. This model includes electrons, xenon ions, metastable, and ground state xenon atoms, the density of which are noted as n_e, n_i, n_m, and n_g, respectively. The xenon atoms, metastable and xenon ions have the same masses, noted M, while the mass of electrons is noted m_e. The considered reactions and rates coefficients are defined in Table 5 and the rates are displayed in Figure 4.3 and Figure 4.4.

In section 4.2.1, we give the basic equations of the 0D model and then present and discuss the results. The results are briefly summarized in section 4.2.2.

4.2.1 0D model presentation and results

As described in classical books on the subject [6]-[7], in a low pressure global model, the particle balance equation relates the ionization rate integrated over the discharge volume, to the charged particle losses (Bohm flux) at the surfaces integrated over the chamber walls. The power balance relates the power absorbed by electrons in the plasma to the power dissipated by charged particles through collisions in the volume, and carried to the walls.

Particle balance equation

For a simple problem where direct ionization is the only mechanism of charged particle production, and assuming a quasi-constant plasma density n_0(except at the sheath edge) and a constant electron temperature, the global particle balance equation writes:

$$n_0 n_g K_{iz} V = n_s u_B A \qquad (4.1)$$

n_0 is the plasma density and K_{iz} the ionization rate (constant if the electron temperature is constant).The left hand side is the ionization frequency integrated over

the discharge volume *V*, and the right hand side is the charged particles flux to the walls integrated over the wall area *A* and evaluated at the sheath entrance where the plasma density has dropped to the value n_s, and the ion velocity is equal to the Bohm velocity u_B .Defining an effective wall area A_{eff} by

(4.2) $$n_0 u_B A_{eff} = n_s u_B A$$

the balance equation above becomes:

(4.3) $$\frac{K_{iz}}{u_B} = \frac{A_{eff}}{n_g V} = \frac{1}{n_g d_{eff}}$$

where $d_{eff} = V / A_{eff}$ is an effective dimension of the chamber.

The left hand side of this equation depends only on electron temperature, while the right hand side depends on the gas density and discharge dimension. This means that the electron temperature is completely determined by the gas density and discharge dimensions (and does not depend on the power absorbed in the discharge, for a fixed gas density).

The effective wall area A_{eff} , related to the plasma density at the sheath edge by

$$A_{eff} = \frac{n_s}{n_0} A = hA$$

can be estimated by simple arguments but depends on the degree of collisionality of the ions, i.e. on gas pressure[6].

In the limit of low gas pressure and low ion collisionality, the global model above is accurate because the approximation of quasi-constant plasma density and electron temperature is good. At higher pressure, i.e. when the ion mean free path is much smaller than the discharge dimensions, the approximation of constant plasma density is no longer uniform and the model must be improved. In this regime the charged particle fluxes are ambipolar, and are defined by:

(4.4) $$\Gamma = -D_a \nabla n$$

where $n = n_e = n_i$ is the local plasma density.

Assuming direct ionization only, as above, the continuity equation can be written as:

(4.5) $$D_a \Delta n = -n \nu_{iz} \; with \;\; \nu_{iz} = n_g K_{iz}$$

Assuming constant ionization frequency and ambipolar diffusion coefficient, this equation leads, for a cylindrical geometry to a solution that is the product of a cosine profile along the axial direction x, times a Bessel J_0 profile in the radial direction r:

(4.6) $$n(x,r) = n_0 J_0(\chi_{01} r/R)\cos(\pi x/L)$$

Where *R* and *L* are the radius and length of the cylinder respectively and $\chi_{01} \approx 2.405$ is the first zero of the Bessel function J_0.

The continuity equation above is an eigenvalue equation and the conditions of zero density at the wall surface require that:

(4.7) $$\frac{\nu_{iz}}{D_a} = \frac{\chi_{01}^2}{R^2} + \frac{\pi^2}{L^2}$$

This equation is strictly equivalent to (4.1) for the collisional, ambipolar regime, in the sense that it imposes that the total ionization in the volume is balanced by the losses to the walls. In our conditions the electron temperature is much larger than the ion temperature and we can write:

(4.8) $$D_a \approx \mu_i \frac{kT_e}{e} = \frac{kT_e}{M\nu_{in}}$$

where $\mu_i = \frac{e}{M\nu_{in}}$ is the ion mobility and ν_{in} the ion-neutral collision frequency.

For xenon ions in xenon [8], a value of ν_{in} that gives an ion mobility consistent with experimental values of the mobility is $\nu_{in} \approx 1.7 \times 10^6 s^{-1}$ at 0.1 torr, 300 K. We can also write:

(4.9) $$\nu_{in} = k_{in} n_g \text{ with } k_{in} \approx 5.3 \times 10^{-16} m^3 s^{-1}$$

From this collision frequency, we can estimate the ion mean free path λ_i with:

$\lambda_i = \frac{u_i}{\nu_{in}}$ where u_i is the ion velocity. An upper limit of λ_i can be obtained when u_i is taken as the Bohm velocity u_B . For an electron temperature around 1 eV (see below), u_B is on the order of 800 m/s in Xe. Combined with the ion collision frequency of 1.7

$10^6\ s^{-1}$ at 100 mtorr, this gives a mean free path λ_i of about 0.5 mm at 100 mtorr. This is much smaller than the discharge dimensions and confirms the assumption above of a collisional, ambipolar regime (this is true for the whole range of pressure we consider here, i.e. between 20 mtorr and 200 mtorr).

Equation (4.4) can be re-written as:

(4.10) $$K_{iz} = \frac{kT_e}{M}\frac{1}{k_{in}n_g^2\Lambda^2}$$

With Λ the characteristic length scale for plasma diffusion:

(4.11) $$\frac{1}{\Lambda^2} = \frac{\chi_{01}^2}{R^2} + \frac{\pi^2}{L^2}$$

Equation (4.10) is the equivalent, for our collisional situation and cylindrical geometry, to equation (4.2), i.e. it provides the electron temperature knowing the gas density and dimensions of the chamber.

In the pressure range we consider in this work, metastable ionization is not negligible and can even be dominant. The contribution of stepwise ionization of the metastable atoms to the total ionization frequency is ($n_m K_{sw}$) and is proportional to the metastable density and to the electron temperature dependent stepwise ionization rate K_{sw}. The metastable density can be obtained from a balance equation for the metastable atoms; these atoms are produced by stepwise ionization of the metastable and destroyed by electron impact de-excitation or stepwise ionization. Assuming that the losses to the walls are small with respect to the volume creation and losses (we will checked this assumption in the 2D model results), we can write:

(4.12) $$K_{ex}n_e n_g = K_{sw}n_e n_m + K_{de}n_e n_m$$

Therefore, the metastable density is proportional to the gas density:

(4.13) $$n_m = \frac{K_{ex}}{K_{sw} + K_{de}} n_g = \alpha n_g$$

where $\alpha = \frac{K_{ex}}{K_{sw} + K_{de}}$ represents the fraction of neutral atoms on the metastable state and is a function of the electron temperature T_e only.

Therefore equation (4.10) can be rearranged as:

(4.14)
$$\boxed{\left(K_{iz}+\alpha K_{sw}\right)=\frac{kT_e}{M}\frac{1}{k_{in}n_g^2\Lambda^2}}$$

This equation provides the electron temperature knowing the gas density and chamber dimensions. Note again that for a given gas density, the electron temperature does not depend on the power absorbed in the discharge.

Equation (4.14) has been solved for different values of gas density or pressure and for the considered discharge geometry, using the rate coefficients as a function of electron temperature given in the previous section. The calculated electron temperature as a function of gas pressure is displayed in Figure 4.5. On this figure is also represented the fractional contribution of the metastable states to the overall ionization, defined as:

(4.15)
$$\eta_i=\frac{n_mK_{sw}}{n_mK_{sw}+n_gK_{iz}}=\frac{\alpha K_{sw}}{\alpha K_{sw}+K_{iz}}$$

We see on Figure 4.5 that the electron temperature is on the order of 1 eV and decreases from about 1.5 eV at 0.02 torr to 0.8 eV at 0.2 torr. These variations look relatively small for a variation of a factor of 10 of the pressure and gas density. One must however keep in mind that the electron rate coefficients vary in a very non-linear way with the electron temperature (see Figure 4.3) so that the relatively small variation in electron temperature over this range of pressure is actually associated with a very large variation of the charged particle volume production frequency and losses to the walls. The contribution η_i of the metastable states to the overall ionization through stepwise ionization is quite large, between 60% and 90% over the range of pressure considered and is smaller at lower pressure, as expected since second kind collisions are less important at lower pressures. The electron temperature when the contribution of metastable to ionization is not included in the calculations is also shown for comparisons in Figure 4.5. We see that the electron temperature must be larger by about 0.2 eV for the discharge to be sustained when stepwise ionization is not included. We will however see below that the plasma density is considerably reduced without metastable ionization.

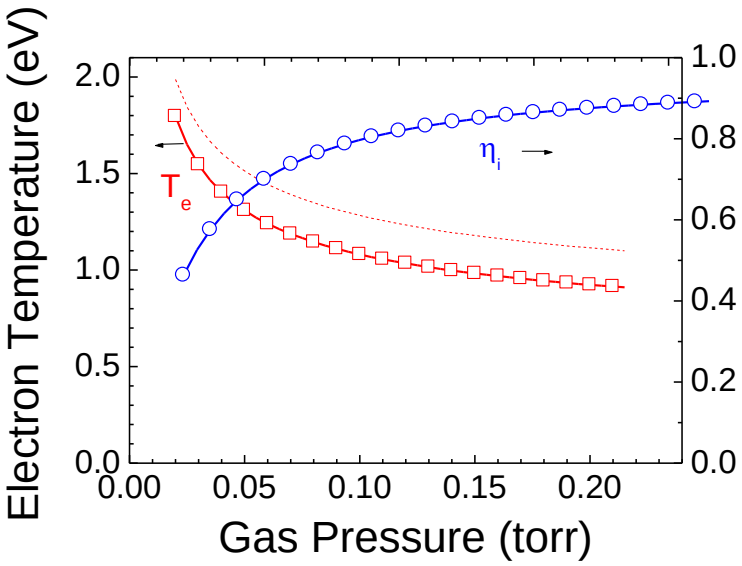

Figure 4.5: Electron temperature T_e and fractional contribution of metastable atoms to the overall ionization, η_i, as a function of gas pressure, in a discharge chamber of radius 2 cm and length 10 cm, from the 0D, global model. The dashed line corresponds to a case where stepwise ionization of the metastable atoms is not considered.

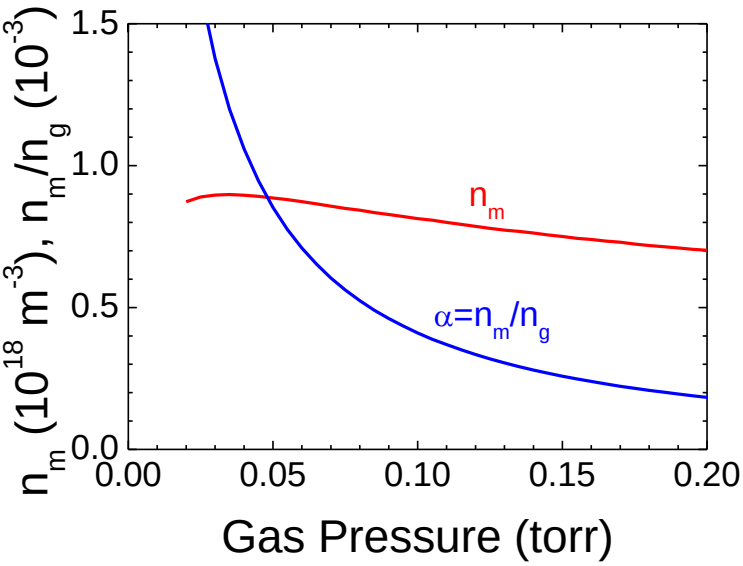

Figure 4.6: Metastable density n_m, and fraction of the neutral gas in the metastable state, α, as a function of gas pressure, from the 0D model (this is independent of absorbed power).

The metastable density, plotted in Figure 4.6, exhibits relatively small variations (slight decrease with increasing pressure) with pressure and is on the order of 10^{18} m^{-3}

in the considered range of pressure. Therefore the relative concentration of metastable atoms decreases with increasing gas density or pressure (close to $1/n_g$ or $1/p$).

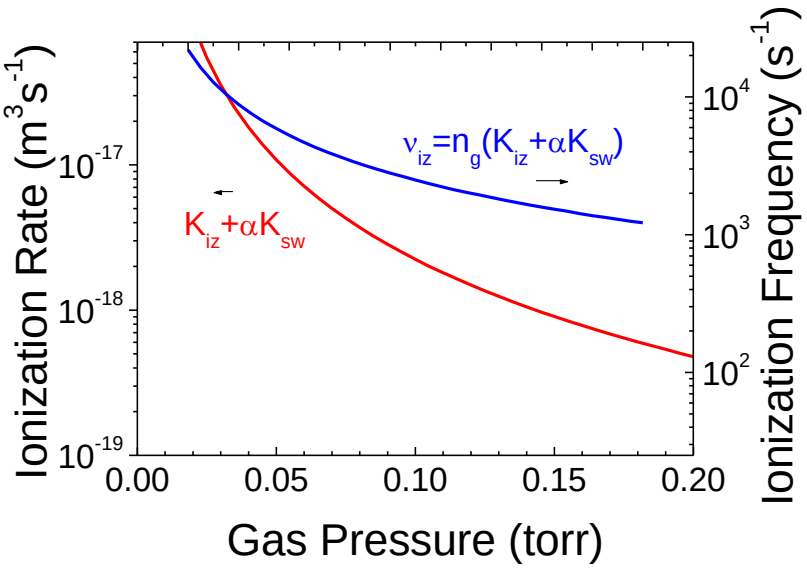

Figure 4.7: Total ionization rate and total ionization frequency (equal to the wall loss frequency) as a function of gas pressure, from the 0D model.

Figure 4.7 displays the total ionization rate and ionization frequency as a function of gas pressure; We see, as mentioned above, that although the variations of the electron temperature (Figure 4.5) are relatively small in the considered pressure range, the ionization rate varies by two orders of magnitude. As expected, the ionization rate and the ionization frequency decrease with increasing pressure. This is because the losses to the walls decrease with increasing pressure.

All the results presented above are independent on the absorbed power because for a given gas density the electron temperature is completely determined by the balance between the losses to the walls and ionization in the discharge volume.

Power balance equation

One quantity that must clearly depend on the absorbed power is the plasma density. The plasma density in a global model [6-7] can be obtained from a simple expression of the power balance in the discharge. The power absorbed in the discharge must be balanced by the losses through collisions in the volume plus the energy losses to the walls. At low pressure the losses to the walls can be quite large. At higher pressure, the energy losses in the volume are dominant.

Before writing the power balance equation, we note that in this global model of a collisional plasma, the plasma density distribution is not uniform (see equation (4.6)) and the electron temperature is supposed to be uniform. The production of charged particles per unit time by ionization in the volume must therefore be obtained by integration over the volume and is given by:

(4.16) $$\left(K_{iz}+\alpha K_{sw}\right)\int 2\pi rn(x,r)dxdr=\left(K_{iz}+\alpha K_{sw}\right)\bar{n}V$$

where V is the discharge volume and $\bar{n}$ the volume averaged plasma density. The density distribution of equation (4.6) can be integrated analytically and one can show that:

$$\int 2\pi rn(x,r)dxdr=n_0 4LR^2\frac{J_1(\chi_{01})}{\chi_{01}}$$

Where J_1 is the Bessel function of first order and $J_1(\chi_{01})\approx 0.52$. The averaged plasma density is therefore related to the maximum density through:

(4.17) $$\bar{n}=n_0\frac{4J_1(\chi_{01})}{\pi\chi_{01}}\approx 0.28n_0$$

The charged particle loss to the walls per unit time is equal to the total production per unit time in the volume and we can therefore write, using equation (4.14):

(4.18) $$\Gamma_s A=n_g\left(K_{iz}+\alpha K_{sw}\right)\bar{n}V=\frac{kT_e}{M}\frac{1}{k_{in}n_g\Lambda^2}\bar{n}V$$

where Γ_s is the charged particle flux at the sheath edge.

Let us now write that the power absorbed by the electrons is equal to the sum of the power lost in the volume and on the surface of the chamber:

(4.19) $$P_{abs}=P_{loss}=\bar{n}VL_C+\Gamma_s A\left(E_e+E_i\right)$$

P_{abs} is the total power absorbed (by electrons) in the discharge, and P_{loss} is the power lost by charged particles, which is composed of volume power losses $\bar{n}VL_C$ and surface power losses $\Gamma_s A\left(E_e+E_i\right)$.

The surface power losses is obtained by multiplying the flux of particles (electron and ions) to the walls integrated over the surface, $\Gamma_s A$, by the sum of the energy carried by electrons and ions to the walls, respectively E_e, and E_i. In the volume loss term, L_C is the energy loss per electron per unit time by electrons due to collisions in the

discharge volume.

Using (4.18) the power balance equation becomes:

(4.20) $$P_{abs} = \Gamma_s A\left[E_c + E_e + E_i\right] = \frac{kT_e}{M}\frac{1}{k_{in} n_g \Lambda^2}\bar{n}V\left[E_C + E_e + E_i\right]$$

with

(4.21) $$E_C = \frac{L_C}{n_g\left(K_{iz} + \alpha K_{sw}\right)}$$

E_C is the energy lost by electrons in the volume for per electron-ion pair generation.

The averaged plasma density is extracted from the power balance equation above, to give:

(4.22) $$\boxed{\bar{n} = \frac{P_{abs}}{V}\frac{M}{kT_e}\frac{k_{in} n_g \Lambda^2}{E_T}}$$

with $E_T = E_C + E_e + E_i$; E_T is the total energy loss per electro-ion pair to the walls.

We now detail the different energy loss terms, E_e, E_i, and E_C.

For a Maxwellian distribution function, the energy carried by electron to the walls is classically given by:

(4.23) $$E_e = 2kT_e$$

The ion energy carried to the walls by ions includes the energy gained in the Debye sheaths $kT_e/2\ln\left[M/(2\pi m)\right]$ (directly deduced from the Debye potential) plus the ion energy at the sheath entrance, $kT_e/2$ (from the Bohm velocity). Therefore:

(4.24) $$E_i = \frac{kT_e}{2}\left[1 + \ln\left(\frac{M}{2\pi m}\right)\right]$$

Note that this ion energy loss corresponds to the energy transported to the walls and does not include the energy deposited by ions through collisions in the gas. These

losses can lead to gas heating. It is difficult to get an exact analytical expression for the losses by ions in the volume (Joule heating). In order to keep the global model simple, we neglect these losses for the moment, and we will check in the complete 2D simulations that these losses represent actually a small percentage of the total power dissipated in the discharge (see Figure 4.21 and the comment on it).

We therefore only consider electron energy losses. The energy lost per electron per unit time, as written in the electron energy equation [6] is:

$$L_C = n_g K_{el} T_e \frac{3m_e}{M} + n_g \sum_j E_j K_j + n_g E_{iz} K_{iz} + n_m E_{sw} K_{sw} - n_m E_{de} K_{de} \qquad (4.25)$$

This expression accounts for electron losses due to elastic collisions (first term), total electronic excitation (second term), direct ionization (third term), stepwise ionization (fourth term), and de-excitation (last term).

The energy loss rates for elastic collision, total excitation, and ionization, respectively $K_{el} T_e \frac{3m_e}{M}$, $\sum_j E_j K_j$, and $E_{iz} K_{iz}$ are plotted as a function of electron temperature on Figure 4.4. The energy loss rates for stepwise ionization and de-excitation can be deduced by multiplying the rate coefficients K_{sw} and K_{de} of Figure 4.3 by the corresponding energy threshold (respectively 3.44 and 8.31 eV).

From equations (4.21) and (4.25), we get the expression of E_C:

$$E_C = \frac{K_{el} T_e \frac{3m_e}{M} + \sum_j E_j K_j + E_{iz} K_{iz} + \alpha \left(E_{sw} K_{sw} - E_{de} K_{de} \right)}{K_{iz} + \alpha K_{sw}} \qquad (4.26)$$

Equation (4.22) shows that for a given gas density, since the electron temperature is independent of the absorbed power, the plasma density varies linearly with absorbed power. Figure 4.8 displays the variations of the plasma density obtained with this expression, as a function of gas pressure and for different values of the absorbed power, from 10 to 60 W. This figure confirms the linear increase of the plasma density with power at constant gas density, and shows, as expected an increase of the plasma density with increasing pressure for a given absorbed power.

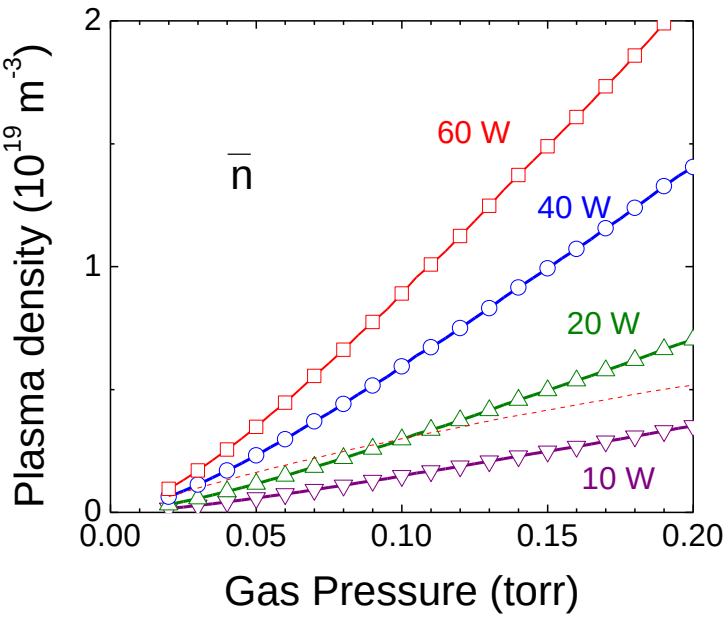

Figure 4.8: Averaged plasma density as a function of gas pressure and for different absorbed power, from the 0D model. The dashed line corresponds to the 60 W case when stepwise ionization of xenon metastable atoms is not considered. The averaged plasma density is related to the maximum plasma density by equation (4.17) (i.e. the maximum plasma density is about 3.5 larger than the averaged plasma density).

The results displayed in Figure 4.9 show that under our conditions the energy lost to the wall per electron-ion pair created, E_C does not vary strongly with gas pressure and is on the order of 40 eV. Since E_e and E_i depend only on electron temperature which does not present very large variations in the considered pressure range, we can deduce that the total energy lost per electron-ion pair to the wall, $E_T = E_e + E_i + E_C$ does not strongly depend on pressure.

It appears on Figure 4.8 that the plasma density for a given power increases almost linearly with pressure or gas density. This can be understood by looking at the expression of the plasma density, equation (4.22). The denominator of eq.(4.22) depends only slightly on gas pressure since it contains only E_T and T_e which weakly depend on the gas pressure in our pressure range. The numerator is proportional to the ion collision frequency and therefore to the gas density or gas pressure. The absorbed power therefore behaves almost as a linear function of the gas density or gas pressure.

The total energy loss per electron-ion pair (Figure 4.9) to the wall is a very important parameter since it determines the discharge efficiency. When designing an electron source, the energy cost per electron extracted must be minimized. The maximum current of electron that can be extracted from our source is equal to the total electron and ion current to the walls.

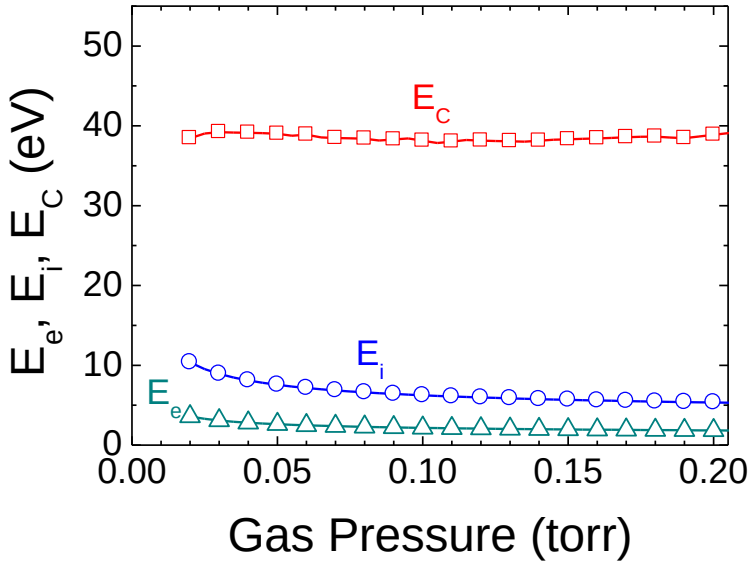

Figure 4.9: Electron E_e, ion E_i energy losses to the walls, and electron energy loss per electron-ion pair to the wall, E_C as a function of electron temperature (see the definitions in eqs. (4.23), (4.24), and(4.26), respectively).

The minimum energy cost per extracted electron is therefore equal to E_T, is on the order of 50 eV. This means that, for a power of 60 W, the maximum electron current that can be extracted is eP/E_T i.e. is on the order of 1.2 A in our conditions.

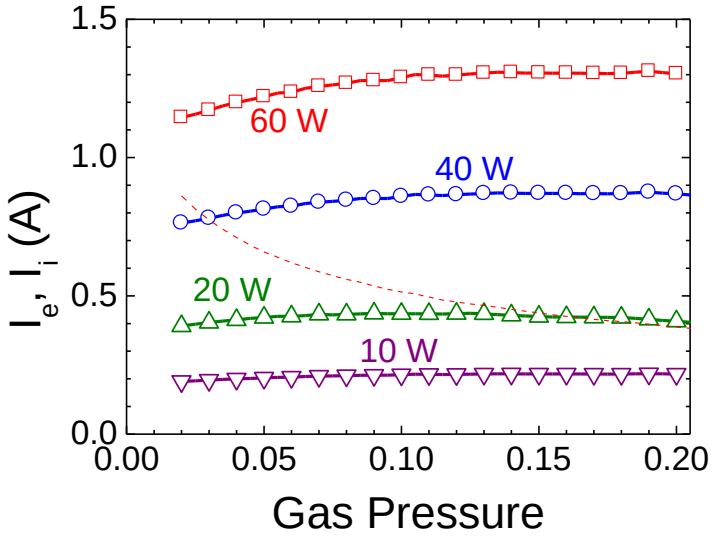

Figure 4.10: Total electron and ion currents to the wall as a function of gas pressure and for different values of the absorbed power. The dashed line corresponds to a power of 60 W without taking into account metastable ionization.

This is confirmed in Figure 4.10 which displays the electron and ion current to the walls as a function of gas pressure and for different values of the power absorbed in the discharge. The current in this figure are deduced from the following equation (see

equations (4.20) and (4.18):

$$I_e = I_i = e\Gamma_s A = e\bar{n}Vn_g\left(K_{iz} + \alpha K_{sw}\right) = \frac{eP_{abs}}{E_T} \tag{4.27}$$

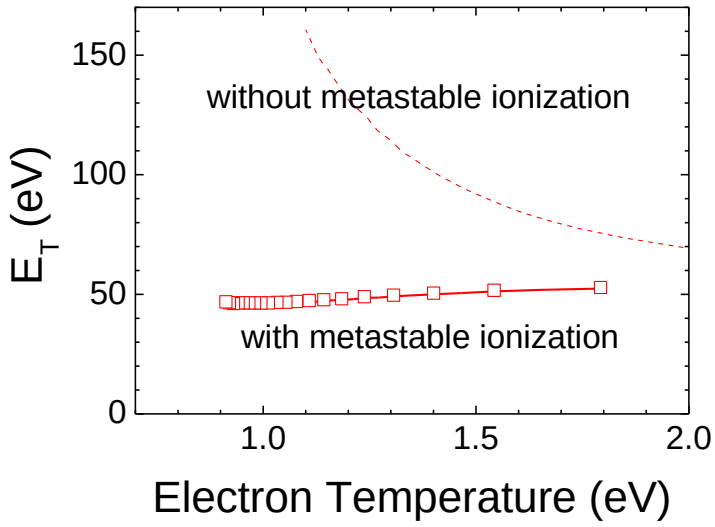

Figure 4.11: Total energy loss per electron-ion pair to the wall for 60 W , as a function of electron temperature with and without taking into account ionization of the metastable state.

We see on Figure 4.10 and on Figure 4.11 that the xenon metastable plays a very important role in our conditions. At 100 mtorr and 60 W, the extracted electron current is more than twice smaller if the contribution of metastable atoms is not included. The presence of metastable atoms leads to a significant reduction of the energy cost to create an electron-ion pair, as seen in Figure 4.11, and therefore to a better efficiency of the source. We also see on Figure 4.10 and on Figure 4.11 that this effect tends to decrease at lower pressures (higher electron temperature) because of the increase of the electron temperature.

Note finally that equation (4.27) and Figure 4.10 give the maximum electron current that is available in the plasma for extraction. The question of electron extraction from the source is treated in the next chapter.

4.2.2 Summary and conclusion

The 0D model, based on global particle balance and power balance equations provides a simple way to estimate the main plasma parameters for given absorbed power and gas density.

The results from a 0D model in the considered conditions (xenon, discharge in a

cylinder of length 10 cm and radius 2 cm, pressure range from 20 mtorr, to 200 mtorr, power between 10 and 60 W) can be summarized as follows:

- the electron temperature in the plasma (independent of the absorbed power at fixed gas density), decreases from 1.5 to 0.8 eV when the gas pressure increases from 20 to 200 mtorr.
- The contribution of stepwise ionization of the metastable atoms is important and represents 60 to 90% of the total ionization. The metastable density stays on the order of 10^{18} m^{-3} in the considered range of pressure (gas density between 3 10^{20} and 3 10^{21} m^{-3}.
- The plasma density is on the order of 2 10^{19} m^{-3} for a pressure of 0.1 torr and an absorbed power of 60 W. The plasma density increases linearly with power for a fixed gas density, as expected, and increases "almost" linearly with pressure at constant power. The plasma drops by more than a factor of 4 at 60 W if stepwise ionization is not included in the model.
- The total energy lost per electron-ion pair to the wall is almost constant in the considered pressure range (20 mtorr-200 mtorr) and is on the order of 50 eV. On this 50 eV, 2 eV are carried by electrons to the walls, about 6 eV are carried by ions to the walls and the rest is spent by electron collisions with neutral atoms in the discharge volume.
- For a plasma electron source, the total energy loss per electron-ion pair to the walls represents the minimum energy cost per extracted electron and determines, for a given power, the maximum electron current that can be extracted. From the 50 eV energy loss per electron-ion pair to the walls obtained with the 0D model (which does not vary significantly with pressure and power in our conditions), we can deduce that the maximum electron current that can be extracted e.g. for a 60 W absorbed power is 1.2 A, i.e. 20 mA/W.

4.3 2D model results for a typical case

In this section we present in details the 2D model results for a typical operating point where the pressure is set to 0.1 torr at 300 K and the absorbed power is 60 W.

We first present the results obtained for a fixed gas density (section 4.3.1) and then show and discuss the results when gas flow and gas heating are taken into account (section 4.3.2). In section 4.3.1 we show that the 2D results are not very sensitive to the exact profile of the power absorbed in the discharge, and that the complexity of the plasma-Maxwell problem can actually be simplified by assuming a given profile of the power absorbed by the electrons in the skin depth, at the edge of the plasma below the quartz window.

The results of this section are summarized in 4.3.3.

4.3.1 Fixed gas density

In the 2D simulations reported in this section, the gas density is fixed at **100 mtorr** and the input power is **60 W**.

As explained in the chapter 2, electrons are described with continuity and momentum equations under the drift-diffusion approximation. The collision rates are obtained assuming a Maxwellian electron velocity distribution function, with a local temperature deduced from an energy equation. Ions are described with a continuity equation and a momentum equation accounting for inertia, and assuming an ion temperature equal to the neutral background temperature. The ambipolar electric field controlling the charged particle fluxes in the momentum equations is obtained from solutions of Poisson's equations.

The heating term in the electron energy equation can be deduced from the coupling of the plasma model with Maxwell's equations or can be imposed. Results obtained by coupling Maxwell's equations to the plasma model are described in section 4.3.1.1. The results show that the energy is absorbed, as expected, in a thin layer (skin depth) next to the quartz window. The skin depth in our conditions is very small because of the large plasma density. A detailed and accurate description of the Maxwell-plasma coupling therefore requires a very fine numerical grid and leads to cumbersome calculations. We therefore decided to check whether or not the simulated plasma properties were very sensitive to the exact spatial distribution of the absorbed power. The results showed that, for a total, given absorbed power, the plasma properties (space distribution of the plasma density, electron temperature, metastable density, plasma potential) were practically not changed when the spatial distribution of the absorbed power was significantly changed (this is described in section 4.3.1.1). Therefore most of the results presented in the rest of the thesis after section 4.3.1.1 have actually been obtained by imposing a spatial profile of the absorbed power (all the power was supposed to be absorbed in a 1 mm layer below the quartz plate).

Another important question is the influence of gas flow or gas heating on the simulation results. To better understand the role of gas flow due to pumping and gas heating due to the power deposition, we first performed simulations for fixed gas pressure and temperature (i.e. ignoring gas flow and gas heating). The results in this case are presented in section 4.3.1 (the first sub-section describes the influence of the power deposition profile and the second sub-section provides a detailed description of the plasma properties for fixed gas density). In section 4.3.2, we present the results obtained when gas flow and gas heating are included.

4.3.1.1 Numerical description of the microwave-plasma coupling

When the microwave-plasma model was developed we first decided to fully describe

the coupling between the plasma equations and Maxwell's equations, as discussed in the model description of chapter 2. The first simulations showed that, as expected, the power was absorbed by electrons in a thin layer between the quartz plate and the plasma (the skin). Since the coupling of Maxwell's equations with the plasma equations can be computationally intensive (the skin depth is very small with respect to the chamber dimensions, which imposes a large number of grid points), we decided to study the sensitivity of the calculated plasma properties to the details of the space distribution of the absorbed power. This point is discussed in this section.

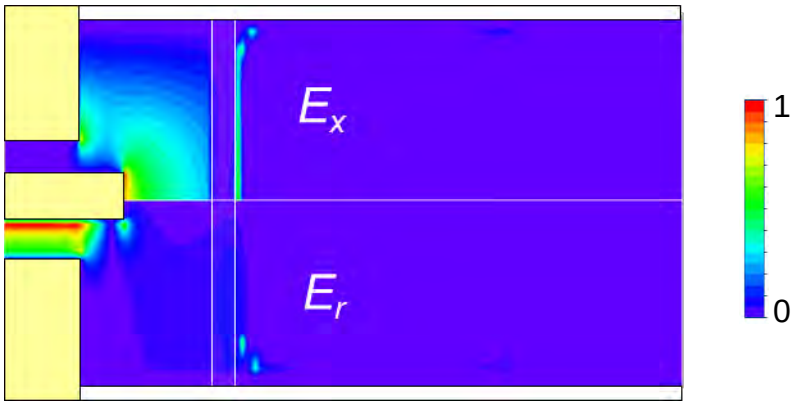

Figure 4.12: Space distribution of the amplitudes of the axial (top) and radial (bottom) electric field for a 60 W, 5.8 GHz (TM) microwave discharge at 100 mtorr in xenon, in the geometry of Figure 4.1. The quartz plate is represented by two parallel white lines.

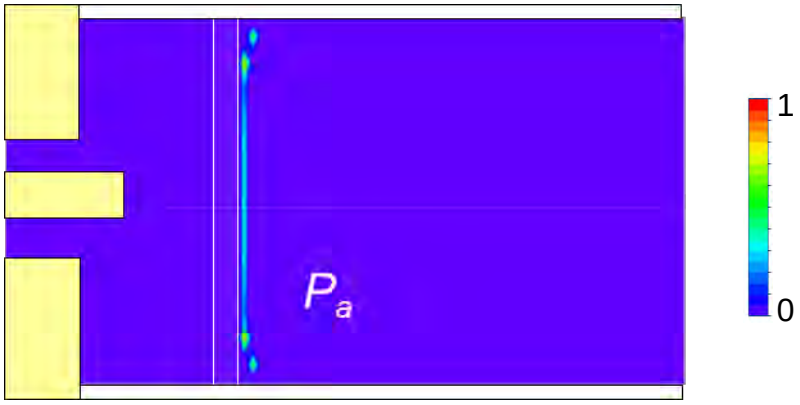

Figure 4.13: Space distribution of the calculated absorbed power for a 60 W, 5.8 GHz microwave discharge at 100 mtorr in xenon, in the geometry of Figure 4.1(same conditions as Figure 4.12).Maximum value on axis, $4x10^7 W.m^{-3}$.

Figure 4.12 displays the spatial distribution of the amplitudes of the components of the electric field calculated with the fully coupled Plasma-Maxwell model for a 60 W absorbed power, 5.8 GHz TM wave, at 100 mtorr in xenon. We see that the electric

field is quickly absorbed by the plasma. The axial component of the electric field is much larger than the radial component and provides the dominant component to the electron heating.

The distribution of the power absorbed by the electrons in the same conditions is shown in Figure 4.13

Under these conditions, the calculated plasma density (see below) is much above the critical density, and the field cannot penetrate very deep into the plasma. Most of the power is absorbed by the electrons in a very thin layer (the skin) at the plasma edge below the quartz plate. The absorbed power is almost uniform radially except in the corners of the cavity, next to the quartz plate. Because the skin depth δ is much smaller than the dimensions of the cavity, the plasma-Maxwell model requires a very small grid spacing (most of the power is absorbed on a few grids in the calculations of Figure 4.12 and Figure 4.13) and this may lead to cumbersome calculations.

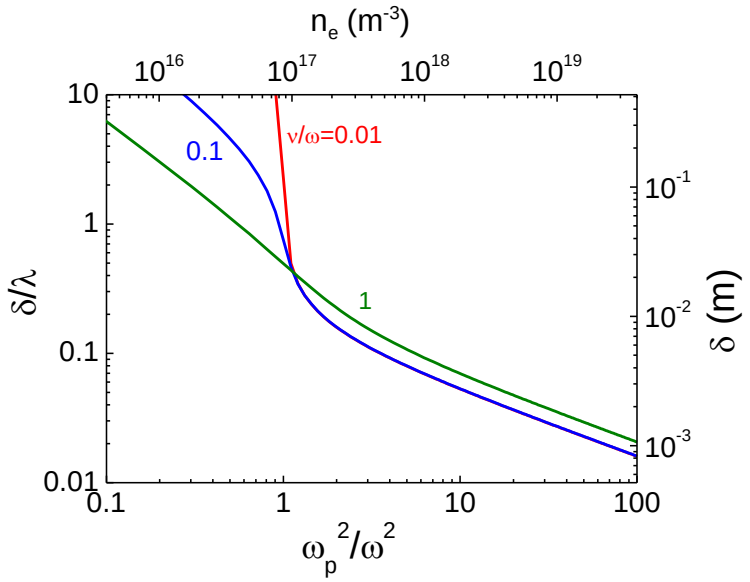

Figure 4.14: Skin depth to wavelength ratio, δ/λ from the Drude model as a function of $(\omega_p/\omega)^2$ (ω_p is the plasma frequency, ω the microwave angular frequency) and for different values of ν/ω (ν is electron collision frequency). The scales on the right and top axis indicate the corresponding values of the skin depth and plasma densities for a value of the wave frequency corresponding to our conditions: 5.8 GHz (experiments of Diamant). At 100 mtorr in xenon, ν/ω is on the order of 10^{-2}.

The skin depth can also be estimated from the complex permittivity of the plasma deduced from the Drude model (see chapter 3). From the Drude model, on can show that the skin depth normalized to the wavelength is a function of the plasma angular frequency and electron collision frequency normalized to the wave frequency, as shown in Figure 4.14. For our conditions at 5.8 GHz, 100 mtorr and 60 W, we will see below that the maximum plasma density, next to the quartz surface, is on the order of $2\ 10^{19}$ m^{-3} and the electron collision frequency is about $3\ 10^{8}$ s^{-1} (so ν/ω is on the

order of 10^{-2}). Figure 4.14 confirms that the skin depth is on the order of 1 mm in these conditions. For this low value of ν/ω the analytical expression of the skin depth tends to the collisionless limit, i.e. to c/ω_p where c is the speed of light. For a plasma density of $2\ 10^{19}$ m^{-3}, the electron plasma angular frequency is about $3\ 10^{11}$ s^{-1} (about 10 times the angular frequency of the 5.8 GHz wave) and this simplified expression of the skin depth gives a value around 1 mm, in agreement with Figure 4.14.

Since the skin depth is very small with respect to the plasma dimensions, the question arises of the necessity or not to describe very accurately the power absorption in the skin depth, i.e. of the sensitivity of the plasma model results to the exact profile of the power deposition at the plasma edge. To check this sensitivity we have performed simulations with the plasma model only and assuming a given profile of the power absorption (i.e. without solving Maxwell's equations). Comparisons between results from the full plasma-Maxwell model and the plasma model with imposed absorbed power in a layer of variable thickness are shown below. The aim is to study the sensitivity of the results to the details of the spatial distribution of the absorbed power.

Figure 4.15 shows the axial variations of the main plasma properties for a 60 W, 100 mtorr 5.8 GHz microwave discharge in xenon. These results have been obtained 1), with the full Maxwell-plasma model, and 2) with only the plasma model assuming that the microwave power is aborbed uniformly in a plasma slab just below the quartz plate. Different values of the slab thickness have been tested in the simulations. We see on Figure 4.15 that the profiles of plasma density, electron temperature, metastable density and plasma potential are actually not very sensitive to the profile of absorbed power.

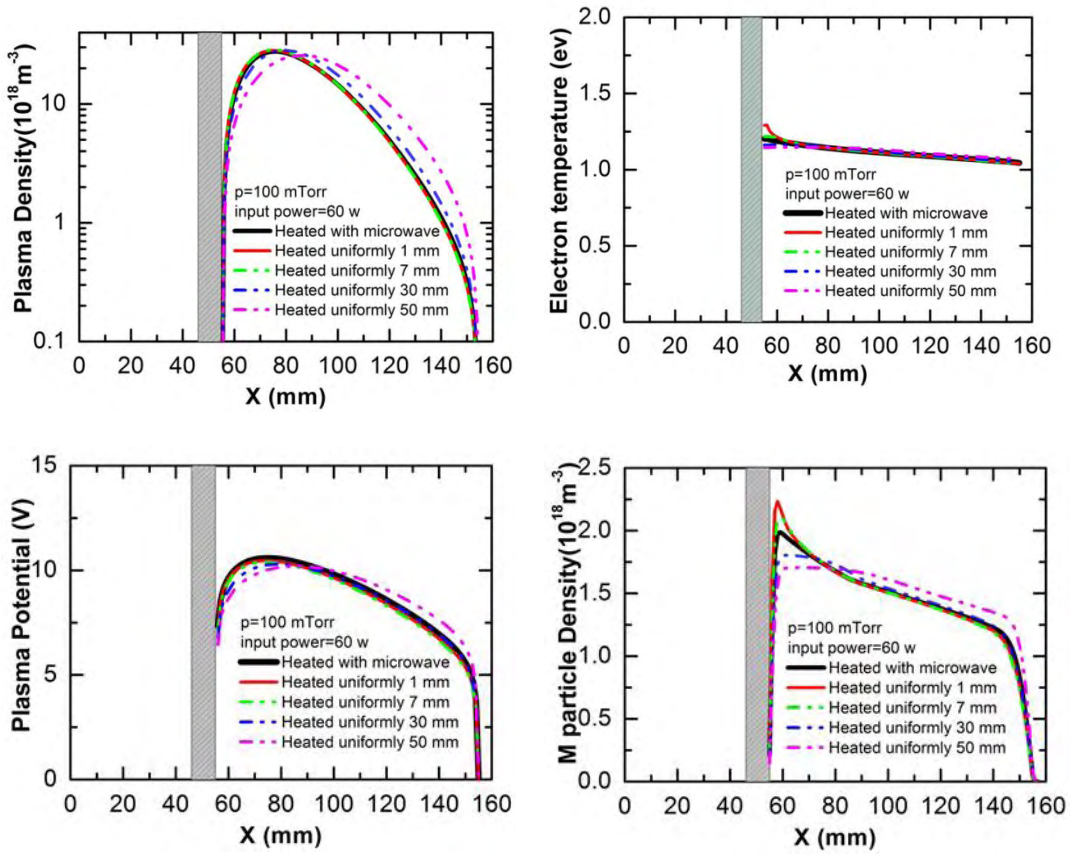

Figure 4.15: Axial profiles of the plasma density, electron temperature, plasma potential, and metastable density calculated for an absorbed power of 60 W at 100 mtorr and 5.8 GHz (geometry of Figure 4.1), with the full Maxwell-plasma plasma, and with the plasma model only, assuming different spatial profiles of the absorbed power (uniform heating in a plasma slab of thickness 2mm, 7 mm, 30 mm, or 50 mm just below the quartz plate).

When the power is supposed to be absorbed in a layer of 1 mm at the plasma edge, the results obtained with the plasma model are very close to those from the full plasma-Maxwell simulation. Even if the power is supposed to be abbsorbed in a much larger plasma layer, of 7 mm below the quartz plate, the obtained plasma properties are not very different from those of the full plasma-Maxwell model. More significant deviations from this model appears when the power is supposed to be absorbed in layers of 30 or 50 mm. The fact that the results from the plasma model are not very sensitive to the exact profile of the absorbed power is consistent with the fact that (as will be discussed below) the 0D model seems to provide very good estimations of the plasma properties (in a 0D model, the power deposition is necessarily uniform over the discharge volume).

We conclude from these comparisons of Figure 4.15 that the full coupling between the plasma equations and Maxwell's equations is not necessary in our conditions (and does not actually bring any new insight in our understanding of this microwave source)

and that one can simply assume that the imposed power is absorbed in a thin layer below the quartz plate. The simulations presented in the rest of this thesis have therefore been performed assuming that the power is absorbed in a 1 mm layer below the quartz plate.

The results of the simulation in the 60 W, 100 mtorr case are discussed in more details in the next two sections (with fixed gas pressure and temperature in section 4.3.1.2, and taking into account gas flow and gas heating in section 4.3.2).

4.3.1.2 Description of the 2D model results for a fixed gas density

In this section the gas pressure (100 mtorr), gas temperature (300 K), and gas density are supposed to be constant.

Figure 4.16 shows the 2D simulation results for the source with the geometry of Figure 4.1. The plasma density distribution in the discharge chamber, electron temperature, metastable density, and plasma potential are shown in Figure 4.16 (a), (b), (c), (d), respectively. The 2D results show a maximum value of 2.8 10^{19} $m^{-3}$of the plasma density on the discharge axis at about 20 mm from the dielectric surface. From this maximum, the plasma density decreases by a factor of about 10 over 8 cm along the discharge axis. This relatively fast decrease is consistent with ambipolar diffusion in this collisional regime.

Note also that the calculated plasma density in the 2D model is in remarkably good agreement with the estimation of the 0D model (where the averaged plasma density was about 10^{19} m^{-3} and the metastable density was around 1 10^{18} m^{-3} at 100 mtorr, 60 W) . The difference between the 2D and 0D model are mainly due to the fact that the absorbed power is located in a thin layer next to the dielectric wall. This creates a (small) non-uniformity in the electron temperature (slightly larger next to the dielectric wall, see Figure 4.16b).

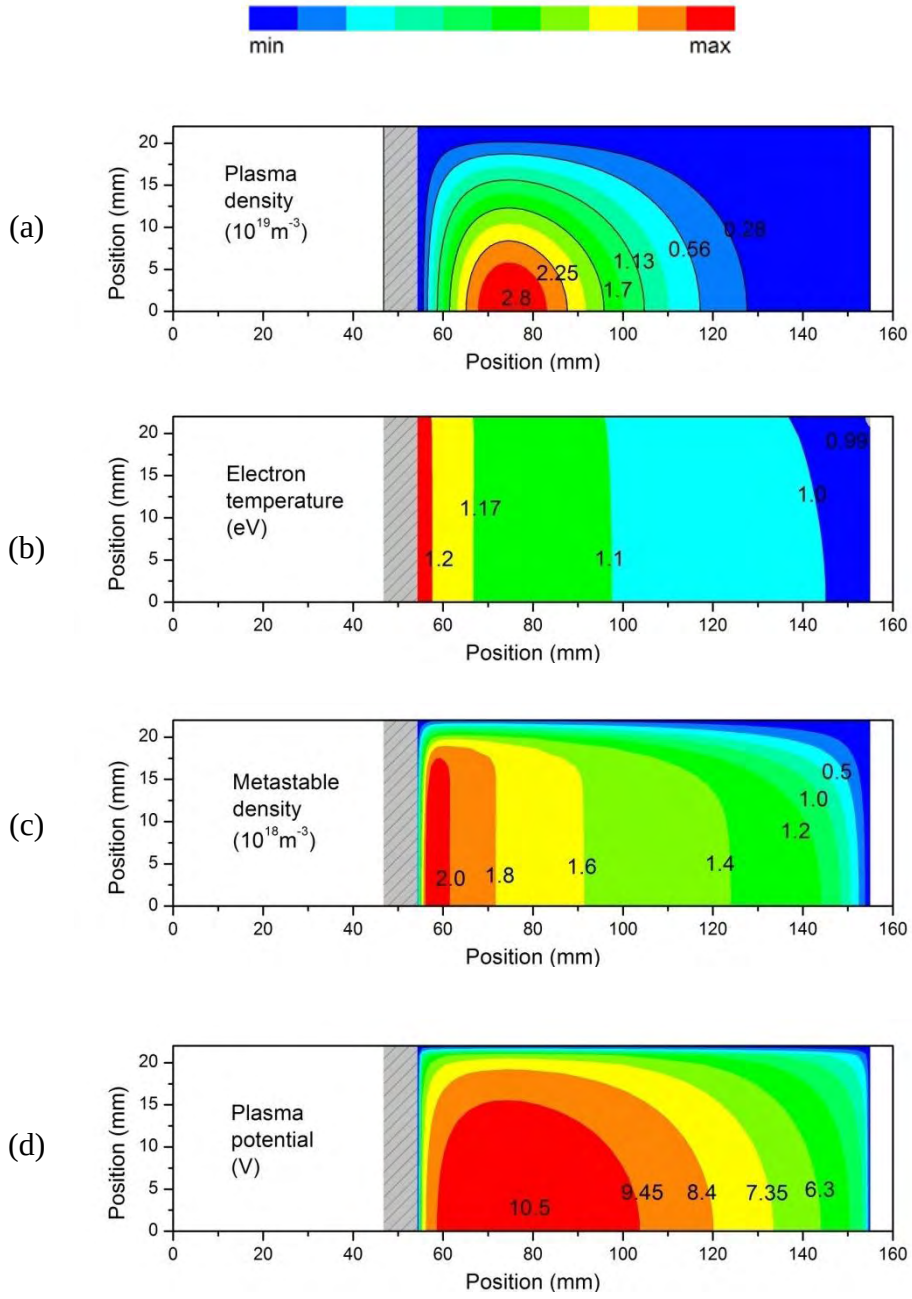

Figure 4.16: 2D distribution of the plasma properties obtained assuming a fixed gas density at 100 mTorr, with an input power of 60 W. a) plasma density, b) electron temperature, c) metastable density, d) plasma potential.

Since the rates are very non-linear functions of the electron temperature, this leads to significantly larger non-uniformities of the metastable density and plasma density (which are larger next to the dielectric wall). The 0D model cannot describe these transport effects. Note that for this reason, we can expect larger differences between

the 0D and 2D model when the pressure increases (smaller thermal diffusion of the electrons).

The electron temperature in the cavity displayed in Figure 4.16b exhibits small spatial variations between 0.99 and 1.2 eV (mainly in the axial direction), again in agreement with the 0D model where the electron temperature was about 1 eV under these conditions. As said above, the electron temperature rises near the dielectric window since the power is supposed to be absorbed in this region.

The metastable density distribution of Figure 4.16c presents a maximum value of $2\ 10^{18}\ m^{-3}$ in the vicinity of the dielectric surface. The metastable density decreases mostly axially, following the variations of the electron temperature. Indeed, the production rate of the metastable is a fast increasing function of the electron temperature around 1 eV (see Figure 4.3) and although the variations of the electrons temperature are not very important, the associated variations of the metastable production are relatively large, which explains the larger metastable density near the dielectric surface where the electron temperature is larger. Also, the reactions involving the metastable atoms are dominant over transport due to diffusion, and this explains the maximum close to the dielectric surface. It is interesting to note that in our simple chemistry model and if the transport terms in the metastable transport equation are not important, the metastable density is simply given by equation (4.13) of the 0D model. This equation shows that the metastable density depends only on the electron temperature through some rate constants (and is proportional to the gas density). We see on Figure 4.15 and Figure 4.16 that indeed the metastable density distribution follows the electron temperature distribution, with amplification due to the fact that the rates of production and destruction of the metastable state are very non-linear functions of the electron temperature.

The plasma potential in the cavity, displayed in Figure 4.16d has a maximum of about 10.5 V in the region of maximum plasma density. Note that for the large plasma density obtained under these conditions, the electron Debye length is rather small (on the order of 10 μm). The Debye sheath between the plasma and the walls is actually not resolved because the grid spacing used in the 2D model (typically 1 mm) is much larger than the Debye length. In spite of the fact that the model does not resolve the sheath, it provides a good estimation of the plasma potential (because the balance of charged particles fluxes is well described in the model) and of the space variations of the plasma properties in the quasi-neutral plasma (the description of charged particle transport in the quasi-neutral plasma does not require to resolve the electron Debye length).

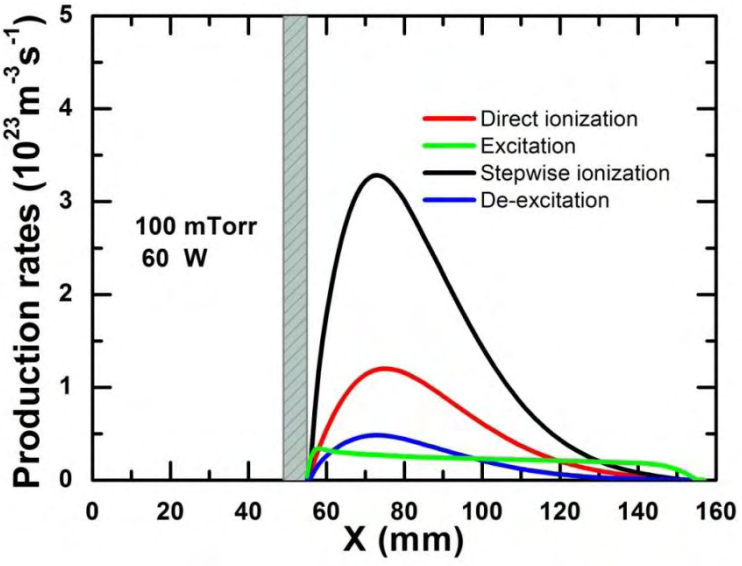

Figure 4.17: Axial variations of the direct ionization, excitation to the metastable state, de-excitation and stepwise ionization

Figure 4.17 shows the variations of the excitation, ionization and de-excitation rates along the discharge axis. We see that, as in the 0D model (see Figure 4.5), most of the ionization comes from stepwise ionization of the metastable states (more than 80% of the ionization is due to stepwise ionization of metastable atoms in both models).

From the 2D calculations we can show the particle balance for each species, i.e. the contributions of the different mechanisms to the production and loss of each species.

Particle→					
Reaction	1 - direct ionization	0.22	0.22	0.00	0.00
	2 – elastic	0.00	0.00	0.00	0.00
	3 – excitation	0.00	0.00	1.00	0.00
	4 – de-excitation	0.00	0.00	-0.15	0.00
	5 – stepwise ioniz.	0.78	0.78	-0.83	0.00
Surface loss		-1.00	-1.00	-0.02	-1.00
Surface production		0.00	0.00	0.00	1.00

Table 6: Particle balance calculated with the 2D model (integrated over the discharge volume) for each species. The relative contribution of each reaction to the production (positive) and loss (negative) for each species in represented in relative unit. The particle generation and losses on the surfaces are also included.

The global (integrated over the volume) particle balance for each species is presented in Table 6 for the conditions considered in this section (60 W, 100 mtorr). As discussed above, this table confirms that stepwise ionization of the metastable is the dominant ionization term since about 80% of the ions and electrons are generated from stepwise ionization, and 20% from direct ionization. These numbers show the importance of taking account of the metastable particles in the calculation. An indirect consequence of the presence of metastable is a lowering of the electron temperature.

In our model, electrons and ions are only lost to the cavity walls (recombination of atomic ions is small and the pressure is not large enough for the production of molecular ions). The metastable atoms are only generated from excitation, and lost mainly in volume collisions by stepwise ionization (83%) and also de-excitation (15%). Only (2%) are lost to the cavity walls, and this confirms that transport effects are not dominant for metastable atoms for this pressure range.

4.3.2 2D results for a typical case with gas flow and heating

The results presented above have been obtained with constant and uniform gas density (pressure and temperature). In this section, we discuss the role of gas flow and gas heating on the model results for the same conditions as above (i.e. 60 W absorbed power, 100 mtorr pressure)..

(a)

(b)

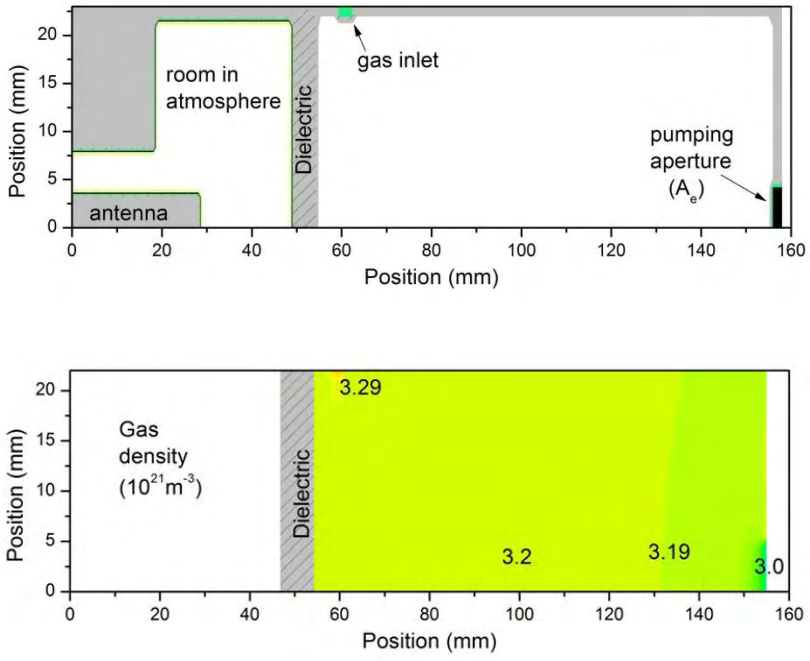

Figure 4.18: Calculation domain (a) and 2D results (b) of the gas density (corresponding to 100 mTorr) distribution from the model with fixed injection flow rate. The aperture radius is 0.4 cm.

In the simulations below the neutral atoms are supposed to be injected from a gas inlet located on the side of the cylinder with a specified flow rate Q_0 (s^{-1}) and pumped through an aperture with an area A_e in the exit plane as shown in Figure 4.18.

The thermal flux of neutral gas that flows out of the cavity across the aperture is defined as:

(4.28) $$\Gamma_g = \frac{1}{4} n_{g0} u_{g0}$$

Where n_{g0} and u_{g0} are the neutral gas density and mean velocity without plasma, $u_{g0} = \left(\frac{8kT_g}{\pi M} \right)^{1/2}$. This definition corresponds to the flux of Maxwellian particles in one direction.

Without plasma, the inlet flux and pumped flux have to be equal:

$$Q_0 = \frac{1}{4} n_{g0} u_{g0} A_e \beta_c$$

Where β_c is a correcting factor to take into account neutral particles that can be partly reflected back into the cavity due to the aperture geometry. Its value ranges from 0 to 1. With perfect aperture, when no particles are reflected, β_c=1. Using the equation of state $p_0 = n_{g0} k T_{g0}$, we obtain a relation between gas pressure, gas temperature and flow rate:

(4.29) $$Q_0 = \frac{u_{g0}}{4kT_{g0}} A_e \beta_c p_0$$

In the experiments of Diamant the flow rate is on the order Q_0=1 mg/s (10.25 sccm). Keeping the same flow rate as in the experiments, and for a gas pressure of 100mtorr, this equation is satisfied if we take the same pumping aperture as Diamant, A_e=5 10^{-5} m^2 (aperture radius 0.4 cm) and adjust the correcting factor (see the definition above) to a value of, β_c=0.46.

Figure 4.18 shows the calculated distribution of neutral gas density using this parameter and without plasma (only Navier Stokes equations are solved). We see on this figure that the gas density is quite uniform inside the cavity and is around 3.2 10^{21} m^{-3} (which corresponds to 100 mTorr at 300 K), except next to the gas inlet and to the pumping aperture.

We now look at the simulation results when the plasma is ON and when gas heating is taken into account i.e. when energy exchange between charged particles and neutral particles is included in the Navier-Stokes and energy equations for the gas.

Gas heating is mainly due to the power deposition in the gas through ion-neutral collisions (this power deposition was neglected in the power balance of the 0D model). Ions are accelerated in the ambipolar field and we assume that the power absorbed by ions in this field is delivered to the gas through collisions (Joule heating). Note that in the overall power balance, electrons are actually cooled by the ambipolar field since they lose energy by diffusing against this field. In other word part of the electron energy is used to create the ambipolar field, which in turn accelerated ions toward the walls. The energy gain by ions in the ambipolar field is lost through collisions. We will quantify below the fractional power transferred into gas heating.

The walls play an important role in the overall energy balance. In the following we assume that the metallic walls are perfectly cooled (temperature is fixed at 300 K at the surface), and we consider two cases for the dielectric wall: cooled dielectric (i.e. temperature imposed on the dielectric surface, and equal to 300 K) or uncooled dielectric (zero thermal flux). A zero thermal flux is also assumed at the pumping aperture. These two different boundary conditions are used to provide upper and lower limits of the gas temperature (assuming that the metal walls of the source stay cold).

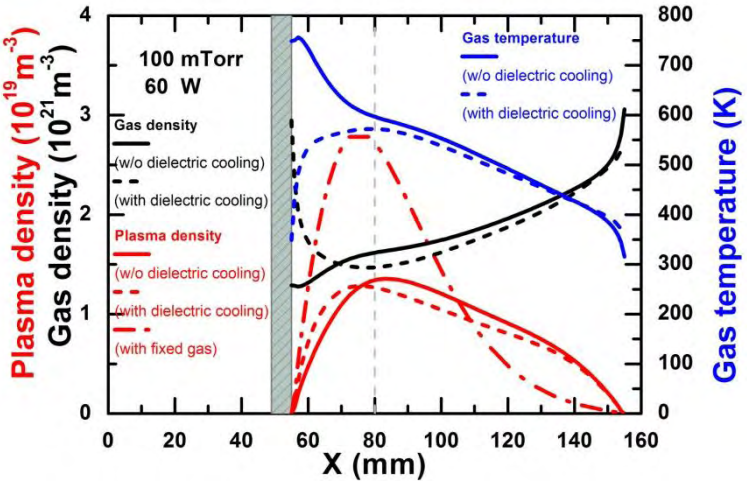

Figure 4.19: Plasma (red lines) and gas (black lines) density, and gas temperature (blue lines) variations along the discharge axis from the plasma model at 100 mtorr and for a 60 W input power, solid lines correspond to uncooled dielectric (zero thermal flux to the dielectric wall), whereas dashed lines correspond to a cooled dielectric (dielectric temperature fixed to 300 K).The dash-dot line corresponds to the case without gas flow and without gas heating (previous section).

Figure 4.19 displays the axial profiles of the gas temperature, gas density, and plasma density calculated with the two different boundary conditions on the dielectric surface for the gas temperature. The gas temperature reaches 700 K next to the dielectric surface when the dielectric is not cooled and about 600 K when the dielectric temperature is kept at 300 K. The gas density varies as expected inversely to the gas

temperature, and is significantly lower next to the dielectric surface.

We also see on Figure 4.19 that the plasma density is not strongly affected by the boundary conditions of the gas temperature on the dielectric surface. In the rest of this thesis we will assume that the dielectric is not cooled and that the thermal flux at the dielectric surface is zero. This assumption on the boundary conditions for the gas temperature on the dielectric wall will therefore give an upper limit of the effect of gas temperature (assuming that the metallic walls temperature is maintained at 300K).

More details on the effect of gas heating on the plasma properties can be seen on the 2D plots of Figure 4.20 where the gas temperature, density, plasma density, electron temperature, metastable density and plasma potential are represented (Figure 4.20(a), (b), (c), (d), (e), (f), (g), respectively). The gas density is reduced by about 50% at the location of maximum gas temperature (as expected, since the maximum gas temperature is 600 K).

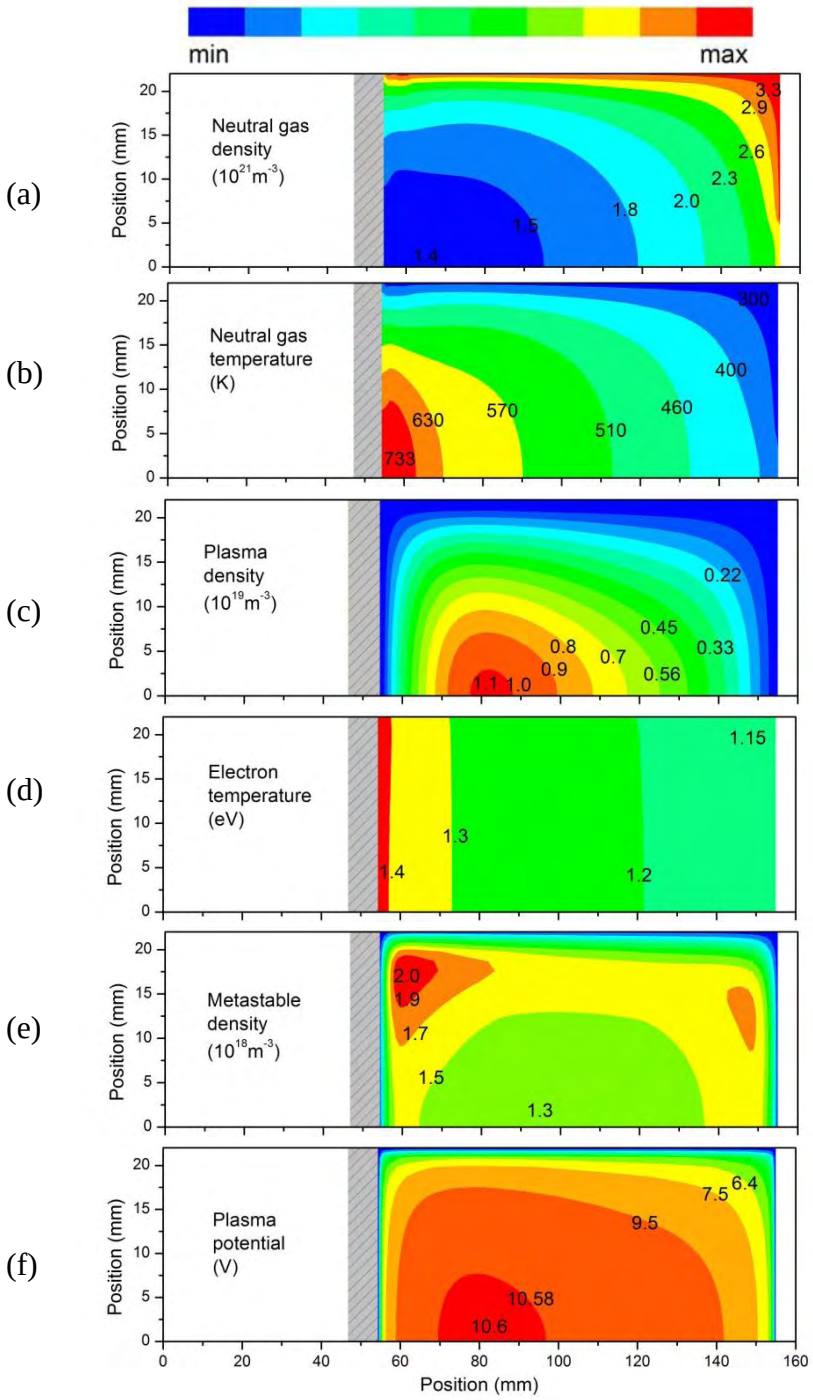

Figure 4.20: (a) gas temperature distribution, (b) gas density distribution, (c) Plasma density distribution, (d) electron temperature distribution, (e) Metastable density distribution, (f) plasma potential distribution, from the 2D model with fixed injection flow rate.

The plasma density maximum (see Figure 4.19 and Figure 4.20(c)) is about twice smaller than in the case without gas heating. This is because the decrease of the gas density (and subsequent decrease of metastable density) due to the larger gas temperature (phenomenon known as neutral depletion in the literature [9]-[11]) leads

to an increase of the electron temperature (as can be clearly seen the 0D particle balance equation: a larger ionization rate is needed to balance the losses to the wall, if the gas density is decreased; this leads to an increase of the electron temperature). The increase in electron temperature (although relatively small, compare Figure 4.20(e) and Figure 4.16(b)) leads to an increase in the energy losses to the walls and in the volume. Roughly speaking, a decrease of the gas density by a factor of 2 must be compensated by an increase of the ionization rate by a factor of 2, to balance the losses to the walls. The increase of the ionization rate by a factor of 2 leads to an increase of the volume electron energy loss rate by a factor on the same order. Therefore, from the power balance equation, the plasma density must decrease by a similar factor).

It is interesting to look at the space and the total power distribution which is dissipated by ions in gas heating. This power density is equal to the power gain per unit volume associated with ions drifting in the ambipolar field and is equal to ($J_i.E_{amp}$) where J_i is the ion current density. Figure 4.21 shows the distribution of the power density deposited into gas heating by ions in the discharge volume. The power density is on the order of 2 10^4 W/m^3 in the bulk plasma, leading to a total power on the order of 2 W (the discharge volume is around 10^{-4} m^3). The exact value obtained by integration over the volume is 2.3 W. This value is a relatively small fraction of the total power absorbed in the discharge in these conditions (60 W).

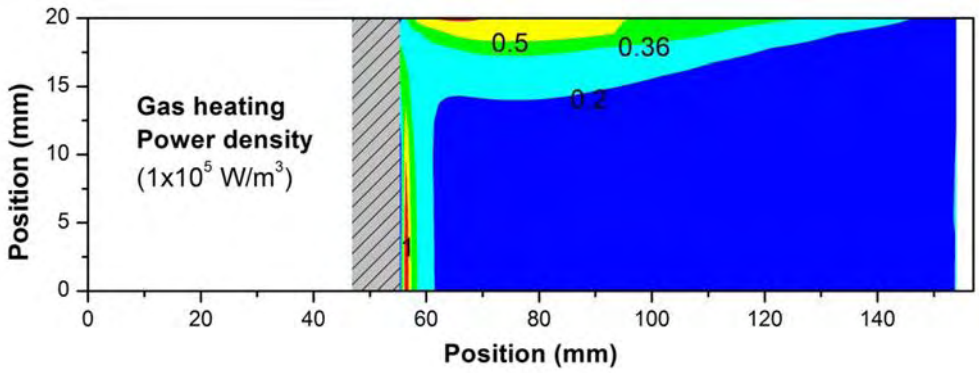

Figure 4.21: Power density dissipated in gas heating by ions at 60 W, 100 mtorr.

The spatial gradient of the plasma density is also significantly affected when gas heating is taken into account. This appears in Figure 4.22 where the axial profiles of plasma density and metastable densities for the cases without and with gas heating are compared (in relative units). The gradients are less important (the profiles are "more flat") when gas heating is included. This can be easily understood in terms of an increase of the particle diffusion coefficients when the gas density decreases.

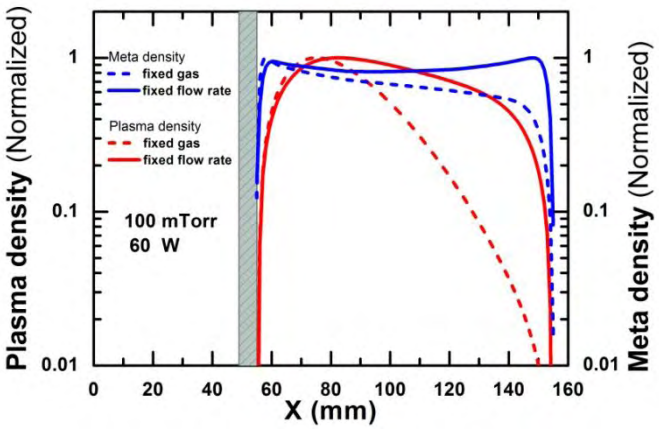

Figure 4.22: Plasma and Metastable density distribution in 1D from CAVIMO code at 60 W input power, solid lines are with fixed gas, dashed lines are with fixed injection flow rate.

Coming back to Figure 4.20 we note (Figure 4.20(f)) that the metastable density presents maximum values in the corners of the cavity, which was not the case when heating was not included (maximum on axis, see Figure 4.16(c) for comparison). This can be simply explained by the fact that the gas density increases radially from the axis to the side walls. The electron temperature being approximately uniform radially because of the good electron thermal conductivity, the production rate of the metastable atoms is therefore larger in the corners.

Finally the plasma potential distribution in the case with gas heating, Figure 4.20(g) is not significantly different (slightly larger) than in the case without gas heating, Figure 4.16(d).

It is interesting to look at the contribution of the different particle to the total pressure in the cavity. The total pressure can be written as:

(4.30) $$p = n_e T_e + n_i T_i + n_g T_g$$

Ion and metastable temperatures are the same as the gas temperature, and since their density is much smaller than the gas density, their contribution to the total pressure is negligible. The total pressure can be therefore approximated by:

(4.31) $$p \approx n_e + n_g T_g$$

In the region of maximum plasma density, the electron density is on the order of 10^{19} m^{-3} and the electron temperature around 1 eV , therefore the electron pressure is about 10 mtorr (the electron pressure decreases toward the walls). Since the total pressure (100 mtorr) is practically constant over the volume, the gas pressure is lower in the volume than near the walls. In other words the electron pressure “pushes the neutral gas” toward the wall. The electron pressure contributes to the depletion of the neutral gas in the discharge volume, although the dominant effect is due to gas heating.

4.3.3 Conclusion

We can summarize this section as follows:

- The detailed description of the plasma-Maxwell coupling is not essential for our problem (this was not obvious *a priori*). The power is absorbed by electrons in a small plasma layer (skin depth) below the quartz plate. The skin depth is small with respect to the plasma dimension. Simulations show that the results are not very sensitive to the exact profile of the power deposition and we concluded that it is possible to use the plasma model only (without solving Maxwell's equations) and to assume that the power is absorbed in a thin layer (we take 1 mm in all the calculations) at the plasma edge below the quartz plate. This is an important conclusion since solving Maxwell's equations coupled with the plasma equations can be quite cumbersome.
- The 0D model provides estimations of the main parameters (plasma density, metastable densities, electron temperature) that are in rather good agreement with the 2D results (in the case where gas heating is neglected).
- Both 0D et 2D models show that under the considered conditions, the contribution of the metastable states to the ionization is dominant (about three times larger than the contribution of direction ionization). A direct consequence of this is that the electron temperature can remain quite low in the plasma volume, on the order of 1 eV.
- The 2D model shows that the plasma density maximum is not in the discharge center but is closer to the dielectric surface. This is because the power deposition is close to the dielectric surface. At the considered pressure, the electron thermal conductivity is however still good and the electron temperature is around 1 eV in the whole volume. A slightly larger electron temperature next to the dielectric surface, associated with a very non-linear dependence of the reaction rates with electron temperature induces the observed non uniformity of the plasma. The metastable density presents a stronger non-uniformity than the plasma density.
- Gas heating for the considered conditions of 60 W and 100 mtorr is relatively important and lead to gas temperatures between 450 and 600 K. This has some significant consequences on the plasma density and distribution.

4.4 2D parametric study

In this section we first perform a parametric study of the plasma properties as a function of power and pressure (section 4.4.1). We then discuss the influence of the gas flow rate on the results (section 4.4.2). Finally we study the influence of the

parameters on the plasma density profiles (section 4.4.3) and compare the model results with the experimental results of Diamant (section 4.4.4). In all the calculations presented in this section, gas heating is taken into account (with the boundary conditions indicated above).

4.4.1 Influence of pressure and power

Figure 4.23 show the volume averaged plasma density, gas density, and electron temperature as a function of power and for different pressure.

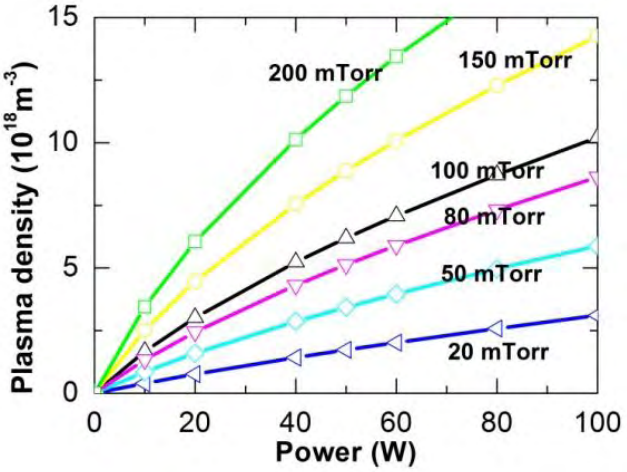

(a)

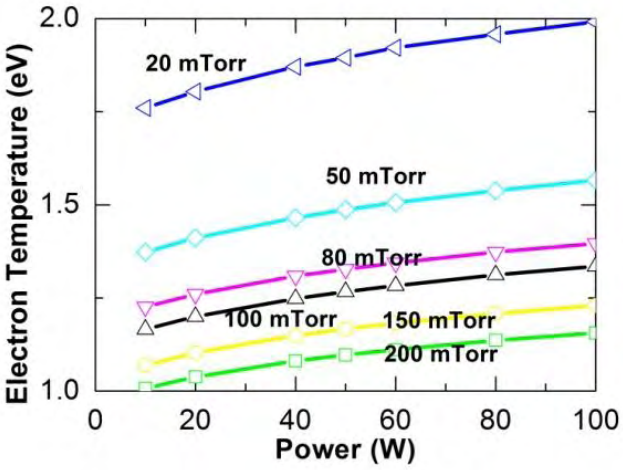

(b)

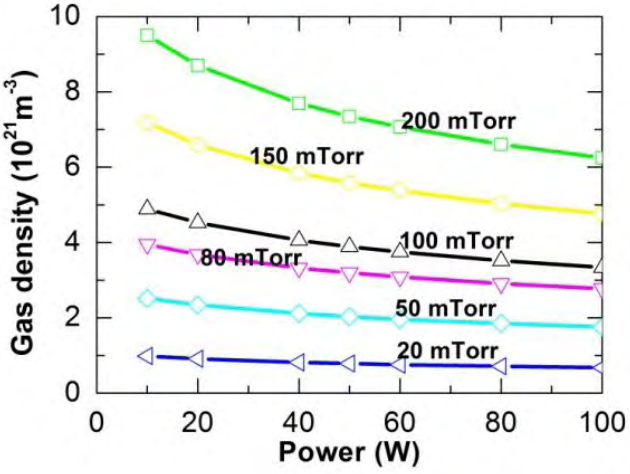

(c)

Figure 4.23: (a), Averaged plasma density, (b),electron temperature, and, (c), gas density as a function of input power (10 to 100 W) for different gas pressures (20 mTorr to 200 mTorr). Note that the gas pressure is fixed before the plasma is turned on.

From the particle and power balance of the 0D model, we can draw the following

simple (approximate) scaling laws: 1), for a given gas density the electron temperature only depends on the gas density and on the effective dimension of the reactor (not on the power), 2) for a given gas density (and thus electron temperature), the plasma density increases linearly with power. These very simple scaling laws may be modified because of transport effects and non-uniformities and also because of gas heating (which modifies the gas density).

Looking at the 2D averaged numerical results of Figure 4.23, we see that the simple scaling laws are not valid, but we recognize the trends given by the scaling laws. The electron temperature of Figure 4.25b decreases when pressure increases, for a given power, as expected since the ionization increases with gas density. The electron temperature for a given pressure is not constant as a function of power as stated by the simple scaling laws, but increases slightly with power. This is because the gas density decreases with increasing power, due to the gas heating effect. Note that the gas flow can play an important role here. In the case with gas heating and no gas flow (i.e. no gas injection nor pumping), the gas density may decrease locally but the volume averaged density must remain constant (i.e. the gas density decreases in the volume center but must increase near the walls). In the case with gas heating and gas flow, which is considered in Figure 4.23, the situation is more complicated and the results show that the volume averaged gas density decreases because of gas heating (for a constant flow rate). This point is discussed in the next section.

Finally, we can deduce from the 2D model the total electron and ion currents to the walls. As mentioned above in the description of the 0D model results, these currents give an upper limit of the electron current that can be extracted when the source is used as an electron source.

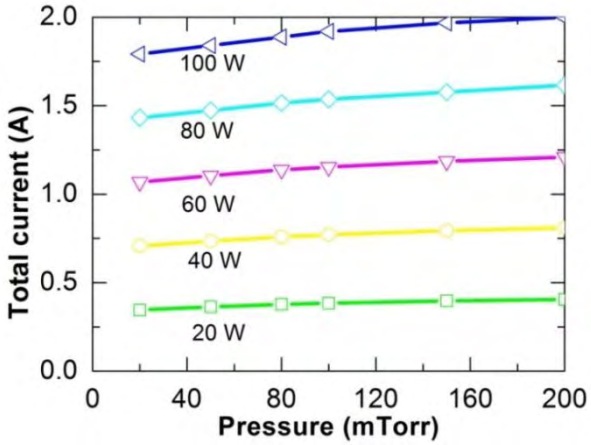

Figure 4.24: Total electron current to the walls as a function of pressure and for different values of the applied power, from the 2D model with gas heating and gas flow included.

The total electron current to the walls is shown in Figure 4.24 as a function of power and pressure. We see that the values of the electron current are close to those from the

0D global model represented in Figure 4.10. The trends with increasing pressure are slightly different from the 0D model due to the effect of gas heating.

4.4.2 Influence of the flow rate

We come back here to the question of the influence of the gas flow rate on the results. As mentioned in the previous section, in the absence of gas flow, gas heating may lead to a decrease of the gas density in the volume of the cavity, but this must be balanced by an increase of the gas density near the walls since the volume averaged gas density must stay the same (no in or out flow).

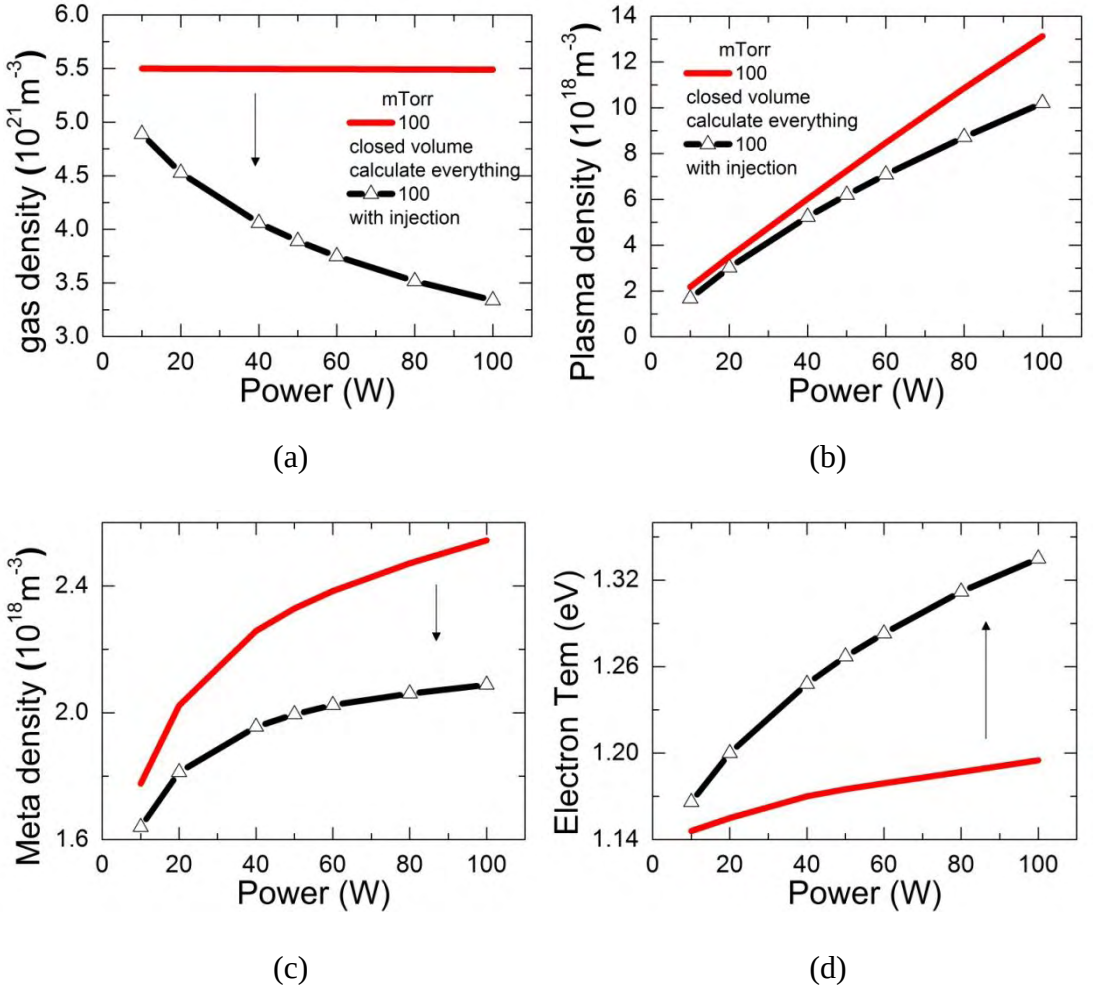

Figure 4.25: Results of the discharge in a closed volume (red lines) and the discharge with injection and pumping (black lines) under 100 mTorr gas pressure. (a)Gas density, (b)ion density, (c)Metastable density and (d)electron temperature as a function of power.

This is illustrated in Figure 4.25 which compares the cases with and without gas injection and pumping and with gas heating, for an initial gas pressure of 100 mtorr and a varying absorbed power of 60 W. Figure 4.25(a) shows the volume-averaged

gas density in the chamber. We see that in the case of a closed volume (red line), the averaged is constant because only the space distribution of the neutral atoms is affected by gas heating and the number of xenon atoms in the chamber is practically constant (and is negligibly affected by ionization). The black line of Figure 4.25(a) shows that when injection and pumping is taken into account, the averaged gas density, for a given flow rate giving a pressure of 100 mtorr before the plasma is turned ON, decreases significantly with power. In turn, the decrease of the gas density must be balanced by an increase of the ionization rate, leading, as expected to an increase of the electron temperature, as seen in Figure 4.25(d). The plasma density Figure 4.25b) and metastable atoms density (Figure 4.25(c)) decrease when because of the decrease of the gas density.

4.4.3 Plasma density profile

In the next section, we compare the model results with experimental measurements of the plasma properties performed by Diamant [12] using Langmuir probes. These measurements include measurements of the plasma density axial profile and it is therefore useful to understand what are the parameters controlling this profile in the model.

(a)

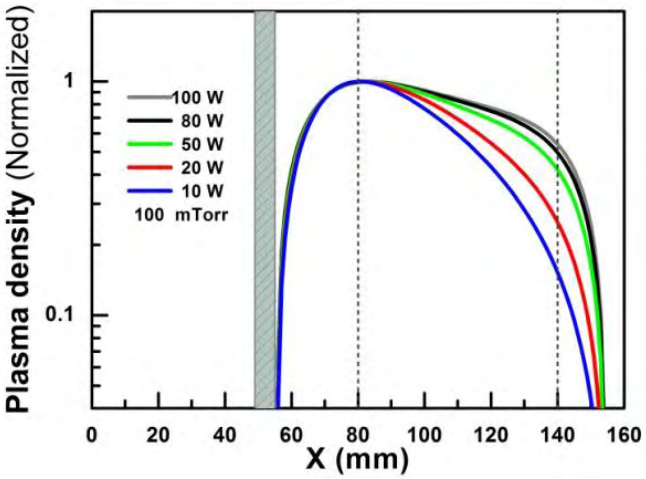

(b)

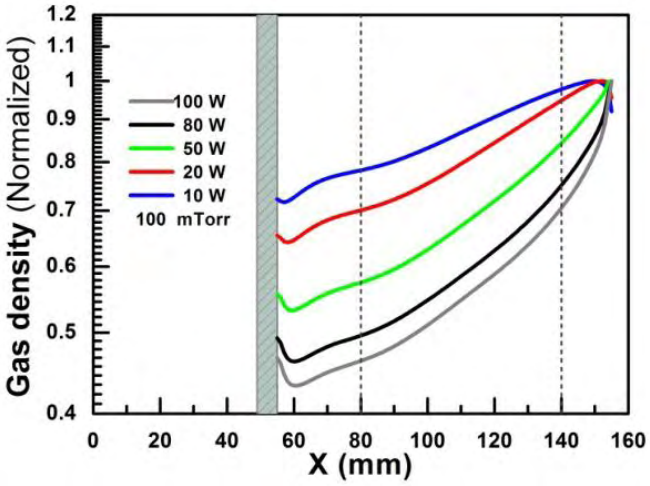

(c)

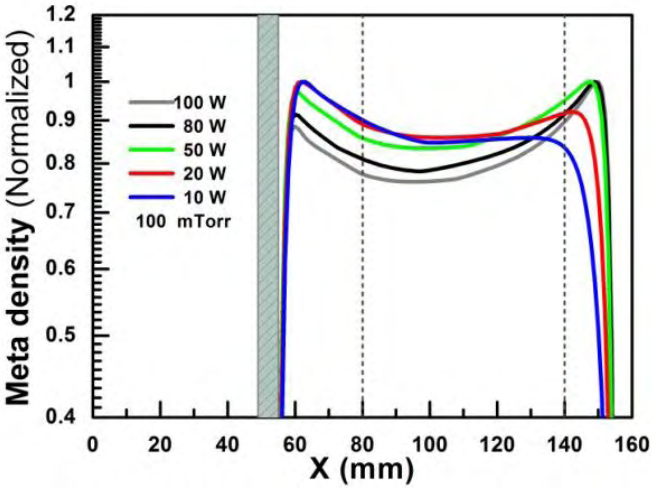

Figure 4.26: Normalized axial profiles at 100 mtorr and for different values of the applied power of (a) plasma density, (b), gas density , and (c), metastable density.

Figure 4.26(a) shows that the value of the applied power significantly affects the axial plasma density profile. This can be explained by the fact that the gas density decreases more next to the quartz plate (where the gas temperature is higher), as seen

in Figure 4.26(b) (see also Figure 4.20(b)). Ionization is therefore larger on the right side of the chamber. The distribution of metastable atoms is also larger on the right side, because the gas density is larger, and this in turn enhances the ionization in the this region.

We can therefore conclude that the flatter plasma density profile observed when the power increases is due to the fact that the gas temperature is larger (gas density is lower) on the left side of the chamber, next to the quartz plate. Not however that this is the results of our assumptions on the boundary conditions for the gas temperature equation, i.e., ambient temperature of the metallic walls (supposed to be cooled), and no heat flux to the dielectric surface.

The maximum plasma density increases with pressure as seen in Figure 4.23, but the results show that the plasma density profile is not strongly affected by changes in the pressure in the considered range.

4.4.4 Comparisons with experiments

Figure 4.27 and Figure 4.29 show comparisons between results from our simulations and the experimental measurements of Diamant.

Figure 4.27 shows the simulation results and the measurements of Diamant for a discharge at 60 W, 100 mtorr. Several experimental results are shown on this figure. Some of them have been performed with the electron extraction system ON, i.e. with applied potential applied on a keeper or on an anode outside the chamber beyond the aperture. Some measurements have also been performed without extracting voltage, i.e. under conditions similar to the simulations in the present chapter (the question of electron extraction is treated with the 2D model in the next chapter). These measurements are represented in red (symbols) on the figures and can be compared with the simulation results. We see that the measurements and model results for the electron temperature (Figure 4.27(b)), and plasma potential (Figure 4.27(d)) distributions along axis are in rather good agreement but that the plasma density profiles are not. The maximum value of the plasma density in the experiments and simulations are however relatively close to each other, on the order of 10^{19} m^{-3}.

(a)

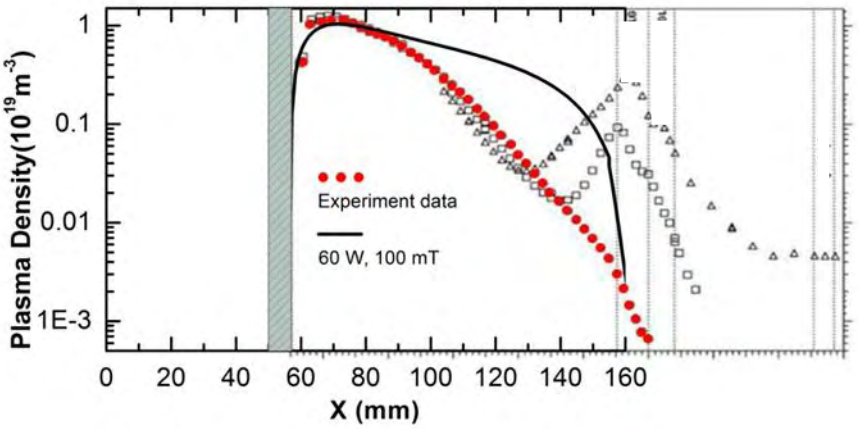

(b)

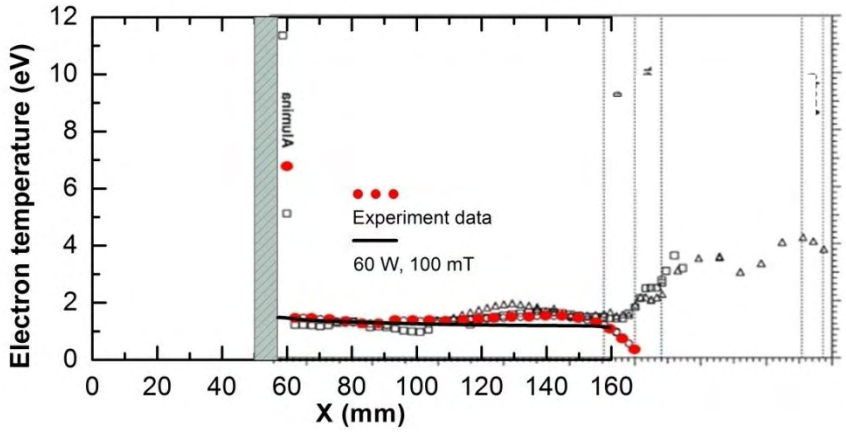

(c)

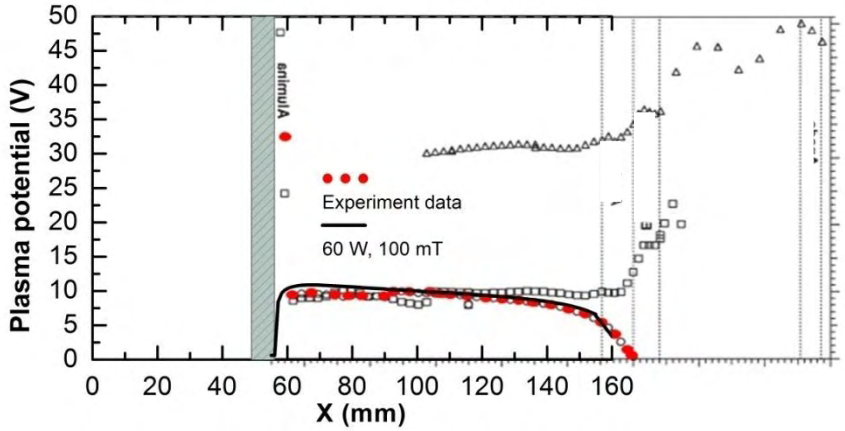

Figure 4.27: Comparisons of the measured (red symbols) and simulated (red line) axial profiles of (a) plasma density, (b), electron temperature, and (c), plasma potential at 100 mtorr, 60 W. The black symbols correspond to experimental results when an electron extraction voltage is applied beyond the aperture on the right wall of the chamber.

The calculated plasma density profile in Figure 4.27a is much flatter than in the experiments. The discussion of section 4.4.3 can be used to understand this result. We

have seen in this section that when the power is increased, the gas temperature tends to increase more next to the quartz plate since we assume that it is not cooled whereas the metallic walls are supposed to stay at room temperature. Therefore the gas density is lower on the left part of the plasma source, next to the quartz plate. The ionization source term, which is proportional to the gas density, is therefore larger on the right part of the source. This effect increases with power since gas heating increases with power. This effect is clearly seen in Figure 4.28, which shows the plasma density profiles on axis calculated at 60 W, 100 mtorr with and without taking into account gas heating. We see that the plasma density profile is much flatter when gas heating is included, because of the depletion of the gas density next to the quartz plate, as described above. The results with and without metastable atoms included are also displayed on Figure 4.28 and show that the presence or not of metastable atoms does not affect much the profile. Since the metastable density is proportional to the gas density, the presence of metastable atoms increases the ionization rate proportionally to direction ionization; therefore the possible change in plasma density profile due to metastable atoms occurs only through a possible change of the electron temperature when metastable atoms are present.

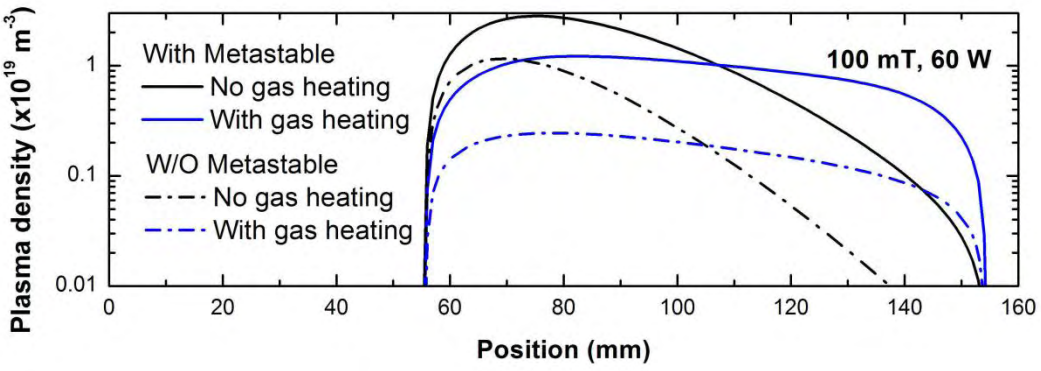

Figure 4.28: Calculated plasma density profiles along the discharge axis at 100 mtorr and for 60 W power, with and without including gas heating and with or without including the presence of metastable atoms.

On can deduce from Figure 4.28 that the calculated plasma density profile is closer to the experimental one when the spatial variations of the gas density due to gas heating are not taken into account in the model, or equivalently, if the absorbed power is lower (less gas heating). Another parameter than can affect the plasma density profile is the gas pressure. The increase of the gas pressure tends to make ionization more local (decrease of electron thermal diffusion) and therefore to increase ionization near the quartz plate. This is turn tends to increase the plasma density on the left part of the chamber. This is illustrated on Figure 4.29, which shows that a good match between measured and calculated plasma density profiles can be obtained when the pressure is increased and the absorbed power is decreased in the calculations.

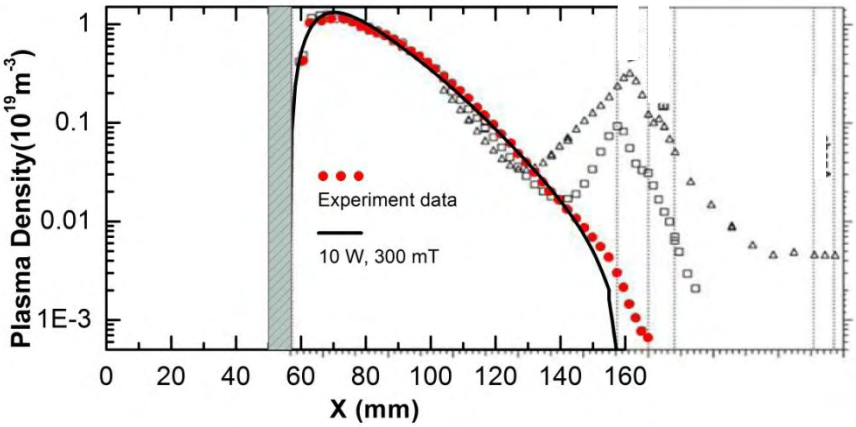

Figure 4.29: Measured density profile at 60 W, 100 mtorr, compared with calculated profile at 10 W, 300 mtorr (see text).

It is difficult to draw clear conclusions from the above comparisons. The good agreement between measured and calculated electron temperature and plasma potential and between the maximum value of the plasma density tends to give us some confidence in the ability of the model to predict or reproduce the experiments. However the difference in the measured and calculated plasma density profile is intriguing. The results show that the plasma density profile is very dependent on the gas temperature and gas density in the source and this may be the source of the discrepancy. It seems from the comparisons that the gas density and gas temperature in the experiments are more uniform than in the model. This could be due to the boundary conditions used in the simulations, and to the fact that the metallic walls are not perfectly cooled in the experiments.

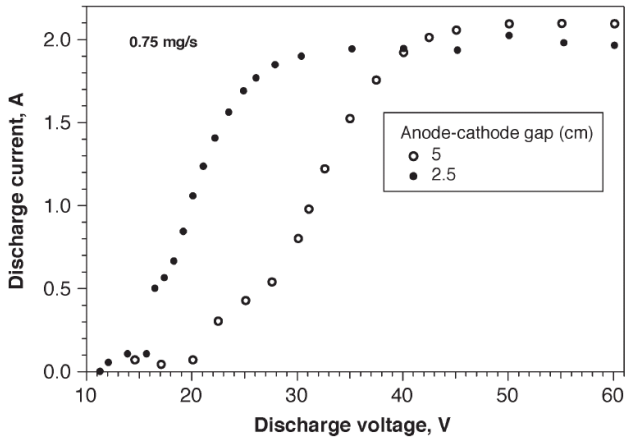

Figure 4.30: Measured extracted electron current as a function of bias voltage (60 W, 100 mtorr) for two different configurations of the extracting electrode [12].

Finally we note that the measured maximum extracted electron current on the order of 2A, see Figure 4.30) is larger than the calculated one (about 1.2 A, see Figure 4.24).

This is a significant difference since the extracted current for a given power is directly related to the energy lost per electron-ion pair generated in the discharge. On the other hand the 0D and 2D models give very similar values of the extracted current for a given power, which tends to show that this parameter depends mainly on the xenon chemistry. A possible reason for the lower calculated current can be that our model underestimates the metastable density. An increase of the metastable density by a factor of 2 would give a calculated current in better agreement with the experiment.

4.4.5 Influence of pumping aperture

In the calculations reported above we did not describe in details the region around the pumping aperture since pumping was simply described by a boundary conditions on a circular aperture of radius 4 mm on the right wall of the plasma source. In this section we consider a more realistic case where the pumping region behind the aperture is also taken into account. This may be important for the simulation of the electron source since electrons are extracted from the source through the pumping aperture.

In section 4.3.2 above the equality between the inlet flux and the pumped flux was written as:

$$Q_0 = \frac{u_{g0}}{4kT_{g0}} A_e \beta_c p_0 \qquad (4.32)$$

Where u_{g0}, T_{g0} , and p_0 are the gas thermal velocity, gas temperature and pressure without plasma, A_e is the area of the pumping aperture and β_c a parameter accounting for back diffusion of atoms from the pumping region into the source. β_c is sometimes written as β_c=1- η_c where η_c is a reflection coefficient called the Clausing factor [13] related to a conductance into the cavity from the vacuum system. This coefficient depends on the aperture's length-to-diameter ratio and can be calculated with Monte Carlo simulations [14]-[15].

For the source of Diamant, the length-to-diameter ratio of the aperture, $L_e/D_e \approx 1.25$, which gives a Clausing factor around [illegible]. Consequently the desired pressure p_0 of 100 mTorr at 300 K background temperature can be obtain with an injection flow rate [illegible] of 7.3 10^{18} particles.s^{-1} (≈1.5 mg.s^{-1}), through equation (4.32) above. This value is a little higher than the injection flow rate reported by Diamant (1 mg.s^{-1}). This may be due to the fact that than an anode is present in the expansion region behind the aperture in the experiment which may increase the number of atoms flowing back to the source.

Figure 4.31 shows the gas density distribution obtained from the Navier Stokes part of the model when an expansion region beyond the aperture is included in the model (without plasma).

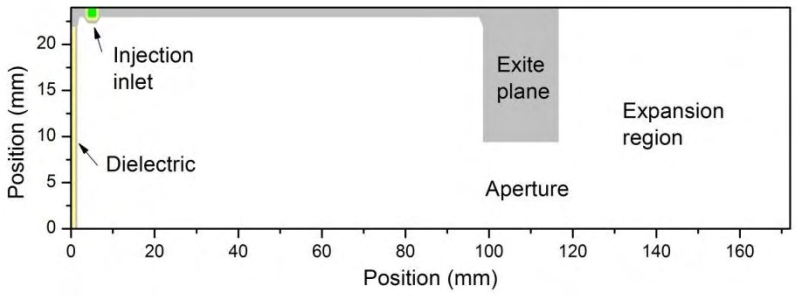

(a)

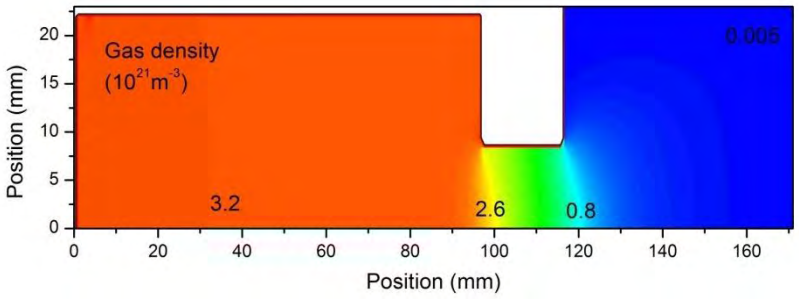

(b)

Figure 4.31: (a) Simulation domain including an expansion region beyond the aperture, and (b) calculated 2D distribution of the gas density (without plasma) in this configuration with a mass flow rate adjusted to obtain a gas pressure of 100 mtorr.

Results from the complete simulation of the source in the domain of Figure 4.31a (including the expansion region) with gas heating and pumping are shown in Figure 4.32. We see that the plasma density decreases very quickly through the aperture. The description of the real aperture and region beyond the aperture in the simulations does not change significantly the results presented in the section above as we can see on the comparisons of the axial profiles of the different plasma properties shown in Figure 4.33

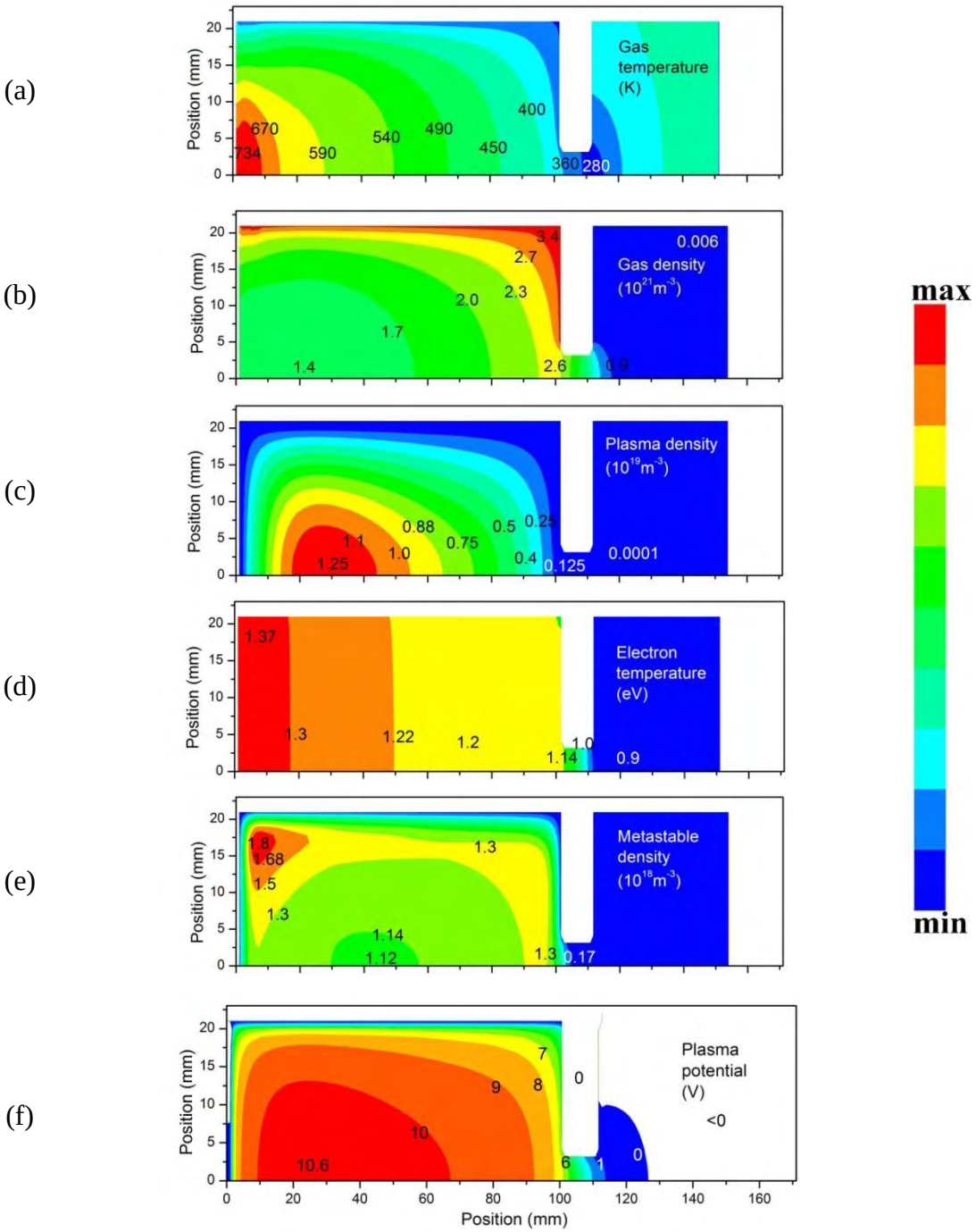

Figure 4.32: Plasma properties calculated when the expansion region beyond the pumping aperture is included in the simulations (60 W, 100 mtorr); (a) gas temperature, (b) gas density, (c) plasma density, (d) electron temperature, (e) metastable density, (f) plasma potential.

(a)

(b)

(c)

(d)

(e)

(f)

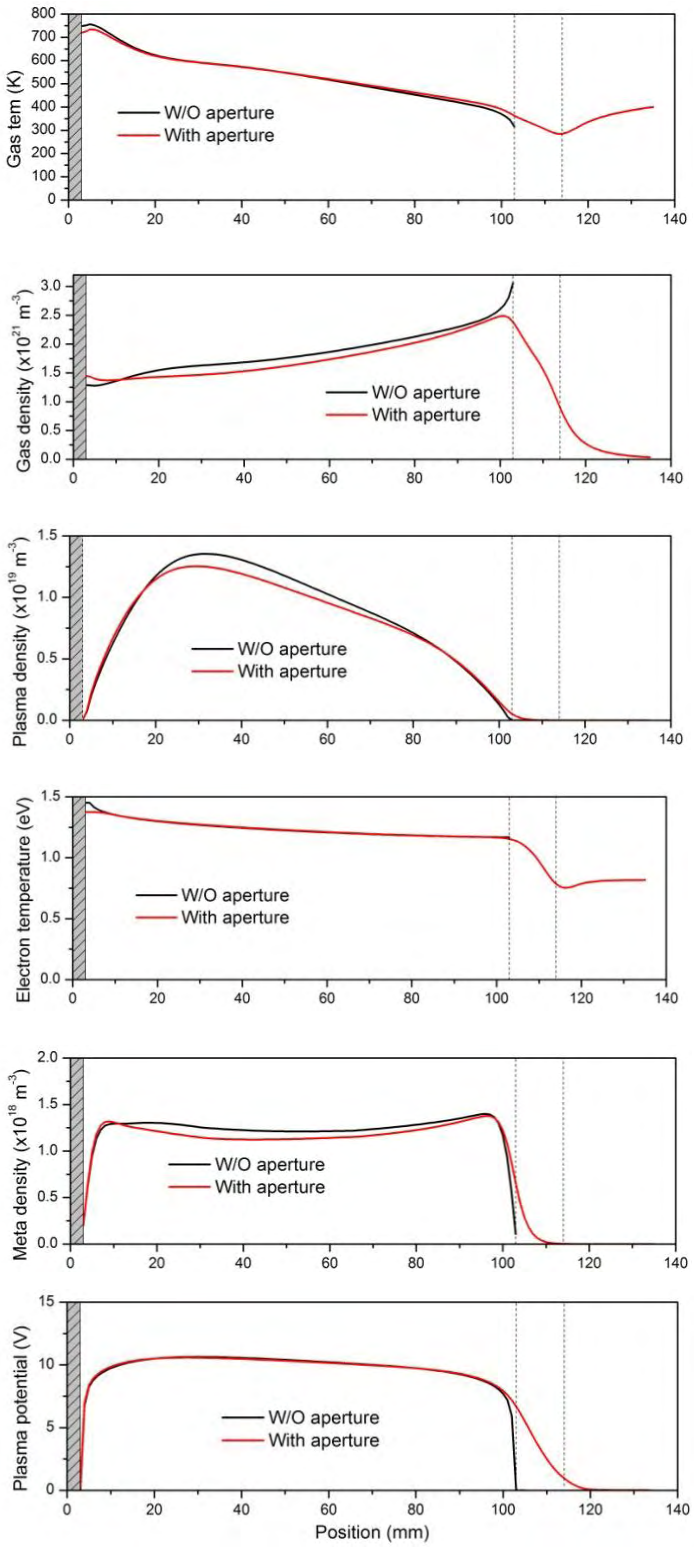

Figure 4.33: Axial profiles of the different plasma properties calculated with the complete aperture in the simulations (same as in Figure 4.32) compared with those obtained with a simple hole and using the back diffusion parameter β_c, as in the results presented in the sections above.

4.5 Conclusion

In this chapter we have studied the microwave source in the conditions of the experiments of Diamant, without considering the question of electron extraction (this is the subject of the next chapter).

Global model

Before looking at the results from 2D simulations of the source, we first presented the simplified plasma chemistry scheme used for xenon in this thesis. We then described the principles of a global, 0D model of the source. This model is based on global equations for the particle and energy balance: ionization (direct and stepwise) must balance the losses to the walls, and the power lost by particle flowing to the walls and by collisions in the volume must be equal to the power absorbed by the electrons. A global model can be accurate if the electron temperature does not vary significantly in the discharge volume. This is the case in our conditions (pressure on the order or below 0.1 torr and dimensions of a few cm). However, although the electron mean free path for energy exchange is sufficiently large in these conditions to ensure an almost constant electron temperature, the electron mean free path for elastic collisions (in the cm range) and the ion mean free path (fraction of a mm) are sufficiently small for the transport to be controlled by collisions and ambipolar diffusion. In these conditions, the charged particle densities can be classically estimated by some Bessel-cosine profiles and the charged particle balance equation provides a relation between ionization frequency, ambipolar diffusion coefficient, and dimensions of the discharge vessel (classical eigenvalue problem for ambipolar diffusion). The electron temperature is deduced from this equation. Knowing the electron temperature, the charged particle losses to the walls and by collisions in the volume can be estimated. Equating the energy loss per unit time to the absorbed power, the plasma density is deduced (and varies linearly with power for a given electron temperature and gas density).

Using the 0D model, we have shown that the electron temperature in the conditions of Diamant is on the order of 1 eV. Actually, according to the model, the electron temperature stays around 1 eV in a relatively large range of pressure: 20 mtorr to 200 mtorr, and tends to increase rapidly below 20 mtorr. An important conclusion from the 0D model is that the average energy loss (including collision losses and energy losses to the wall) per electron-ion pair generated in the volume is on the order 50 eV in our conditions. This number is relatively constant in the range of pressure (20 to 200 mtorr) and power (10 to 100 W; this parameter is in principles independent of power since it is depends only on electron temperature) that we have explored. From this number we can deduce the maximum electron current that can be extracted from a plasma source in these conditions: the total energy cost E_T= 50 eV per electron-ion pair corresponds to a maximum current per unit power $I/P=1/E_T$, i.e. 20 mA/W. In

other words, according to the 0D model, the maximum current that can be extracted from the plasma for an absorbed power of e.g. 60 W would be 1.2 A. At 60 W and 100 mtorr, which are typical of the experiments of Diamant [12],[16]-[18], the 0D model predicts an average plasma density on the order of 10^{19} m^{-3}. The model also shows that stepwise ionization of the metastable xenon atoms plays a very important role in the particle and energy balance (the energy cost per electron-ion pair would be much larger without metastable ionization, and the maximum extracted current per unit power at 100 mtorr would be two to three times smaller).

2D model

The global model can give reasonable estimates if the electron temperature and gas density are uniform in the plasma volume. The electron temperature is not necessarily uniform. One reason of non-uniform electron temperature could be the very non-uniform electron heating in a microwave plasma (electrons are heated in a very thin skin at the plasma edge). The gas density may also be non-uniform because of gas heating and gas flow and pumping. The 2D model is very useful to check these effects and can provide very detailed information on the transport of particles and energy in the discharge chamber. We have therefore performed a number of simulations in the conditions of Diamant's experiment.

The first simulations were done assuming no gas heating and no gas flow. We found that in these conditions the 2D model results were quite close to those of the 0D model. The electron temperature given by the 2D simulations is not perfectly uniform in the discharge volume and presents a relative maximum (of about 10%) next to the quartz surface, i.e. in the region of microwave power absorption. This small non-uniformity of the temperature actually leads to a more important non-uniformity of the ionization and excitation rates, which vary exponentially with electron temperature. The charged particle production rate is therefore not uniform in the volume, and the plasma density profile is larger on the left part of the chamber next to the quartz plate (the global model would predict a Bessel-cosine distribution with maximum plasma density in the center of the plasma source). Globally, the calculated plasma density and energy cost per electron-ion pair generated are very similar to those of the 0D model. The 2D results obtained with full Maxwell-plasma coupling show that the microwave power is absorbed in a thin region of about 1 mm thickness next to the quartz plat where the microwave power is injected. This is consistent with a skin depth of about 1 mm for the plasma density of a few 10^{19} m^{-3} given by the simulation. Note that the maximum plasma density is about ten times larger than the critical density in our conditions. We also noted that practically identical results were obtained with the 2D simulations when Maxwell's equation were not solved together with the plasma equation, but just assuming a given power absorbed uniformly in a thin layer of 1 mm at the plasma edge. Moreover, we also noted that the results were not very sensitive to the exact thickness of the region of absorption (between 1 and a few mm). We therefore decided to simply assume uniform power absorption in a 1

mm layer at the plasma edge next to the quartz plate, in the rest of this work.

We then performed 2D simulations taking into account gas flow and pumping and gas heating by the discharge (Navier Stokes equations). The results show that in the case of a 60 W power at 200 mtorr, the gas temperature can increase by more than 300 K next to the quartz plate (assuming no cooling of the quartz plate and a fixed, ambient temperature of the metallic walls). This on uniform increase of the gas temperature leads to a non-uniform distribution of the gas density. The gas density tends to be lower next to the microwave power injection side. The drop in the gas density leads to a decrease of the ionization source term in this region. This tends to balance the effect of a larger electron temperature (and ionization rate) next to the power injection and the global consequence is that the predicted plasma density is actually more uniform when gas heating is included.

Comparisons with the available experimental results of Diamant have been performed. They show a global rather good agreement on the values of the maximum plasma density and on the electron temperature and plasma potential. However the model does not reproduce well the profile of the measured plasma density along the discharge axis. The calculated profile is more “flat” i.e. the density gradient is lower in the calculations that in the experiments (the experimental profile corresponds to calculated profiles when the injected power is lower, i.e. when the non-uniformity of the gas density due to gas heating is less important). Another important discrepancy between model and experiment is the extracted current. The extracted electron current in Diamant’s experiments is 2A at 60 W, 100 mtorr, while it is only 1.2 A in the simulations. The experimental value corresponds to an energy loss of only 30 eV per electron-ion pair generated in the plasma (against 50 eV in the model). This large difference in the energy cost if difficult to understand since the measured and calculated electron temperatures are very similar. Moreover, the calculated energy cost is very close to the energy cost in other electron sources (RF inductive) operating in similar conditions of pressure (see the last section of chapter 2).

Finally all the 2D simulations in this chapter have been performed without a complete description of the pumping aperture and region beyond the aperture (only a circular aperture was considered, with proper boundary conditions to take into account back diffusion of pumped atoms). The model shows that the results are not significantly modified when a real pumping aperture is considered.

4.6References

[1] Meunier, J., P. Belenguer, et al. Numerical model of an ac plasma display panel cell in neon-xenon mixtures. *Journal of Applied Physics*. 78(2): 731-745 (1995)

[2] Pitchford, L. C., J. Kang, et al. Calculated characteristics of radio-frequency plasma display panel cells including the influence of xenon metastables. *Journal of Applied Physics*. 92(12): 6990-6997 (2002)

[3] Sommerer, T. J. Model of a weakly ionized, low-pressure xenon dc positive column discharge plasma. *Journal of Physics D: Applied Physics*. 29(3): 769 (1996)

[4] PHELPS database. http://www.lxcat.laplace.univ-tlse.fr/. retrieved the 15th of March

[5] Hagelaar, G. J. M. and L. C. Pitchford. Solving the Boltzmann equation to obtain electron transport coefficients and rate coefficients for fluid models. *Plasma Sources Science and Technology*. 14(4): 722 (2005)

[6] Lieberman, M. A. and A. J. Lichtenberg. *Principles of Plasma Discharges and Materials Processing*. (Wiley, 2005)

[7] P. Chabert and N. Braithwaite. *Physics of Radiofrequency Plasmas*. (Cambridge University Press, 2011)

[8] L.A. Viehland and E.A. Mason. Transport Properties of Gaseous ions over a wide energy range, IV*. *Atomic Data and Nuclear Data Tables*. 60, 37 (1995)

[9] Fruchtman, A., G. Makrinich, et al. Enhanced Plasma Transport Due To Neutral Depletion. *Physical Review Letters*. 95(11): 115002 (2005)

[10] Fruchtman, A. Energizing and depletion of neutrals by a collisional plasma. *Plasma Sources Science and Technology*. 17(2): 024016 (2008)

[11] Liard, L., J.-L. Raimbault, et al. Plasma transport under neutral gas depletion conditions. *Journal of Physics D: Applied Physics*. 40(17): 5192 (2007)

[12] Diamant, K. D. Resonant Cavity Plasma Electron Source. *Plasma Science, IEEE Transactions on*. 37(8): 1558-1562 (2009)

[13] Clausing, P. The Flow of Highly Rarefied Gases through Tubes of Arbitrary Length. *Journal of Vacuum Science and Technology.* 8(5): 636-646 (1971)

[14] Lobo, P. J., F. Becheri, et al. Comparison between Monte Carlo and analytical calculation of Clausing functions of cylindrical and conical tubes. *Vacuum*. 76(1): 83-88 (2004)

[15] Marino, L. Experiments on rarefied gas flows through tubes. *Microfluidics and Nanofluidics*. 6(1): 109-119 (2009)

[16] Diamant, K. D. Resonant Cavity Hollow Cathode. *41st AIAA/ASME/SAE/ASEE Joint Propulsion Conference & Exhibit*. July 2005, Tucson, AZ

[17] Diamant, K. D. Plasma Measurements in a Resonant Cavity Hollow Cathode. *42nd AIAA/ASME/SAE/ASEE*. 11 July 2006, Sacramento, CA.

[18] Diamant, K. D. Microwave Cathode for Air Breathing Electric Propulsion. *31st*

International Electric Propulsion Conference. Sept. 2009, Michigan, USA

Chapter 5: Electron extraction from the plasma source

We have studied in details the microwave plasma source properties in the previous chapter, under conditions where the metallic walls were grounded. In this chapter we focus on the question of electron extraction from the source. This implies the presence of a biased electrode placed after an extraction hole. In experiments, the extraction hole is identical to the pumping aperture. The objective in an electron source is to extract all the electron current available, i.e. to apply a bias potential large enough so that all the electron current is collected through the aperture and all the ion current is collected at the chamber walls. The diameter of the hole and the value of the bias potential that must be applied to extract the electron current are clearly related. One of the objectives of this chapter is to clarify this question in the conditions of our microwave source.

In section 5.1 we present the basic theory of electron extraction from a biased electrode. In section 5.2 we present the results from the 2D simulations, and compare them with theory for a chamber where electron extraction is performed through an electrode of given size placed on the discharge wall. In section 5.3 we present and discuss simulation results for a more realistic case where electrons are extracted through an aperture in the chamber wall and with a positively biased electrode outside the chamber.

5.1 Electron extraction from a biased electrode: theory

In this section we summarize previous theoretical work on electron collection by a biased electrode placed in a plasma. Most of the work referred to here has been done in the groups of A. Lacoste [1][2] and N. Hershowitz [3]-[7]. Some work about the plasma cathode electron source also can be found in Oks's book [8].

The equations of section 5.1.1 below are derived for a low pressure, "non-collisional" plasma, since the ion loss to the walls is simply written as the product of the plasma density times the Bohm velocity times exp(-1/2). This factor just accounts for the acceleration of the ions to the Bohm velocity at the sheath edge. In our conditions, we have seen that the plasma is actually collisional so that the theory below will have to be corrected to account for the ion collisionality. The correction to be made to the theory of section 5.1.1 in the case of a regime dominated by ampibolar diffusion is discussed in section 5.1.2. Finally a summary of the theory is given in section 5.1.3.

5.1.1 Theory for a low pressure plasma

Using the notations of Baalrud et al. [5], we consider a discharge chamber with a wall area A_w and an auxiliary electrode AE with an area A_{AE}. The wall voltage is V_w, the plasma potential is V_p and the positive bias voltage applied to the auxiliary electrode is V_{AE}. It is clear, from basic plasma theory, that if the auxiliary electrode area is "small enough", it will behave as a probe, i.e. will not perturb the plasma and the maximum electron current that can be collected if V_{AE} is large enough with respect to kT_e/e, is equal to the electron thermal current times the probe area, i.e. ($A_w env_{th}$ /4) which is the electron saturation current. In this case the plasma potential is not perturbed, the sheath in front the auxiliary electrode is an electron sheath, and no ions are collected by AE. It is also intuitive that, for a finite volume chamber, if the surface of the auxiliary electrode is "large enough", the auxiliary electrode can collect all the electron current if the bias voltage is large enough (we will prove this below). In that case the plasma potential is above V_{AE} the plasma potential "follows" the bias potential, the sheath in front AE is a positive, sheath, i.e. both A_W and A_{AE} collect ions, but A_{AE} collects all the electron current and A_W collects no electrons (the plasma potential is too high).

The general problem is actually a little more complicated than described with the intuitive explanations above, and we will now write the equations characterizing the variations of the current collected by the walls and the auxiliary electrode, and of the plasma potential with bias voltage and area ratio A_{AE}/A_W. We will see that a third regime is actually possible. We note $G_{e,w}$, $G_{i,w}$, $G_{e,AE}$, $G_{i,AE}$ the electron and ion fluxes to the electrodes, integrated over the walls and the auxiliary electrodes. The quantities eG are the current to the walls. Current conservation imposes that:

$$G_T = G_{e,w} + G_{e,AE} = G_{i,w} + G_{i,AE} \tag{5.1}$$

As mentioned above, the sheath in front of the auxiliary electrode can be an ion sheath or an electron sheath, depending on the size of the electrode and on the bias voltage. We will therefore consider separately, following Baalrud et al. [5], these two cases.

Ionic sheath

We first consider the case of a positively biased auxiliary electrode with an ionic sheath, i.e. collecting both electrons and ions. The electron and ion currents to the walls can be written classically as:

$$G_{e,w} = A_w n_0 \frac{V_e}{4} \exp\left[-\frac{e\left(\phi_p - \phi_w\right)}{kT_e}\right];\ G_{e,AE} = A_{AE} n_0 \frac{V_e}{4} \exp\left[-\frac{e\left(\phi_p - \phi_{AE}\right)}{kT_e}\right] \tag{5.2}$$

$$(5.3) \qquad G_{i,w} = A_w n_0 u_B \exp(-1/2); \quad G_{i,AE} = A_{AE} n_0 u_B \exp(-1/2)$$

Combining these equations with the current conservation equation (5.1) we can write:

$$(5.4) \left(A_w + A_{AE}\right) u_B \exp(-1/2) = \frac{V_e}{4}\left[A_w \exp\left(-\frac{e\left(\phi_p - \phi_w\right)}{kT_e}\right) + A_{AE} \exp\left(-\frac{e\left(\phi_p - \phi_{AE}\right)}{kT_e}\right)\right]$$

Using the notation:

$$(5.5) \qquad \mu = 4\exp(-1/2)\frac{u_B}{V_e} = \left(2\pi \exp(-1)\frac{m}{M}\right)^{1/2} \approx \sqrt{\frac{2.3m}{M}}$$

Equation (5.4) becomes:

$$(5.6) \qquad \mu\left(A_w + A_{AE}\right) = A_w \exp\left(-\frac{e\left(\phi_p - \phi_w\right)}{kT_e}\right) + A_{AE} \exp\left(-\frac{e\left(\phi_p - \phi_{AE}\right)}{kT_e}\right)$$

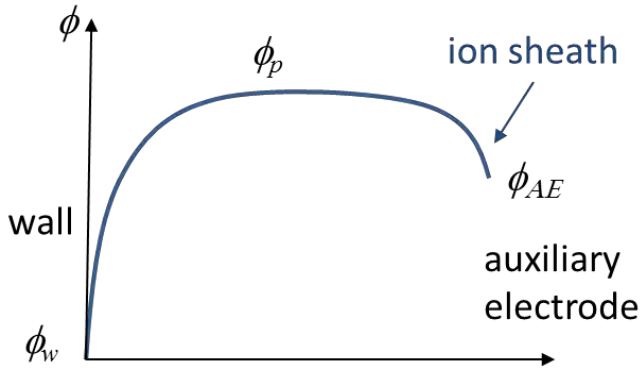

Figure 5.1: Schematic of the potential distribution in the ion sheath regime

This leads to:

$$(5.7) \qquad \phi_p - \phi_w = \frac{kT_e}{e}\ln\left(\frac{A_w + A_{AE} e^{\frac{e\left(\phi_{AE} - \phi_w\right)}{kT_e}}}{\mu\left(A_w + A_{AE}\right)}\right)$$

For large enough bias of the auxiliary electrode all the electron current is collected by AE and equation (5.7) becomes:

$$(5.8) \qquad \phi_p - \phi_{AE} = \frac{kT_e}{e}\ln\left(\frac{A_{AE}}{\mu\left(A_w + A_{AE}\right)}\right)$$

This expression gives the potential difference between the biased electrode and the plasma and shows that the plasma potential follows the potential of the biased electrode. The sheath next to AE is an ion sheath only if this voltage is larger $kT_e/2$, which is the Bohm condition. This imposes a constraint (argument of the log must be larger than exp(1)) on the right hand side of equation (5.8), leading to:

(5.9)
$$\boxed{\frac{A_{AE}}{A_w} \geq \left(\frac{\exp(1/2)}{\mu} - 1 \right)^{-1} \approx 1.7\mu}$$

For xenon, this corresponds to $A_{AE}/A_w > 5\text{x}10^{-3}$.

In this regime the ratio of the electron current collected by the biased electrode, to the total electron or ion current collected to all the walls is:

$$\frac{G_{e,AE}}{G_T} = \frac{V_e/4}{u_B \exp(-1/2)} \frac{A_{AE}}{\left(A_w + A_{AE}\right)} \exp\left[-\frac{e\left(\phi_p - \phi_{AE}\right)}{kT_e} \right]$$

Combining this equation with equation (5.4), this gives:

(5.10)
$$\boxed{\frac{G_{e,AE}}{G_T} = \frac{1}{1 + \frac{A_w}{A_{AE}} \exp\left(-\frac{e\left(\phi_{AE} - \phi_w\right)}{kT_e} \right)}}$$

This clearly shows that all the electron current is collected by the auxiliary electrode ($G_{e,AE} = G_T$) if the bias voltage on it is large enough (the needed bias value to extract most of the electron current depends on the electron temperature and on the area ratio).

When the ratio of the biased electrode area to the chamber area is smaller than the limit value given by equation (5.9) the sheath next to AE cannot be an ion sheath.

Electronic sheath

We consider now as situation where the sheath in front of AE is an electron sheath. This means that the auxiliary electrode does not collect any ion current, and collect the saturation current ($A_{AE}nV_e/4$). With these assumptions, equation (5.6) becomes:

(5.11)
$$\mu A_w = A_w \exp\left(-\frac{e\left(\phi_p - \phi_w\right)}{kT_e} \right) + A_{AE}$$

This gives the following expression of the plasma potential in this regime:

(5.12)
$$\phi_p - \phi_w = -\frac{kT_e}{e} \ln\left(\mu - \frac{A_{AE}}{A_w} \right)$$

This equation is defined only if:

(5.13) $$\boxed{\frac{A_{AE}}{A_w} < \mu}$$

In this regime the maximum relative electron current than can be collected by the auxiliary electrode is given by:

$$\frac{G_{e,AE}}{G_T} = \frac{V_e/4}{u_B \exp(-1/2)} \frac{A_{AE}}{A_w}$$

i.e., provided that the bias potential is larger than the plasma potential:

(5.14) $$\boxed{\frac{G_{e,AE}}{G_T} = \frac{1}{\mu} \frac{A_{AE}}{A_w}}$$

This depends only on the electrode area ratio and is always less than 1 (because of equation (5.13).

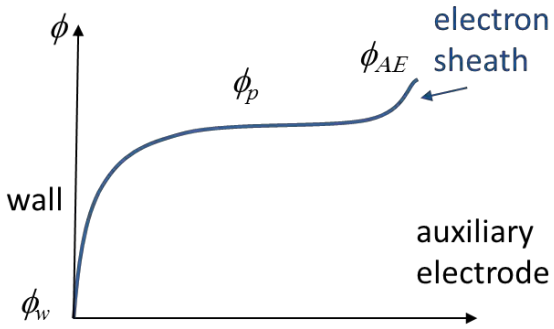

Figure 5.2: Typical potential distribution in the electron sheath regime

Double sheath

We have seen above that the ion sheath regime can exist only if $\frac{A_{AE}}{A_w} \geq \left(\frac{0.6}{\mu} - 1\right)^{-1} \approx 1.7\mu$ while the electron sheath regime requires $\frac{A_{AE}}{A_w} < \mu$.

We therefore need to the study the intermediate situation where

(5.15) $$\mu \leq \frac{A_{AE}}{A_w} < \left(\frac{0.6}{\mu} - 1\right)^{-1} \approx 1.7\mu$$

In this relatively narrow range of values of the area ratio, Baalrud et al. [5] show that a double sheath should exist in front of the auxiliary electrode to preserve

quasineutrality and balance the currents to the walls. A potential minimum ϕ_D ("potential dip") forms in front of the electrode to limit the extracted electron current which, from equation (5.14), tends to become larger than the maximum current when A_E/A_W becomes lager than μ. The electrode bias potential in this regime is above the dip potential and above the plasma potential, and no ions are collected by the AE electrode. The electron current is to the AE electrode is equal to the maximum current, which must be expressed at the potential dip. An electron Child-Langmuir sheath should exist between the potential dip and the biased electrode. Therefore the balance equation (5.4) becomes:

(5.16) $$\mu A_w = A_{AE} \exp\left(-\frac{e\left(\phi_p - \phi_D\right)}{kT_e}\right)$$

This gives

(5.17) $$\boxed{\phi_p - \phi_D = \frac{kT}{e}\ln\left(\frac{\mu A_w}{A_{AE}}\right)}$$

The balance equation here does not provide the plasma potential, but the value of the potential dip. We see from the above equation that the dip potential is, in the range of area ratio defined by equation (5.15), lies in the range:

(5.18) $$0 < \phi_p - \phi_D < \frac{kT}{2e}$$

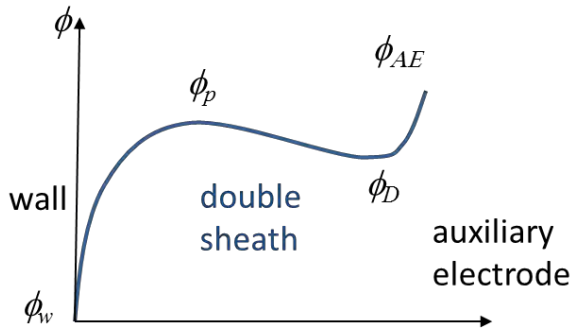

Figure 5.3: Potential distribution in the double sheath regime.

Baalrud et al. [5] give some hints on the parameters controlling the plasma potential. Since there is a Child Langmuir sheath between the potential dip and the biased electrode, the extracted electron current must also be given by a Child-Langmuir law, i.e. is a function of the $(\phi_{AE}\text{-}\phi_D)$ and of the electron Child-Langmuir sheath length. The Child-Langmuir sheath length should not change with applied bias voltage otherwise the effective area of the auxiliary electron would change and so would the

extracted current (which must be equal to the total available electron current in this regime). These arguments show that the dip potential should follow the applied bias potential so that $(\phi_{AE}-\phi_D)$ stays constant for large enough bias voltage. The same is therefore true for the plasma potential because of equation (5.17). One can therefore conclude that the plasma potential must also increase linearly with the biased electrode potential, but the detailed calculations of the potential difference between biased electrode and plasma requires a detailed study of the Child-Langmuir sheath and is beyond the scope of this thesis.

The derivations of this section are very similar to those of Baalrud et al. [5] and are based on the assumption of a collisionless plasma where the ion flux to the surface is given by the classical expression $[nu_B exp(-1/2)]$.

We show below that all the derivations above are still valid in a collisional, ambipolar regime, if the parameter μ is properly modified.

5.1.2 Theory for a collisional plasma

In the case of a diffusion dominated collisional plasma, the ion losses to the wall must be modified as described below.

Remembering from the global model in the preceding chapter, that the total ion (or electron) losses to the wall is balanced by ionization in the volume, and that, for the ambipolar regime, the total losses to the wall per unit time is equal (equation (4.18)) to:

(5.19)
$$\Gamma_s A = \frac{kT_e}{M}\frac{1}{k_{in} n_g \Lambda^2}\bar{n}V$$

with
$$\frac{1}{\Lambda^2} = \frac{\chi_{01}^2}{R^2} + \frac{\pi^2}{L^2}$$

where the averaged plasma density is related to the maximum plasma density by (see equation (4.17)):

(5.20)
$$\bar{n} = n_0 \frac{4J_1(\chi_{01})}{\pi\chi_{01}} \approx 0.28 n_0$$

Relating this expression to the collisionless expression used in the previous section, we can write equation (5.19) in the following form, defining a correction parameter *h*:

(5.21)
$$\Gamma_s A = n_0 h u_B \exp(-1/2)(A_w + A_{AE})$$

The correction parameter *h* can be defined by equating the expression above to the

loss term in the ambipolar regime, equation (5.19).

This means that the derivations of the previous section are still valid in the collisional regime if we multiply the Bohm velocity by *h*, or, equivalently, the μ coefficient by *h*.

From equations (5.19) and (5.21), the *h* parameter is obtained as:

(5.22) $$h = \frac{kT_e}{Mu_B}\frac{1}{k_{in}n_g\Lambda^2}\frac{\bar{n}}{n_0}\frac{V}{\left(A_w + A_{AE}\right)}$$

After some simple transformations, and replacing the different constants by their values, we get:

(5.23) $$h = \frac{2\chi_{01}J_1\left(\chi_{01}\right)\exp\left(1/2\right)}{\pi}\frac{u_B}{k_{in}n_gR}\frac{1+\dfrac{R^2\pi^2}{L^2\chi_{01}^2}}{\left(1+\dfrac{R}{L}\right)}$$

The constant coefficient of this equation (first fraction on the right hand side) is about 1.3. In the case of Diamant's experiment, R is much smaller than L, and this expression can be simplified to:

(5.24) $$h \approx 1.3\frac{u_B}{k_{in}n_gR}$$

For our conditions, xenon, electron temperature around 1 eV, 100 mtorr pressure, R=2 cm and L=10 cm, we have u_B~800 m/s, $k_{in}n_g$~1.6x10^6 s^{-1} and

(5.25) $$h \approx 2.5\times10^{-2}$$

In the collisional, ambipolar regime, all the expressions of section 5.1.1 can be used if we replace μ by $h\mu$.

For xenon at 100 mtorr, and for the chamber dimensions of Diamant (see above), we have, numerically:

(5.26) $$h\mu \approx 7.5\times10^{-5}$$

Note that if λ_i is the mean free path of thermal ions, and $V_i = \left(8kT_i/\pi M\right)^{1/2}$ is the ion thermal velocity, we have $\lambda_i = V_i/\nu_{in}$, and we can write:

(5.27) $$h \approx 0.8 \frac{\lambda_i}{R} \left(\frac{T_e}{T_i} \right)^{1/2}$$

5.1.3 Summary of the theory of electron extraction

When an electrode is biased positively with respect to a grounded plasma source to extract electrons, three different regimes can be identified. These regimes are characterized respectively with an ionic sheath in front of the extracting (auxiliary) electrode AE, an electron sheath, or a double sheath. In a collisionless situation, the source operates in one of these three regimes depending only on the ratio A_{AE}/A_w of the extraction electrode area over the chamber wall area and on the ion mass. In a collisional situation the regime depends also on other parameters such as the ion mean free path and the ratio of electron to ion temperatures.

In the collisionless regime, *h* is equal to 1, and in the collisional regime *h* is given by equations (5.23) and (5.25).

We note α the area ratio:

$$\alpha = \frac{A_{AE}}{Aw}$$

We can summarize the results of the previous sections as follows.

The three possible regimes for electron extraction are ($\mu h \approx 7.5 \times 10^{-5}$):

- The ionic sheath regime, for $\alpha \geq 1.7 \mu h$
- The electronic sheath regime, for $\alpha < \mu h$
- The double sheath regime, for $\mu h < \alpha < 1.7 \mu h$

Ionic sheath $\alpha \geq 1.7 \mu h$

In the ionic sheath regime, the biased electrode collects electrons and ions, and all the electron current can be extracted if the bias voltage is large enough so that:

(5.28) $$\phi_{AE} - \phi_w >> -\frac{kT_e}{e} \ln \alpha$$

This can be easily deduced from the expression of the normalized extracted electron current:

(5.29) $$\frac{G_{e,AE}}{G_T} = \frac{1}{1 + \alpha^{-1} \exp\left(-\frac{e(\phi_{AE} - \phi_w)}{kT_e} \right)}$$

The plasma potential is obtained from

$$\phi_p - \phi_w = \frac{kT_e}{e}\ln\left(\frac{1+\alpha e^{\frac{e(\phi_{AE}-\phi_w)}{kT_e}}}{h\mu(1+\alpha)}\right) \tag{5.30}$$

The ionic sheath regime can be used for electron extraction but the fact that the plasma potential increases with the bias voltage indicates that energy will be lost in the acceleration on ions to the walls. It is therefore important to operate at the minimum extraction voltage giving a sufficient extracted current. For example for extraction of more than 90% of the maximum current, $\alpha^{-1}\exp\left(-e\left(\phi_{AE}-\phi_w\right)/kT_e\right)$ must be less than 0.1, i.e. $\phi_{AE}-\phi_w > -kT_e/e\ln\left(0.1\alpha\right)$. For a radius of the extraction area of 5 mm in a cylindrical discharge chamber of 5 cm radius and 10 cm length, this gives $\phi_{AE}-\phi_w > 7.5kT_e/e$.

Figure 5.4 shows the fractional extracted electron current (defined in equation (5.29)) as a function of bias voltage for different area ratios and a fixed electron temperature of 1 eV (Figure 5.4(a)), and as a function of electron temperature , for a given area ration of 10^{-2} (Figure 5.4(b)). As can be deduced from equation (5.29), the profile of the extraction current-voltage characteristics is shifted toward higher voltages when the area ratio is decreased at constant temperature, and the slope of the current as a function of bias voltage decreases when the electron temperature increases at constant area ratio.

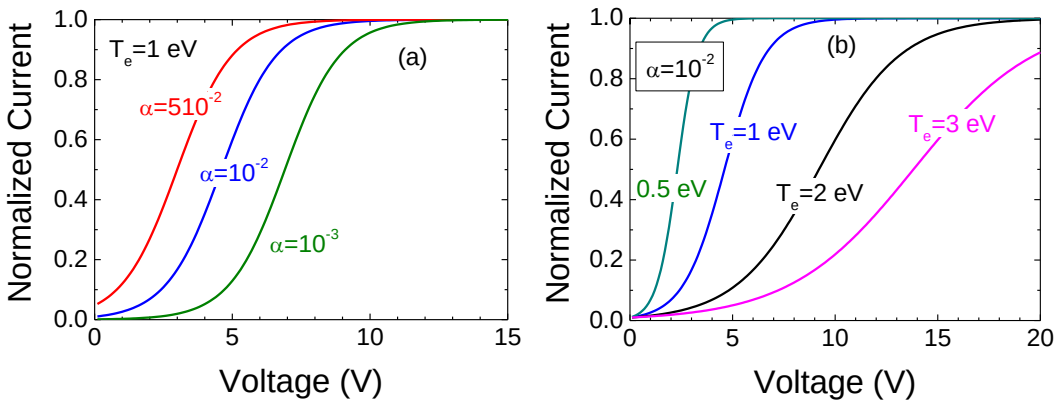

Figure 5.4: Normalized extracted electron current as a function of bias voltage, (a) for different values of the area ratio and an electron temperature of 1 eV, (b) for different values of the electron temperature and for an area ratio of 10^{-2}.

Figure 5.5 shows the plasma potential as a function of bias voltage from equation (5.30). For zero bias voltage, this equation gives a plasma potential of $\phi_p - \phi_w = -\frac{kT_e}{e}\ln(h\mu)$, while for a bias voltage much larger than kT_e/e the plasma potential "follows" the bias voltage as $\phi_p \approx \phi_{AE} + \frac{kT_e}{e}\ln\left(\frac{\alpha}{h\mu}\right)$. For α=10^{-2}, and for xenon in our pressure conditions ($h\mu$~0.75x10^{-4}), this gives a plasma potential about 5 V above the bias potential, as seen in Figure 5.5.

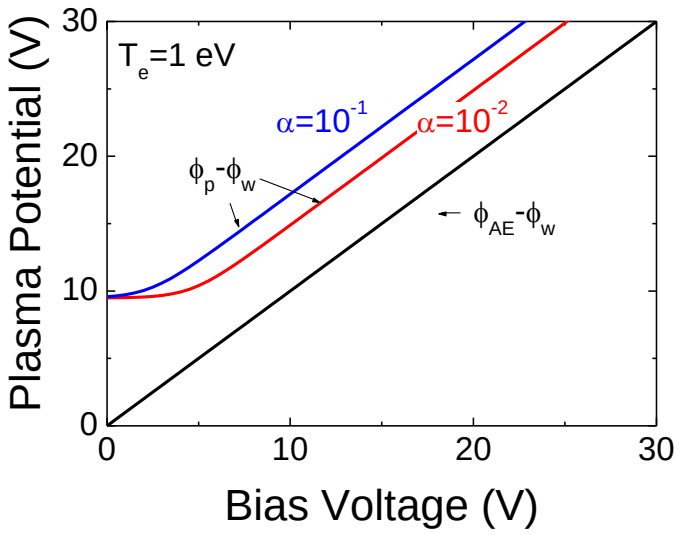

Figure 5.5: Plasma potential as a function of bias voltage in our conditions (xenon, 100 mtorr, T_e=1 eV) for two values of the area ratio (from equation (5.30)).

Electronic sheath $\alpha < \mu h$

In the electronic sheath regime the plasma potential is below the biased electrode potential, ions are not collected by the biased electrodes, and the extracted electron current is smaller than the total current to the walls and is given by:

(5.31) $$\frac{G_{e,AE}}{G_T} = \frac{1}{\mu}\frac{A_{AE}}{A_w}$$

The plasma potential is given by:

(5.32) $$\phi_p - \phi_w = -\frac{kT_e}{e}\ln(\mu h - \alpha)$$

This regime is not interesting for electron extraction since the extracted current is smaller than the maximum.

Double sheath $\mu h < \alpha < 1.7\mu h$

In the double sheath regime the potential of the biased electrode is above the plasma potential (i.e. and electronic sheath is present in front of the electrode), but a potential minimum must form in the plasma just before the electronic sheath, to adjust the extracted electron current to its maximum possible value. This corresponds to a double sheath. The extracted electron current is:

$$\frac{G_{e,AE}}{G_T} = 1$$

The minimum potential is between *0* and $kT_e/2e$ below the plasma potential. The plasma potential should follow the bias potential but no clear theory is available to describe its value.

This regime can be interesting because all the electron current is extracted and the plasma potential is below the applied

The 3 regimes in the conditions of Diamant's experiments

In the conditions of the experiments of Diamant considered in this thesis, the $h\mu$ parameter is on the order of 0.75×10^{-4} (see equations (5.25)(5.26) above). Since the chamber wall area A_w is given (A_w~150 cm^2 for a cylinder with R=2 cm, L=10 cm), one can calculate the extraction areas A_{w1} and A_{w2} that correspond to the limit between the three different regimes. Assuming that the extraction electrode is a disk of radius r, the two values r_1 and r_2 of the electrode radii defining the limits are:

(5.33)
$$\frac{\pi r_1^2}{A_w} = h\mu \qquad \frac{\pi r_2^2}{A_w} = 1.7h\mu$$

This gives in our conditions (xenon, 100 mtorr):

$r_1 \approx 0.6$ mm $r_2 \approx 1$ mm

Therefore the double sheath regime can be obtained in our conditions only for very low (and unrealistic) extraction surface, and the natural regime of operation (for an extraction electrode radius of several mm) will be the ionic sheath regime.

5.2 2D model with a closed chamber

In this section we study electron extraction with the help of the more accurate 2D model (the theory of the previous section was based on a global model).

We first consider that the extraction electrode (auxiliary electrode) is a disk centered on axis, on the right wall (facing the quartz plate) of the chamber. We perform 2D

simulations with gas heating and no gas flow (no pumping) and we study the influence of the extraction area on the results.

Figure 5.6 shows the distribution of potential in the chamber in the 60 W, 100 mtorr case, with an extracting electrode of radius 4 mm. As above, the dimensions of the discharge chamber are those of the Diamant's experiments, L=10 cm, and R=2 cm. In these conditions the area ratio α is equal to 3.3×10^{-2}. The bias voltage applied to the extracting electrode is 20 V. The area ratio α is much larger than $1.7 h\mu$ ($h\mu$ is equal to 7.5×10^{-5} in our conditions, see above) so that the electron source should operate in the ionic sheath regime. This is confirmed by *Figure 5.6* and *Figure5.7* which show that the plasma potential is a few volts above the anode potential in these conditions.

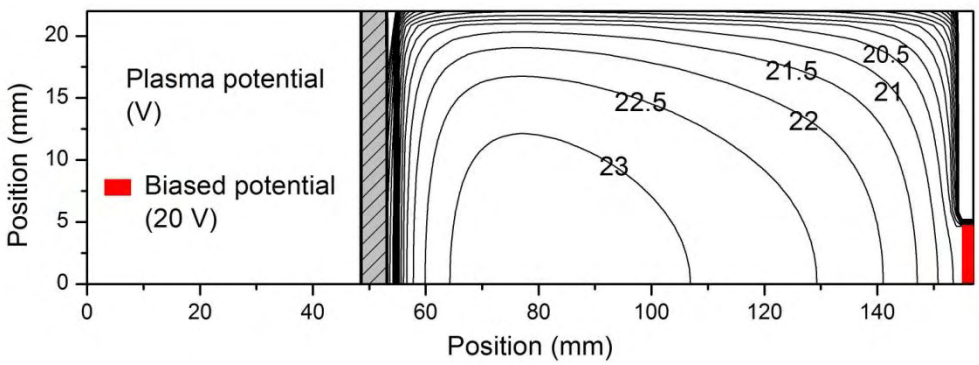

Figure 5.6: 2D potential distribution in the discharge chamber for an extracting electrode of radius 4 mm (area ratio $\alpha \sim 3.3 \times 10^{-2}$). The extracting electrode is biased at 20 V. The microwave power dissipated in the plasma is 60 W and the xenon pressure is 100 mtorr. Gas heating is included but without flow.

We also see on the axial distribution of the potential shown in *Figure5.7* that the plasma potential follows the bias voltage as expected in the ionic sheath regime, and that the potential on the dielectric surface increases with the bias voltage. This is because in the presence of a dielectric surface it is actually impossible to draw all the electron current to the anode and some electron current must flow to the dielectric surface to balance the ion flux. Therefore, to keep an electron current equal to the ion (Bohm current on the dielectric surface) the surface potential must be below the plasma potential by only a few times kT_e. As can be seen in *Figure5.7* the potential difference between the plasma and the dielectric surface stays practically constant, on the order of 10 V, when the bias voltage is increased.

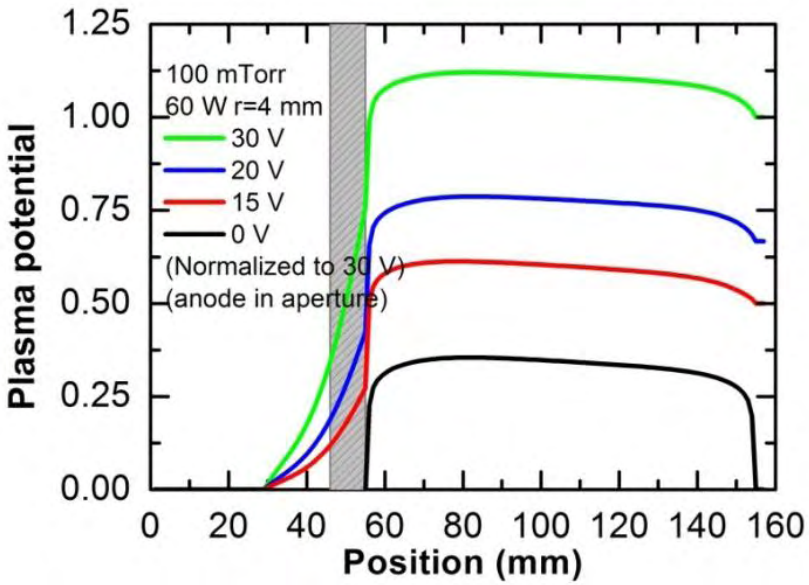

Figure5.7: Axial distributions of the potential in the conditions of Figure 5.6 and for four values of the bias voltage (0, 15, 20 and 30 V).

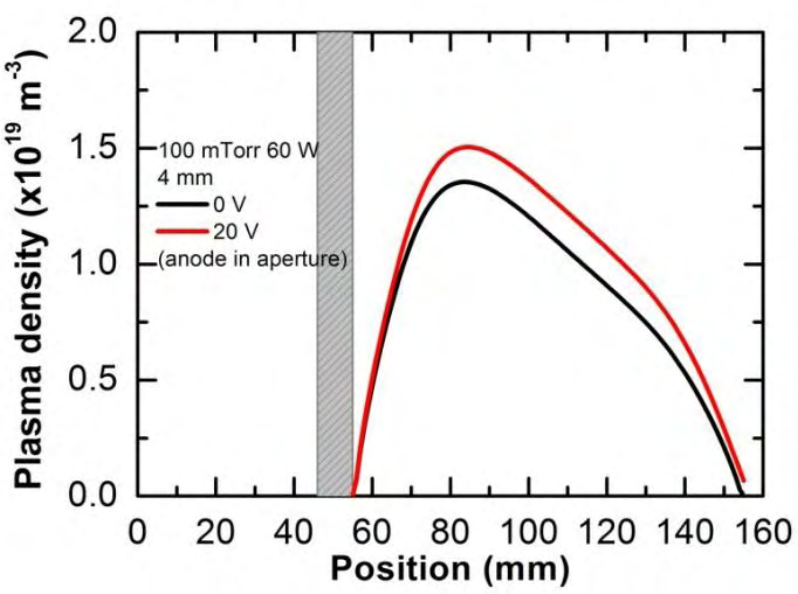

Figure 5.8: Plasma density axial distribution in the conditions of Figure 5.6 for 0 V and 20 V.

Assuming that the plasma density is not strongly affected by the bias voltage as shown in Figure 5.8, the ion (Bohm) current and therefore the electron current to the dielectric walls are the same as without bias. This current must therefore be equal to the total current to the walls times the ratio of the dielectric surface area to the total wall area. In our cylindrical geometry, this area ratio is $\left[2\left(1+L/R\right)\right]^{-1}$, i.e. is equal to 1/12. Therefore less than 10% of the total electron current produced is lost to the dielectric wall and cannot be extracted by the anode.

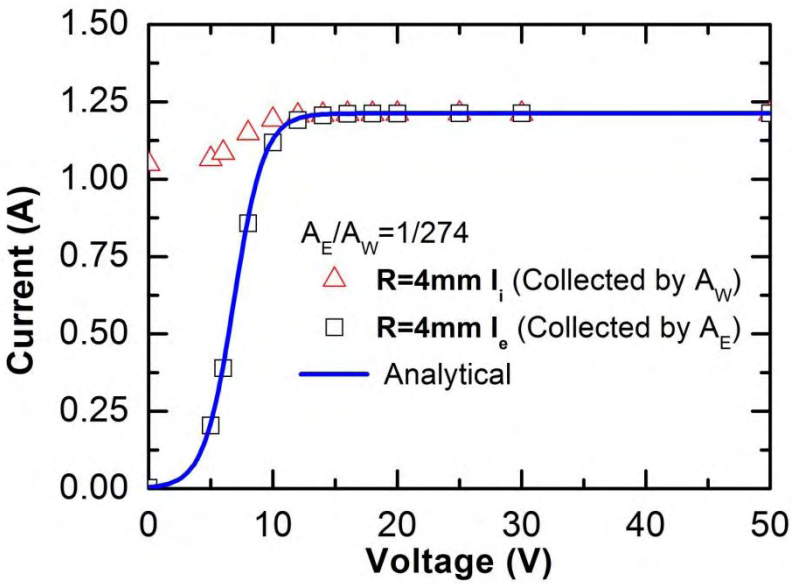

Figure 5.9: Extracted electron current as a function of bias voltage in the same conditions as Figure 5.6 (extracting electrode radius 4 mm, 60W, 100 mtorr), from the 2D model (square symbols), and from the analytical expression, equation (5.29) scaled to the maximum current. The ion current to the wall is also represented (triangles).

We can deduce from the simulations the extracted electron current normalized to the total electron or ion current to the walls, as a function of the bias voltage. Since the electron source operates in the ionic sheath regime, the extracted electron current should be close to the analytical expression equation (5.29). This is the case as can be seen in Figure 5.9 which shows the extracted electron current as a function of bias voltage obtained with the 2D model and from the analytical expression (scaled to the same maximum current). The agreement between the ionic sheath theory and the 2D model is excellent.

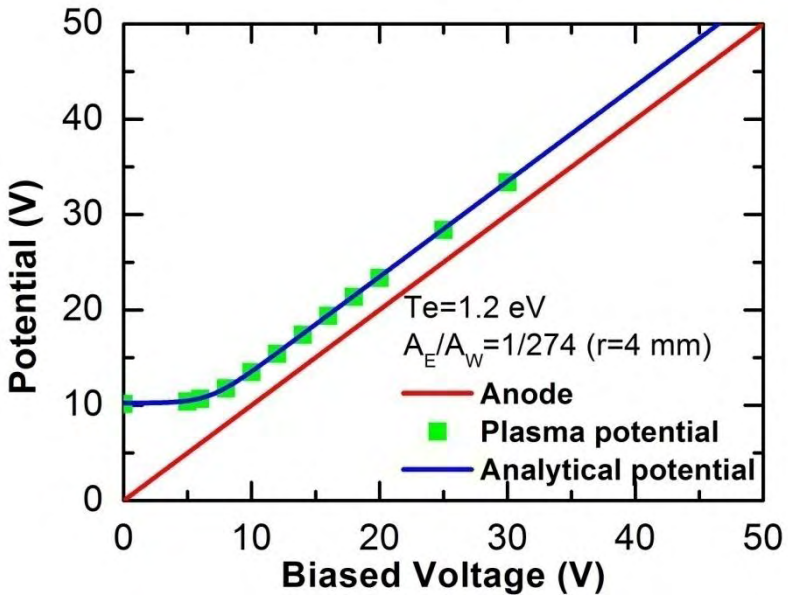

Figure 5.10: Plasma potential as a function of extracting (bias) voltage in the conditions of Figure 5.6-Figure 5.9, from the 2D model (square symbols), and from the analytical expression, equation(5.30).

The maximum plasma potential from the 2D model is represented as a function of extracting voltage in Figure 5.10. The plasma potential from the analytical equation (5.30) is also represented on this figure. The 2D results are in excellent agreement with the theory, and the plasma potential increases linearly with the bias voltage when this voltage is above about 10 V (where all the available electron current is extracted). For large enough bias voltage, the plasma potential is about 5 V above the bias voltage, in agreement with the discussion of section 5.1.3 for the ionic sheath case.

According to the last part of section 5.1.3 the transition to the double sheath regime should occur for lower values of the extracting electrode radius, on the order of 1 mm. Indeed we see in *Figure 5.11* and *(*5.12) that the case with extracting electrode radius of 1 mm corresponds to a double sheath regime.

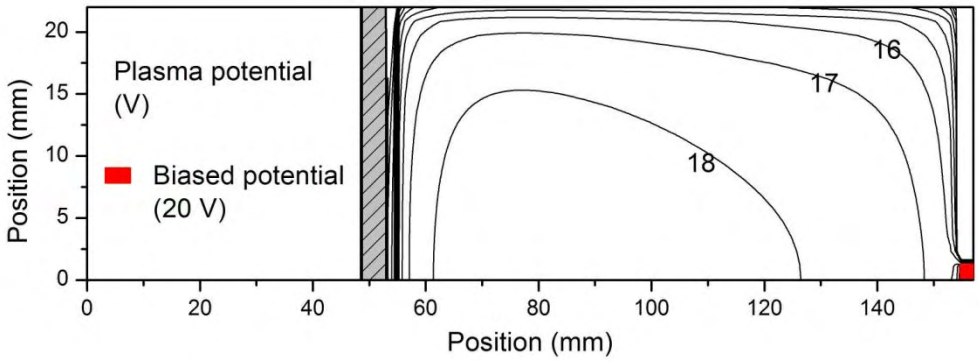

Figure 5.11: 2D potential distribution in the discharge chamber for an extracting electrode of radius 1 mm (area ratio α~2.1x10^{-3}). The extracting electrode is biased at 20 V. The microwave power dissipated in the plasma is 60 W and the xenon

pressure is 100 mtorr. Gas heating is included but without flow.

Figure 5.11 shows the 2D distribution of the potential in the case of a 1 mm radius and a bias voltage of 20 V, and *Figure 5.12* displays the axial distribution of the plasma potential for four different values of the bias voltage: 0, 5, 15, and 20 V. We see on *Figure 5.12* that for 0 V bias, the source operates in an ionic sheath regime, with a plasma potential above the anode potential, while above 15 V, it operates in a double sheath regime where the plasma potential is below the bias potential. In this regime, the 2D model is in agreement with the theory, i.e. it predicts an electron sheath next to the extraction electrode, and a potential dip just before the electron sheath.

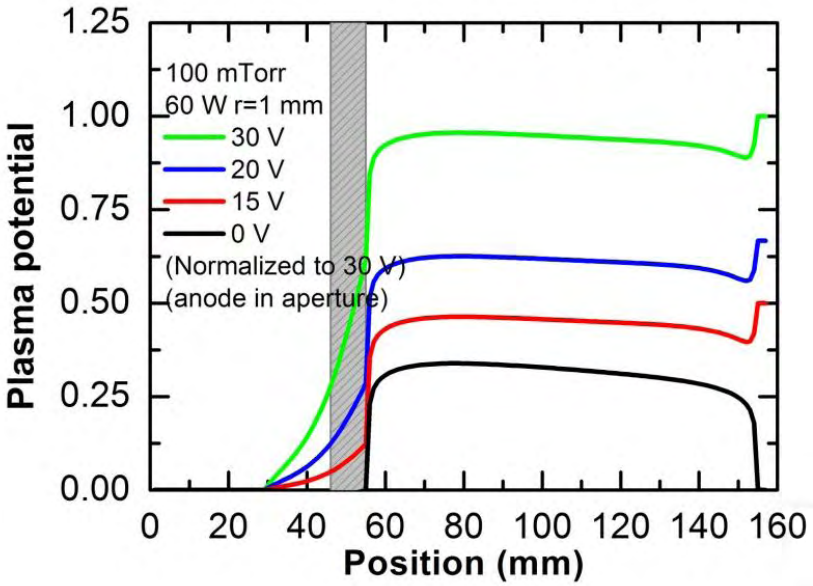

Figure 5.12: Axial variations of the plasma potential for 4 values of the bias voltage (0, 15, 20, 30 V) in the same conditions as Figure 5.11.

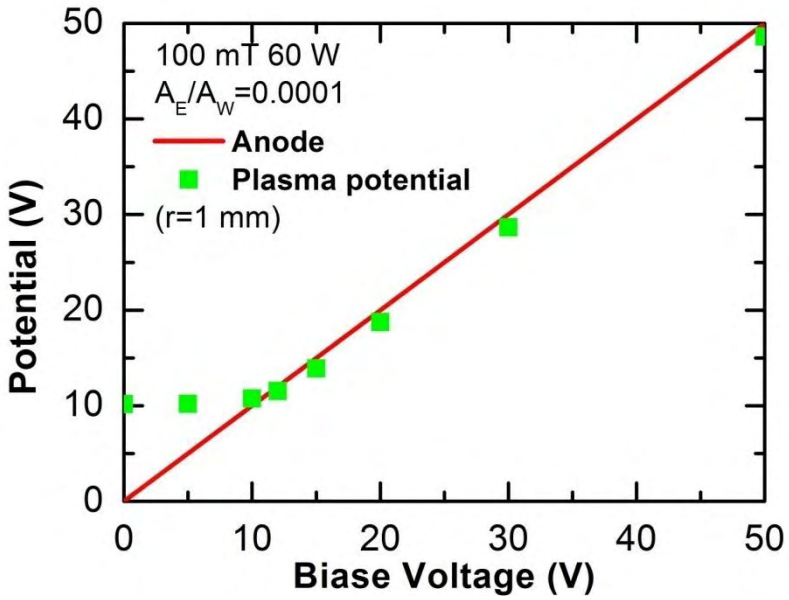

Figure 5.13: Plasma potential (symbols)as a function of bias voltage in the conditions of Figure 5.11 and Figure 5.12 (100 mtorr, 1 mm anode radius).

For bias voltage larger than 10 V the plasma potential is below the bias voltage and increases linearly with the bias voltage as seen in *Figure 5.13*.

The calculated extracted electron current as a function of bias voltage for a 1 mm radius anode is plotted in *Figure 5.14*.

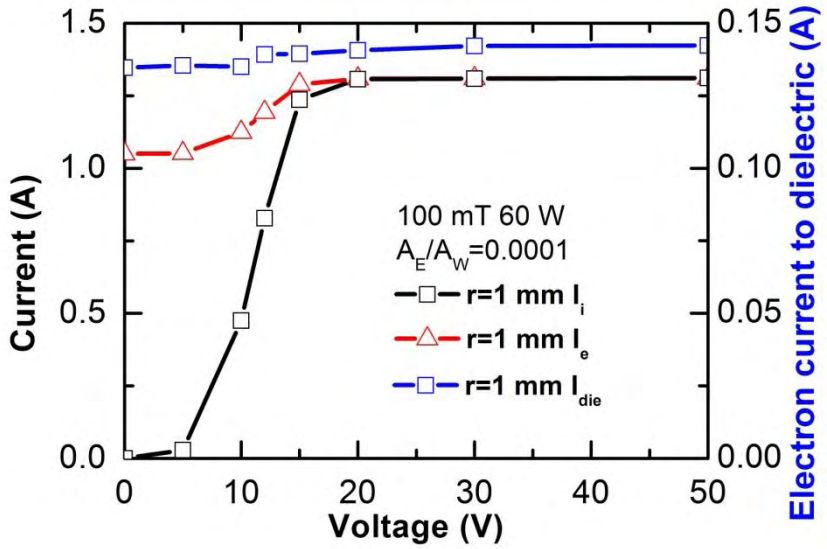

Figure 5.14: Extracted electrons current (black line, square symbols) as a function of bias voltage for a 1 mm anode radius (100 mtorr, 60 W). The electron current to the dielectric surface (blue line, square symbols), and the ion current to the grounded wall (red line, triangle symbols) are also represented.

The maximum electron extracted current is on the order of 1.25 A, i.e. slightly larger than the total electron current to the wall without extraction. Part of this current increase is due to the fact that in this collisional regime, the potential increase next to the anode leads to a non-negligible supplementary ionization. *Figure 5.14* also shows the electron current to the dielectric surface. The figure confirms that the current to the dielectric surface is less than 10% of the total electron current, as discussed above.

Finally we performed simulations for small anode radii such that $\frac{\pi r_1^2}{A_w} < h\mu$ (see (5.33)) to study the anodic sheath regime predicted by the theory. This corresponds to quite small anode radii, i.e. smaller than 0.6 mm at 100 mtorr in our conditions and the numerical convergence was difficult in these conditions because of the small anode radius compared with the discharge dimensions. We then decreased the pressure to increase the value of *h* and therefore to increase the maximum anode radius corresponding to an electronic sheath regime (to make the numerical

calculations easier). Even with a lower pressure, the model failed to predict the existence of an electronic sheath regime, i.e. a regime where the maximum current extracted at the cathode is $\frac{G_{e,AE}}{G_T} = \frac{1}{\mu}\frac{A_E}{A_W}$ (eq. (5.31)) , and the plasma potential does not increase with increasing bias voltage. We did not further explore the reasons for which the model did not predict this regime and more work is needed to understand the reasons for this limitation of the model (one possible reason is the drift-diffusion approximation for electrons which implies that the electron transport in the electron sheath is always collisional, i.e. controlled by mobility).

5.32D model with an aperture

In the section above, the problem was simplified by using an anode placed on the chamber wall. In a real electron source electrons must be extracted through an aperture in the chamber and the anode is placed outside the chamber. In this section we assume that the electrons are extracted through the pumping aperture.

Figure 5.15 shows the simulated geometry when the aperture is taken into account, and the distribution of the potential when the anode is grounded. The anode is placed far away from the aperture plane on the pumping side and its radius is supposed to be the same as the discharge cylinder radius. The gas is pumped from the space on the walls, between the downstream aperture plane and the anode.

In this section the reported results have been obtained at a pressure of 100 mtorr before the plasma is ON (i.e. the mass flow rate is adjusted to obtain a pressure of 100 mtorr). Simulations have been performed with different radii r and thickness l of the extraction aperture, the typical value (in Diamant's experiments) being r=4 mm, l=1 cm.

Note that in our cavity when the mass flow rate is fixed (1 mg/s in experiment), the gas pressure is decided by the aperture size. To get a high gas pressure, the aperture size should be small, on the other hand, the electron current will become difficult to be extracted from a small size aperture, and even no electrons can be extracted when the aperture size is too small. The mechanism of the electron extraction with respect to the aperture size will be discussed in the following of this section.

Experimentally, when the gas pressure is too low, not only the breakdown becomes difficult to trigger (see section 3.4) but also one has to adjust the antenna in a large length scale to obtain the least microwave power reflection during the steady state operation, considering the small cavity size, this situation should be avoided. Hence the gas pressure is chosen at 100 mTorr for the discharge. We will also focus on this gas pressure as a typical simulation parameter.

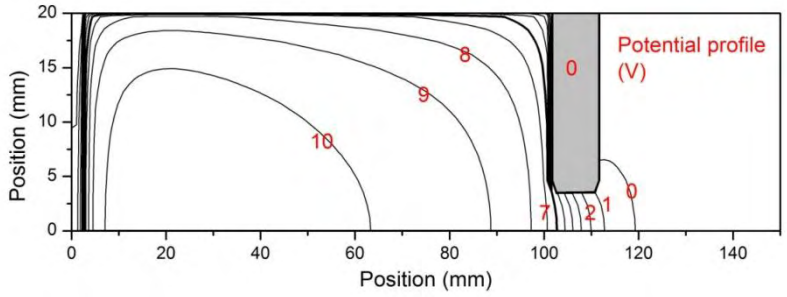

Figure 5.15: Discharge geometry and equipotential contours with an aperture (radius 4 mm, length 1 cm). The anode is grounded.

Figure 5.16 displays the simulated results for a typical case at 100 mtorr, 60 W, with a bias voltage of 30 V on the anode, and with the standard aperture dimensions r=0.4 cm, l=1 cm. The plasma density, electron temperature, plasma potential, metastable density, gas density , and ionization source term are displayed in Figure 5.16, b, c, d, e, f, respectively.

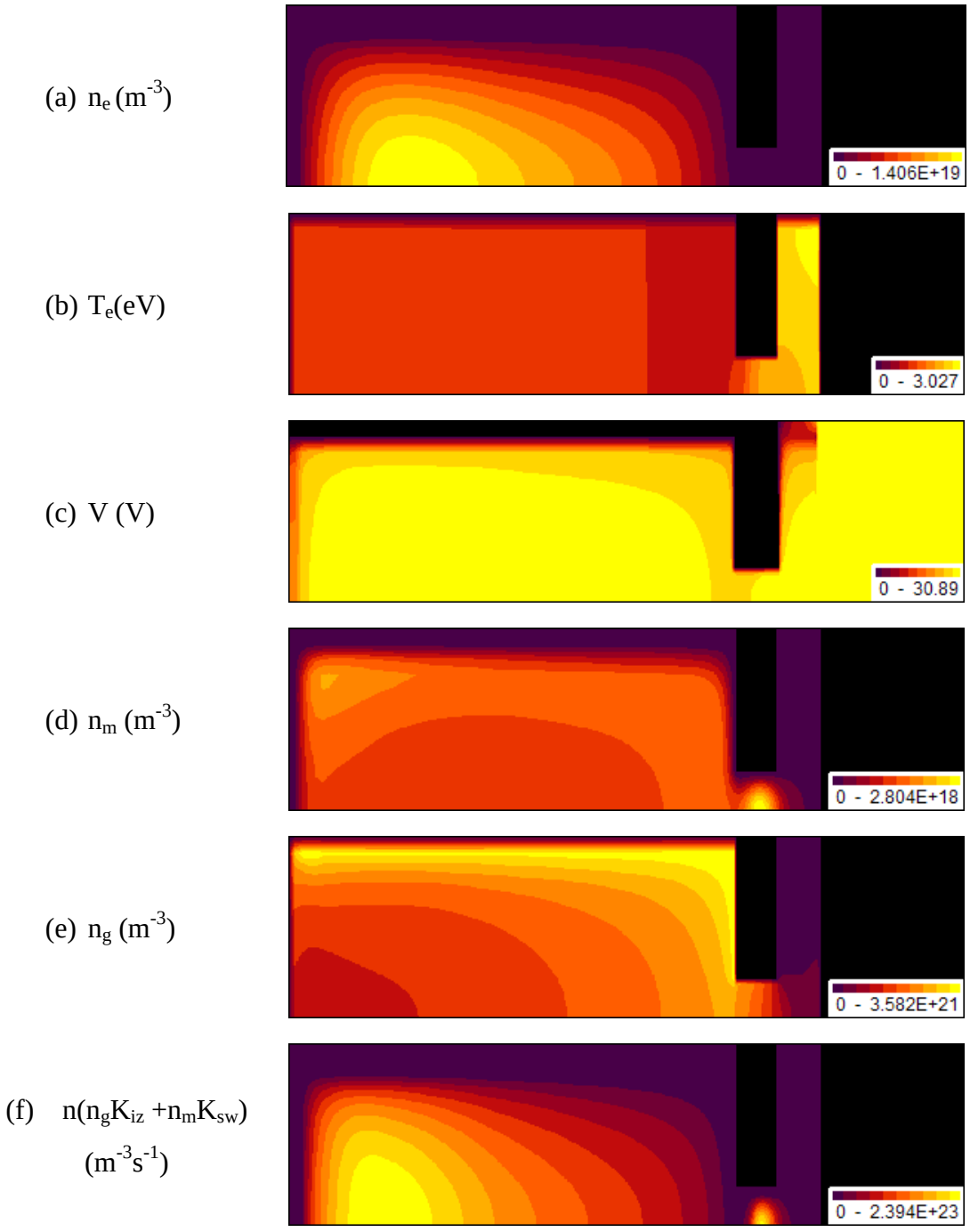

Figure 5.16: 2D distributions of (a) plasma density, (b) electron temperature, (c) plasma potential, (d) metastable atom density, (e) gas density, (f), total ionization source term. The gas pressure before turning the plasma ON is 100 mtorr, the power is 60 W, the bias voltage is 30 V. The radius and thickness of the aperture are 4 mm and 1 cm respectively.

We see on Figure 5.16 that the electron temperature increases through the aperture because of the potential increase. This electron temperature increase is responsible for an important enhancement of the ionization rate in the aperture. The plasma potential

is close to the bias potential and practically all the electron current is extracted to the anode in these conditions. The regime is typical of the ionic sheath regime although a small decrease of the plasma potential can be seen before the potential increase at the aperture (as in a double sheath regime). A comparison of on axial plasma density and ionization source term profiles with and without full description of the aperture is shown in *Figure 5.17*.

Important differences can however appear at low extraction voltages of for lower radii larger thicknesses of the aperture, as can be seen in *Figure 5.18*.This is because, when the aperture radius is too small, the anode potential cannot penetrate in the discharge chamber and no electron current is extracted even for large applied biases. For a given aperture thickness, the anode potential no longer penetrates inside the chamber for a radius smaller than a given value (which varies with the aperture thickness). For example (Figure 5.18*b*) the anode potential does not penetrate in the discharge for a radius of 1.5 mm and below and no electron current can be extracted.

(a)

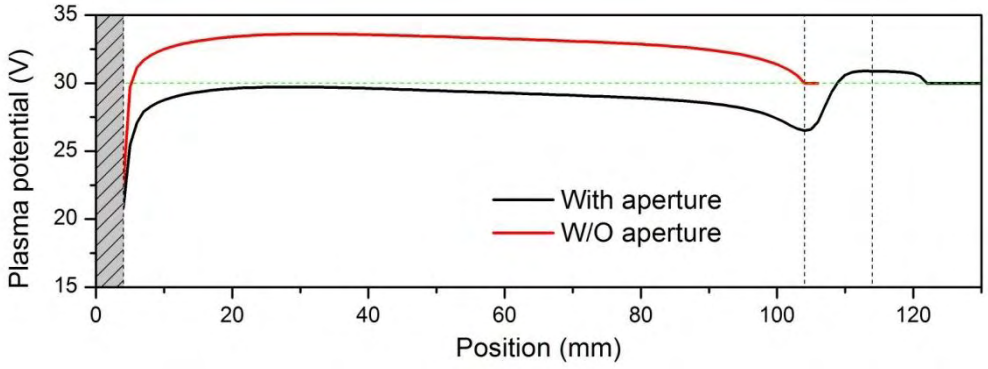

(b)

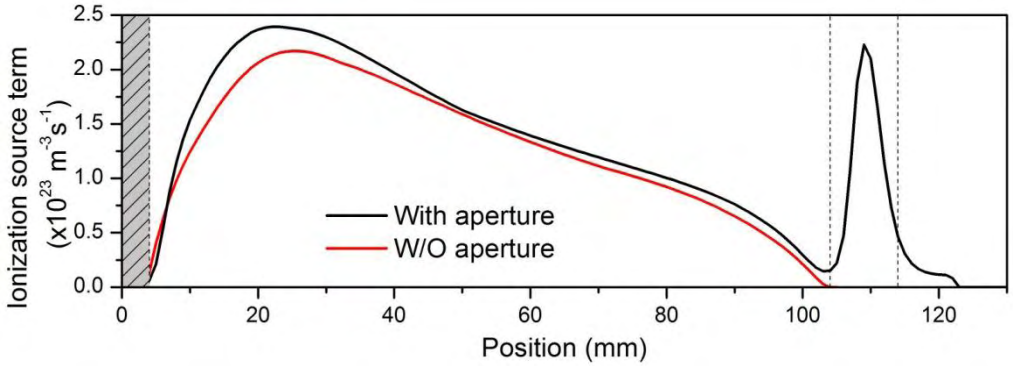

Figure 5.17: Comparisons of on axis profiles with and without (as in previous section) full description of the aperture; (a) potential profile, (b) ionization source term.

(a)

(b)

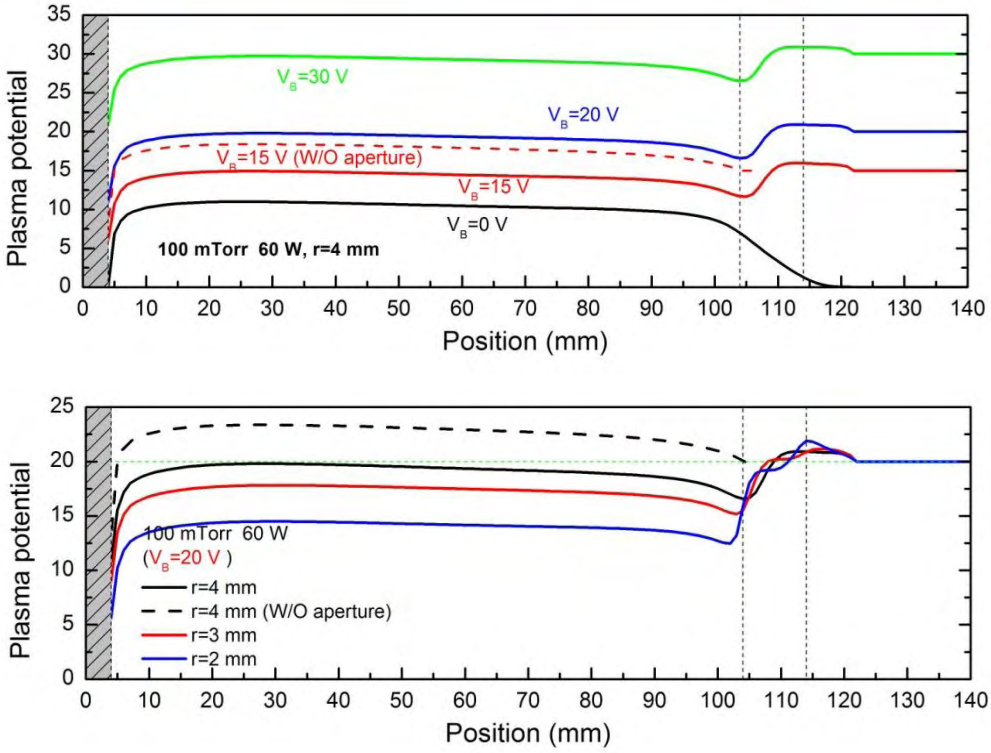

*Figure 5.18: (a) on axis normalized plasma potential profiles for different bias voltages with an aperture radius of 4 mm (1 cm thickness). The case without aperture is also displayed (dashed line) for a bias voltage of 15 V. (b) on axis plasma potential for a bias voltage of 20 V, for different radii (**4 mm, 3 mm, 2 mm**). The case without aperture (anode radius of 4 mm) is also displayed (dashed line) for a bias voltage of 20 V.*

(a)

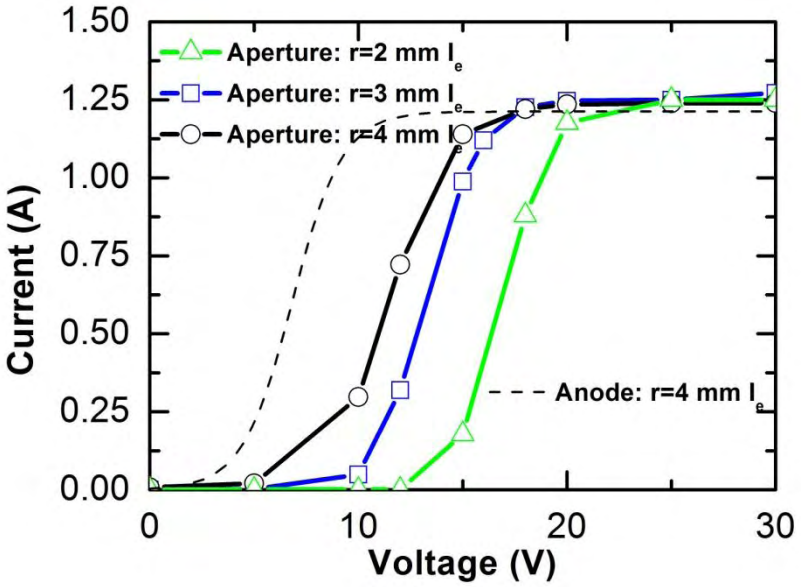

(b)

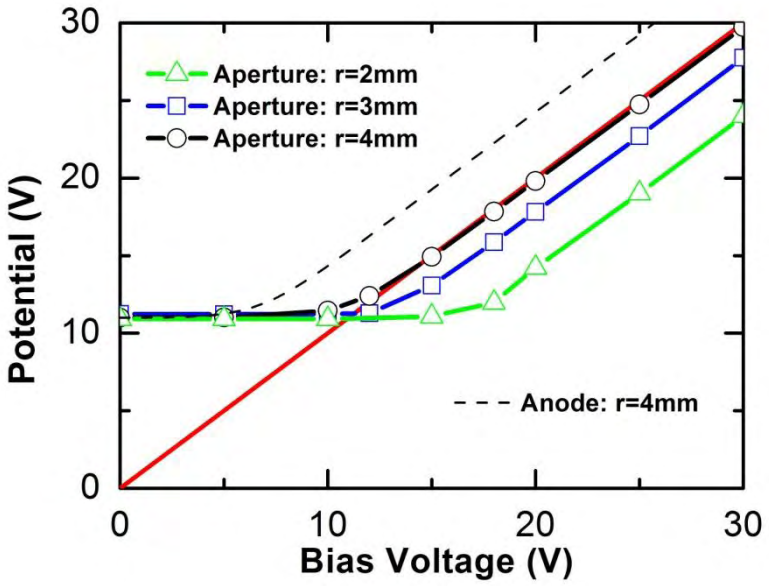

Figure 5.19: (a) extracted electron current, and (b), plasma potential as a function of bias voltage for three different values of the aperture radius, 2 mm, 3 mm, 4 mm and an aperture thickness of 1 cm. Power and pressure are 60 W and 100 mtorr. The case without full description of the full aperture (previous section) is also represented in dashed lines.

Figure 5.19a confirms that the needed bias voltage to extract the maximum possible current increases when the aperture radius decreases (i.e. the extraction curves are shifted to the right when the aperture radius decreases), as already seen in the previous section. We also see on this figure that more voltage is needed when the aperture is fully described and the anode is outside the chamber (comparison with

results of the previous section where the anode was on the red-plate of the chamber).

Finally it is interesting to deduce from the simulations the consequences of the choice of the aperture dimensions on the electron source performances. The performances of the electron source can be characterized by two important parameters: the total energy cost per extracted electron, which must be minimized, and the gas utilization efficiency which must be as large as possible.

To evaluate the cost per extracted electron we consider only situations where all the possible electron current is extracted (if the bias voltage is too low and only a small part of the current is extracted, the cost per extracted electrons will be very large since a large part of the electron current is lost on the walls of the discharge chamber). Therefore we calculate the cost per extracted electron at a bias voltage such that 90% of the maximum current is extracted. We note $V_{B_{90\%}}$ this bias voltage.

The energy cost (in eV) per extracted electron is therefore equal to:

(5.1) $$C_e = \frac{P + I_e V_{B_{90\%}}}{I_e} = \frac{P}{I_e} + V_{B_{90\%}}$$

P is the power absorbed in the source (the power losses in the circuit are not included) and I_e is the extracted current at a bias $V_{B_{90\%}}$ and $I_e V_{B_{90\%}}$ is the power used to extract the electron current.

The gas utilization efficiency can be characterized by the parameter F defined as the number of electrons extracted per injected xenon atom:

(5.2) $$F = \frac{I_e}{e\dot{M}/M}$$

where $\dot{M}$ is the xenon mass flow rate and M the xenon mass. For xenon, we have:

(5.3) $$F \approx 1.4 \frac{I_{e(A)}}{\dot{M}_{(mg/s)}}$$

When $F=1$, each injected xenon atoms is ionized once, and if F is larger than one (better gas utilization efficiency), each injected atom is ionized more than once (ions recombine on the walls so each atom can be ionized several times). The formula above indicates that the equivalent current of 1 mg/s of xenon is about 0.7 A.

When choosing the operating point of an electron source, we must choose the gas mass flow rate and the aperture radius. For a given aperture radius, the gas mass flow

rate imposes the pressure inside the discharge. We have seen in the previous chapters that operating at very low pressure with the microwave source may be a problem for the ignition of the discharge, and that breakdown is relatively easy at 100 mtorr. Several combinations of mass flow rate and aperture radius can give the same pressure. Therefore, if we fix the pressure at 100 mtorr, we have to choose the optimum combination of mass flow rate and aperture dimensions.

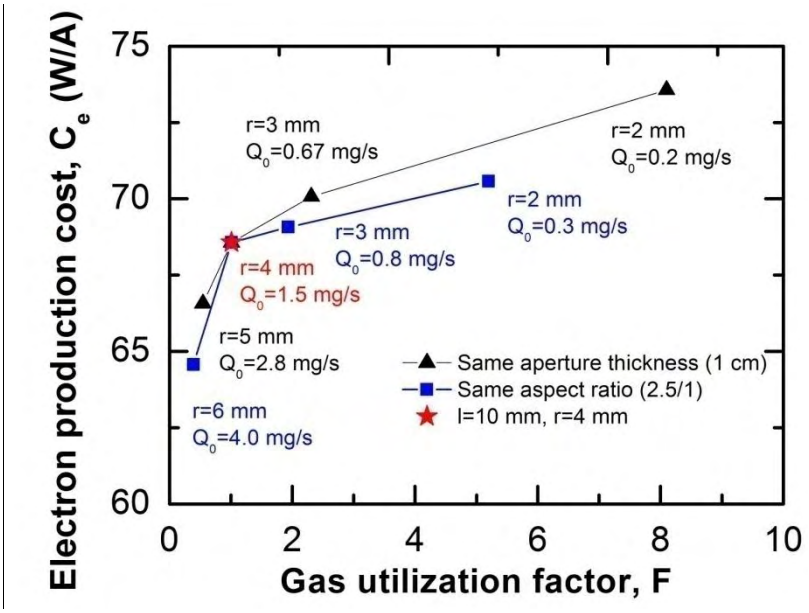

Figure 5.20: Map showing the energy cost per extracted electron and the gas utilization efficiency for different values of the aperture dimensions. The power is 60 W, the mass flow rate is adjusted for each aperture so that the pressure in the chamber is 100 mtorr. The bias voltage is such that 90% of the electron current is extracted.

We see from these two parameters C_e and F defined in equations (5.1) and (5.2), that the choice of the aperture radius and mass flow rate implies a compromise between energy cost and gas utilization efficiency. If the radius is small , this is good for the gas utilization efficiency (because the same pressure can be obtained at a lower mass flow rate than for a larger radius), but the energy cost is larger because a larger bias voltage is needed to extract the electron current. This is represented in *Figure 5.20* which provides the energy cost per extracted electron and the gas utilization efficiency for different values of the aperture dimensions. We see that it is necessary to operate at radii below 4 mm to obtain a good gas utilization efficiency.

5.4Conclusion

In this chapter we have studied the conditions of electron extraction from the microwave source. We have first reported from the literature, the different regimes of electron extraction in a low pressure plasma. Three regimes have been identified. 1) The ionic sheath regime, where the size of the extraction aperture is such that all the electron current can be extracted if a sufficient bias voltage is applied at the extracting electrode. This regime is obtained if the ratio between the extraction area and the chamber walls is larger than, with 1.7μ $\mu = \sqrt{2.3m/M}$ and m and M are the electron and atom masses respectively. In this regime the plasma potential is above the bias voltage and increases linearly with the bias voltage (for sufficiently large bias). 2) The electronic sheath regime where the maximum extracted electron current is equal to the saturation current (thermal flux times area of the extracting electrode). This is for example the regime of a Langmuir probe, and should occur, according to the theory, for ratios of the extracting electrode area to chamber wall area smaller than μ. In this regime the plasma potential is not perturbed by the bias voltage and does not increase with bias voltage. 3) The third regime, takes place when the area ratio is between and μ and 1.7μ. In this regime, a double sheath is present (potential dip with electronic sheath next to the extracting electrode), and all the electron current can be extracted is the bias voltage is sufficiently large. The plasma potential increases with the applied bias voltage.

We have then showed that this theory can be extended to the case of a collisional plasma if the parameter μ is replaced by $h\mu$ where the h parameters depends on the geometry and on the ion "collisionality" therefore on the gas density, i.e. the higher gas density, the bigger h.

In a second part of this chapter we have used the 2D model to study the conditions of electron extraction with a biased electrode (anode) placed on the chamber walls. In the third section of this chapter we have considered the problem of electron extraction with a more realistic geometry including an aperture in the chamber wall, and an anode placed downstream, outside of the chamber. In both sections we have shown that the ionic sheath and double sheath regimes predicted by the theory are well reproduced by the simulations. We have quantified the extracted electron current as a function of bias voltage and aperture dimensions. Finally we have shown that the choice of the aperture dimensions must be done by making a compromise between a good gas utilization efficiency (which is obtained for low aperture radii), and a low extracting voltage (which is obtained for larger radii).

5.5 References

[1] Lacoste, A., T. Lagarde, et al. Multi-dipolar plasmas for uniform processing: physics, design and performance. *Plasma Sources Science and Technology*. 11(4): 407 (2002)

[2] Lacoste, A., S. Béchu, et al. Extraction of large-area low-energy electron beams from a multi-dipolar plasma. *Plasma Sources Science and Technology*. 18(1): 015017 (2009)

[3] Hershkowitz, N. Sheaths: More complicated than you think. *Physics of Plasmas*. 12(5): 055502 (2005)

[4] Longmier, B., S. Baalrud, et al. Nonambipolar electron source. *Review of Scientific Instruments*. **77**(11): 113504 (2006)

[5] Baalrud, S. D., N. Hershkowitz, et al. Global nonambipolar flow: Plasma confinement where all electrons are lost to one boundary and all positive ions to another boundary. *Physics of Plasmas*. 14(4): 042109 (2007)

[6] Longmier, B. and N. Hershkowitz. Improved operation of the nonambipolar electron source. *Review of Scientific Instruments*. **79**(9): 093506 (2008)

[7] Longmier, B. and H. Noah. Helicon Mode and Xenon Operation with the Nonambipolar Electron Source. *43rd AIAA/ASME/SAE/ASEE Joint Propulsion Conference & Exhibit*. 11 July 2007, Cincinnati, OH

[8] Oks, E. *Plasma Cathode Electron Sources: Physics, Technology, Applications*. (Wiley, 2006)

General conclusion

Ion sources for space propulsion need an electron source to neutralize the ion beam. Thermoionic hollow cathodes are efficient sources of large electron current in a relatively small volume. They are however expensive, fragile because of high temperature operations and the electron emitter is sensitive to contamination by oxygen, which may be a problem for operation on low orbits. It is therefore useful to pursue the research efforts to develop efficient electron sources that do not rely on thermionic emission. To be considered for space applications, these sources must be efficient (low absorbed power per unit electron current extracted) and have a good gas utilization efficiency (low gas flow rate per unit electron current extracted).

In this thesis we have studied the properties of an electron source based on microwave excitation, which has been proposed by Diamant and operates in xenon, around 100 mtorr, at a microwave frequency of 5.8 GHz, and with power of dozens of Watts. The source properties have been thoroughly experimentally analyzed by Diamant, but no systematic modeling of this source had been developed so far. The purpose of our work was therefore to model the operation of this electron source, to understand its physical properties (plasma generation, plasma properties, electron extraction) and to evaluate its potential and limitations.

A large part of the work presented in the thesis is based on a 2D discharge fluid model called CAVIMO developed over the years at LAPLACE/GREPHE. We have also developed and used specific tools to analyze specifically the question of microwave propagation in the discharge cavity prior to the formation of the plasma (FDTD method, HFSS code), and to study the discharge properties with an approach much simpler than the 2D model (global, 0D model of the plasma source).

The basis of the fluid model of the discharge are recalled in chapter 2. The rest of the work is presented in three parts: 1) in chapter 3: questions related to microwave coupling in the cavity prior to the plasma formation, and breakdown and plasma formation in the cavity, 2) in chapter 4: plasma properties from the 2D and global models, 3) in chapter 5: questions related to electron extraction from the plasma.

In chapter 3 we have recalled the theory of microwave coupling in a cylindrical cavity and have explained the design and dimensions chosen by Diamant for the electron source. We have also described breakdown and plasma formation in the cavity and shown that for the dimensions of the Diamant’s source (which are related to the wave length of the 5.8 GHz wave considered in this work), a good operating point (i.e. which gives a reasonable breakdown field) is around 100 mtorr.

The study of the plasma properties in chapter 4 can be summarized as follows:

- the global (0D) model provides a very good insight in the plasma properties and its conclusions are in good agreement with those of the more complex 2D fluid model. The reason for the good agreement is that, in spite of the relatively large collisionality of the plasma (the electron and ion mean free paths at 100 mtorr are significantly smaller than the vessel dimensions), and of the very local electron heating in the very thin skin depth, the mean free path for electron energy exchange with the neutral atoms is long (i.e. the electron thermal conductivity is large) and the electron temperature is almost constant in the discharge volume). Nevertheless the more complex 2D fluid model provides a much more detailed and accurate description of the plasma properties and is necessary when gas flow and gas heating are considered.
- In the conditions of operations of the source the electron temperature is relatively low, on the order of 1 eV, and a large part of the ionization in the discharge volume is due to stepwise ionization of the metastable xenon atoms. An important conclusion from the 0D and 2D models is that the average energy loss (including collision losses and energy losses to the wall) per electron-ion pair generated in the volume is on the order 50 eV and does not vary significantly in the relatively large range of pressure (20 to 200 mtorr) and power (10 to 100 W) studied in this work. The maximum electron current that can be extracted from a plasma source in these conditions is therefore on the order of 20 mA/W, a number in agreement with several experiments on xenon plasma sources in the same pressure range (the experiments of Diamant however gives a larger current per unit power). The averaged plasma density predicted by the 0D and 2D models for an absorbed power of 60 W is on the order of 10^{19} m^{-3}.
- The 2D simulation results show that the detailed description of the plasma-Maxwell coupling is not really necessary. It is sufficient to assume that all the power is absorbed in a thin plasma layer (about 1 mm) next to the quartz plate.The results are not very sensitive to the thickness of the region of power absorption (between 1 and a few mm) so most of the calculations presented in this work have been obtained assuming that the power is absorbed in a 1 mm plasma slab (this simplifies the numerical aspects of the model since the plasma-Maxwell coupling can be quite cumbersome numerically).
- When gas flow and gas heating are included in the model, the results show an increase of more than 300 K next to the quartz plate for an injected power of 60 W (and assuming that the metallic walls are cooled). The consequences are that the gas density tends to be lower next to the microwave power injection side. And this tends to balance the effect of a slightly larger electron temperature (and ionization rate) next to the power injection (quartz plate). The predicted plasma density is therefore more uniform when gas heating is included. Although the agreement between model and experiments for the maximum plasma density and the electron temperature is rather good, the predicted plasma density profile is significantly

"flatter" in the simulations. One possible reason for the discrepancy could be that the walls are not perfectly cooled in the experiments but we do not have a definite explanation at the moment.

Chapter 5 is devoted to the question of electron extraction from the source. This question definitely can be addressed only with the 2D model. In this chapter we have first recalled the three different possible regimes of electron collection from a small electrode in a plasma (ionic sheath for large enough area of the collector, electronic sheath, for very small collection areas, as in probes, and double sheath regime in between). We have shown that the theory, derived for a collisionless plasma, can be extended to more collisional plasmas. We have then performed simulations with realistic apertures in the chamber and with an extracting anode outside the chamber. A large part of the electrons generated in the source can be extracted if a sufficiently large voltage is applied (only the electrons that are necessary to neutralize the ion flux to the dielectric quartz plate cannot be extracted; they represent less than 10% of the total electron current). We have shown that the voltage required to extract the electron is sensitive to the size of the aperture. This is quite intuitive but the model has helped to quantify this dependence. The results show that about 15 V are sufficient to extract 90 % of the electron current for an aperture of 4 mm radius and 1 cm length, while 20 V are necessary for a 1 mm radius (the anode was about 1 cm away from the aperture, outside the chambers). The choice of the aperture size must result from a compromise between a small enough aperture to get the required value of the pressure (around 100 mtorr) at a low xenon mass flow rate (good gas utilization efficiency), and a sufficiently large aperture to minimize the power loss to extract the electrons from the source. The model shows that a good gas utilization efficiency can be obtained for an aperture radius less than 4 mm. The choice of Diamant in his source in an aperture of 4 mm radius and 1 cm length, but the model shows that a 3 mm radius and ¾ cm length allows to operate at a mass flow rate reduced by a factor of 2, with a minor increase of the extraction cost.

Finally, we can say that the fact that the energy cost per electron-ion pair generated in the discharge does not depend much on pressure and power in the considered range of variations of these parameters seems to indicate that it will be difficult to improve this energy cost even with different sources (not mentioning the efficiency of the power coupling to the discharge) or by adding magnetic confinement (magnetic confinement has the same effect as reducing the surface over volume ratio of the chamber, or increasing the pressure). This seems in contradiction with the results of Diamant who shows an increase of the source performance with magnetic confinement. More work is needed to understand this feature. An experiment is being developed at LAPLACE/GREPHE to study an electron source in conditions similar to those of Diamant, and more detailed comparisons between experiment and model will be performed.

Author : Yu ZHU

Title : Modeling of a microwave plasma electron source for neutralization of ion thrusters

Supervisors : M. Jean-Pierre BOEUF and M. Laurent LIARD

Date and place : May 22, 2013, LAPLACE's colloquium hall, Toulouse

Abstract :

The electron sources are used to neutralize the ion beams from the ion thrusters. The conventional neutralizers are thermoionic hollow cathodes, which are fragile, expensive and very sensitive to the contaminations, especially by Oxygen in Low Earth Orbit. Therefore, the research in seeking a plasma electron source is still very active. In my thesis, I have tried to understand the physics behind a microwave plasma electron source, by means of analytical global model and self-consistent numerical model, and compared the results with the experimental results.

The first effort was devoted to better understand the plasma generation under the conditions similar to those of experiments. In particular, we found the best thresholds of gas flow rate, gas pressure and aperture size in order to trigger the breakdown. The second effort was devoted to understand how much is the maximum electron current that is available for extraction in the plasma source under the operation pressure range, and provide quantitative information on the plasma characteristics (plasma density, electron temperature, etc…). We found the maximum current in this source is not very sensitive to the pressure and is around 20 mA/W. Knowing the maximum current, we based our last numerical study on the sheath theory, to tune the aperture size in order to extract all the electrons out from the plasma source.

In the second and last study, both analytical and numerical tools were employed, and the results were in good agreements with those from the experiments.

Keywords: ion thruster, neutralizer, microwave plasma source, global model, self-consistent model, fluid model, ionic sheath, double sheath, electronic sheath

Specialty : Plasma Physics and Plasma Engineering

Laboratory :

Laboratoire Plasma et Conversion d'Energie (LAPLACE)
118, route de Narbonne
31062 TOULOUSE CEDEX 9

Auteur : Yu ZHU

Titre : MODELISATION D'UNE SOURCE PLASMA MICROONDE D'ELECTRONS POUR LA NEUTRALISATION D'UN PROPULSEUR SPATIAL IONIQUE

Directeurs de thése : M. Jean-Pierre BOEUF et M. Laurent LIARD

Date et lieu de soutenance : le 22 mai 2013, salle des colloques de LAPLACE, Toulouse

Résumé : Les sources électroniques sont utilisées pour neutraliser le flux d'électrons sortant d'un propulseur ionique. Les neutraliseurs conventionnels sont des cathodes creuses thermoioniques. Elles sont malheureusement fragiles, chères et très sensibles à la contamination par des espèces étrangères comme l'oxygène pour les orbites basses. Ainsi, des efforts de recherche autour des sources électroniques sont en cours. A l'aide d'un modèle analytique global ainsi qu'un modèle numérique auto-cohérent, je me suis attaché, durant ma thèse, à comprendre la physique qui régit les sources plasmas micro-ondes d'électrons et à comparer les résultats des modèles avec les résultats expérimentaux.

Dans un premier temps, nous avons cherché à mieux comprendre la phase de génération du plasma sous des conditions similaires à celles de l'expérience. En particulier, nous avons pu trouver les meilleurs seuils de taux de flux de gaz, de pression de gaz et de taille de l'ouverture d'extraction des électrons, afin de déclencher le claquage. Ensuite, nous avons cherché les valeurs maximum de courant électronique qu'il est possible d'extraire de la source plasma, suivant les plages de pression de l'expérience, et nous avons fourni des informations quantitatives sur les caractéristiques du plasma (densité plasma, température électronique, etc...). Nous avons trouvé que le courant maximum dans la source n'est pas très sensible à la pression et se situe autour de 20 mA/W. Connaissant le courant maximum, nous avons basé notre dernière étude numérique sur la théorie de gaine, afin de régler la taille de l'ouverture, dans le but d'extraire tous les électrons de la source plasma.

Dans cette étude ainsi que la précédente, les outils analytiques et numériques ont été employés, et les résultats se sont trouvés être en bonne correspondance avec ceux de l'expérience.

Mots-Clés : Propulsion ionique, neutraliseur, source plasma micro-onde, modèle global, modèle auto-cohérent, modèle fluide, gaine ionique, double gaine, gaine électronique.

Discipline administrative : Ingénierie et Physique des Plasmas

Intitulé et adresse du laboratoire :

Laboratoire Plasma et Conversion d'Energie (LAPLACE)
118, route de Narbonne
31062 TOULOUSE CEDEX 9